
Master's Thesis
International Master's Programme in Space Sciences

# Fine Structures in Coronal Mass Ejections-Driven Sheath Regions

Erika Palmerio
2015

Supervisor: Emilia K. J. Kilpua
Examiners: Hannu E. J. Koskinen
Emilia K. J. Kilpua

UNIVERSITY OF HELSINKI
DEPARTMENT OF PHYSICS

PL 64 (Gustaf Hällströmin katu 2)
00014 University of Helsinki

HELSINGIN YLIOPISTO — HELSINGFORS UNIVERSITET — UNIVERSITY OF HELSINKI

| Tiedekunta/Osasto — Fakultet/Sektion — Faculty | Laitos — Institution — Department |
|---|---|
| Faculty of Science | Department of Physics |

Tekijä — Författare — Author
Erika Palmerio

Työn nimi — Arbetets titel — Title

Fine structures in coronal mass ejection-driven sheath regions

Oppiaine — Läroämne — Subject
Space Physics

| Työn laji — Arbetets art — Level | Aika — Datum — Month and year | Sivumäärä — Sidoantal — Number of pages |
|---|---|---|
| Master's thesis | January 2015 | 78 |

Tiivistelmä — Referat — Abstract

Coronal Mass Ejections (CMEs) often travel in the interplanetary space faster than the ambient solar wind. When their relative velocities exceed the local magnetosonic speed, a shock wave forms. The region between the shock front and the leading edge is known as a sheath region. Sheaths are compressed regions characterized by turbulent magnetic field and plasma properties and they can cause significant space weather disturbances.

Within the sheath region, it is possible to find fine structures such as planar magnetic structures (PMSs). The magnetic field vectors in a PMS are characterized by abrupt changes in direction and magnitude, but they all remain for a time interval of several hours nearly parallel to a single plane that includes the interplanetary magnetic field (IMF) spiral direction.

PMSs have been associated to several regions and phenomena in the heliosphere, but many of them occur in CME sheath regions. This suggests that CMEs play a central role in the formation of PMSs, probably by provoking the amplification and the alignment of pre-existing discontinuities by compression of the solar wind at the CME-driven shock or because of the draping of the magnetic field lines around the CME ejecta. The presence of PMSs in sheath regions, moreover, suggests that PMSs themselves can be related to space weather effects at Earth, therefore a comprehensive study of PMS formation and structure might lead to a better knowledge of the geoeffectiveness of CMEs.

This work presents the study of PMSs in the sheath region of CMEs with a magnetic cloud (MC) structure for a sample of events observed in situ by the ACE and WIND spacecraft between 1997 and 2013. The presence of fine structures is evaluated through the minimum variance analysis (MVA) method, needed for determining the normal vector to the PMS-plane. Then, the position of each PMS within its corresponding sheath region is determined and the encountered cases are divided into different groups. Eventually, a number of shock, sheath and MC properties is evaluated for each group, aiming to perform a statistical analysis.

The conclusions are that PMSs are observed in 80% of the studied sheath events and their average duration is ∼5 hours. PMSs tend to form in certain locations within the sheath: they are generally observed close to the CME-driven shock, close to the MC leading edge or they span the whole sheath. PMSs observed near the shock can be associated to strong shocks, while PMSs located near the MC leading edge can be related to high density regions and, therefore, to compression.

Avainsanat — Nyckelord — Keywords
Space plasma physics, Sun, Coronal mass ejection

Säilytyspaikka — Förvaringsställe — Where deposited
Kumpula Science Library

Muita tietoja — övriga uppgifter — Additional information

International Master's Programme in Space Sciences

# Contents

# Introduction

The Sun, besides being fundamental for the existence of the solar system and the human life, is also the cause of space disturbances within the heliosphere. The heliosphere refers to the region of space that contains the solar system, the solar wind and its whole magnetic field that shields the solar system from galactic cosmic radiation. The solar activity is extremely varied and complicated, and it is mainly related to the solar magnetic field. It includes the solar cycle, sunspots, solar wind, solar flares and coronal mass ejections (CMEs). The solar activity deeply affects the Earth's environment, being the origin of geomagnetic disturbances. The magnetosphere is the region of space that is controlled by the Earth's magnetic field and covers the various interactions between the solar wind and the Earth's magnetic field. The perturbations that take place within the magnetosphere are referred to as magnetospheric storms or, more simply, magnetic storms.

For several years, it was believed that solar flares were the main drivers of magnetic storms. The current theories connect the disturbance in the interplanetary medium that drives the geomagnetic storm to a coronal mass ejection (CME) or to a high speed stream of the solar wind originating from the coronal holes. CMEs are among the most violent and energetic events related to solar activity, releasing huge amounts of mass and magnetic flux from the Sun into the heliosphere.

Magnetic storms are phenomena that can be classified under the name of space weather. Space weather refers to the effects of the Sun and its variable magnetic conditions on the interplanetary space and Earth's magnetosphere, ionosphere and thermosphere, on the performance and reliability of space- and ground-based technological systems and even on human life and health. Therefore, as CMEs are among the main sources of space weather, a complete understanding of them is essential for the modern technological infrastructure in space and on ground.

CMEs often travel in the interplanetary space faster than the ambient solar wind. When their relative velocities exceed the local magnetosonic speed, a shock wave forms. The region between the shock front and the CME leading edge is known as a sheath region. Sheaths are compressed regions characterized by turbulent magnetic field and plasma properties and they can cause significant space weather disturbances.

The aim of this work is to investigate CME-driven sheath regions in high detail, in order to determine eventual fine structures, such as planar magnetic structures (PMSs). PMSs are characterized by magnetic field vectors that undergo abrupt changes in direction and magnitude but remain all nearly parallel to a single plane.

The presence of PMSs in sheath regions may lead to a better understanding of several phenomena of solar origin. Their correlation with sheath regions suggests that PMSs themselves can have a certain importance in space weather events. Moreover, PMS stud-

ies may lead to a better knowledge of CME origin and how the CME structure that is detected through remote sensing observations evolves to its in-situ counterpart.

The thesis is divided into two blocks. In the first three chapters, a theoretical review of coronal mass ejections, sheath regions and planar magnetic structures is given. In the second part, a sample of sheath regions is introduced, for which the presence of fine structures is determined through the minimum variance analysis (MVA) method. The properties, features and location of PMS's are then studied in greater detail and compared with the shock, sheath and CME properties.

# Chapter 1

# Coronal Mass Ejections

Solar flares and coronal mass ejections are two examples of solar eruptions, and they are the main storm phenomena that take place in the Sun's atmosphere.

Flares were thought to be the drivers or solar storms for many decades, though a tight connection between flares and storms was never found: a high-power flare can occur without giving rise to a magnetic storm and, similarly, it is possible to identify a storm without the presence of a solar flare [17].

The picture became clearer in the early 1970s, with the first space-borne coronagraph observations of CMEs made by the OSO-7 coronagraph [66]. A joint analysis of coronal and solar wind observations reported a disturbance, which was later called coronal mass ejection [14].

Nowadays, CMEs are believed to be the main drivers of magnetic storms, and therefore mainly responsible for space weather effects at the Earth [17] [70]. They are large eruptions containing plasma and magnetic fields that are expelled from the Sun into the heliosphere.

In this chapter, the main observational and physical properties of CMEs are reviewed, before continuing to the detailed description of their sheath regions in Chapter 2.

## 1.1 Remote sensing CME observations

CME observations were traditionally obtained by visual inspection of coronagraph images. Nowadays, in addition to the automatization of the CME detection process, the view of CMEs has broadened considerably as the result of observations made by other instruments at a wide range of wavelengths. Phenomena related to CMEs can manifest in fact at every observable wavelength, as well as in a number of interplanetary signatures.

### 1.1.1 Coronagraph observations

A coronagraph is a device that produces an artificial eclipse, in order to occult the solar disk for coronal observations. This allows the scattered light leaving the faint surrounding corona to be observed around the occulting disk, which hides the entire solar surface.

Since a CME itself does not emit radiation, the observed light originates from the Thomson scattering of the solar photons from the electrons within the erupting plasma. The solar photons are mostly in the visible range, therefore coronagraphs are mainly

working with white light.

The images produced by coronagraphs are two-dimensional, which means that they are projections of CMEs into the plane-of-sky. Hence, the CME image that appears to the observer is highly dependent on the propagation direction. CMEs that propagate along the Sun-observer line experience large projection effects and they appear as clouds surrounding the Sun, therefore they are called halo CMEs. Those CMEs propagating to other directions but with a major component along the Sun-observer line appear to only partially encircle the Sun and they are defined as partial halo CMEs [18].

The first coronagraphs were introduced by Lyot in 1930 and were ground-based. A ground-based coronagraph operates within Earth's atmosphere and therefore suffers from scattering of light in the sky itself. Moreover, from Earth it is not possible to visualize the corona as far from the solar disk as from space-based instruments. It was in the early 1960s that it was possible to look farther out in the corona, with the launch by Tousey of an externally occulted coronagraph on a sounding rocket. Several externally occulted coronagraphs had been used since then, even though these instruments encounter two main problems. First, for a given distance from the occulting disk to the first imaging element, the instrument can only provide images of the corona out of a certain radius ($> 1.5R_{\odot}$). Moreover, at distances near the inner edge of the field of view, most of the imaging element is shadowed by the occulter. Second, because of size limitations, the aperture cannot usually exceed a few centimeters [2]. These problems reduce the resolution of the coronagraph images. The most productive coronagraph to date for CME observations has been the Large Angle Spectroscopic Coronagraph (LASCO), one of the instruments on board the SOHO mission, a project of international cooperation between ESA and NASA. LASCO overcomes the problems related to externally occulted coronagraphs because it consists of three different coronagraphs (named C1, C2 and C3), which cover overlapping fields of view. C1 inspects the corona from $1.1R_{\odot}$ to $3R_{\odot}$, C2 (Fig. 1.1a) images the Sun from $1.5R_{\odot}$ to $6R_{\odot}$ and C3 (Fig. 1.1b) surveys the corona between $3.7R_{\odot}$ and $32R_{\odot}$. C1 is a Fabry-Perot interferometer coronagraph (currently not operating), while C2 and C3 are two white light coronagraphs.

Since the year 2006, LASCO was joined by the Solar Terrestrial Relations Observatory (STEREO) mission, in which each spacecraft is equipped with two coronagraphs with different fields of view.

### 1.1.2 Other methods

Remote observations of CMEs can also be achieved through other methods and instruments, by means of EUV and heliospheric imaging and radio tracking.

The development of a CME takes place also in the lower corona, region that is occulted by coronagraphs. It is possible to study the solar atmosphere from the photosphere outwards through observations at many wavebands, from radio to X-ray.

Soft X-ray and EUV imaging contribute to coronal observations in multiple ways, from the direct viewing of ejecta to the observation of coronal dimming, i.e. long-term brightness decrease on the solar surface. This kind of data show that the coronal restructuring below the erupting CME extends long and wide through the corona, which is consistent with the idea that a CME opens the magnetic field in order to let the flow of an enhanced solar wind [19].

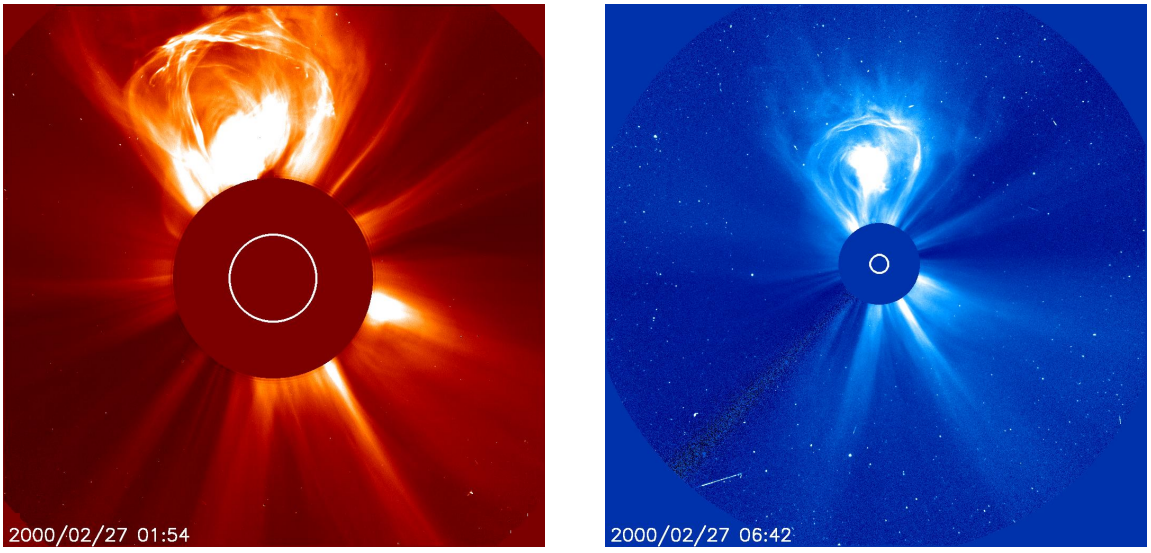


**(a)** LASCO C2 **(b)** LASCO C3

**Figure 1.1:** A coronal mass ejection on February 27, 2000 reported by SOHO LASCO (a) C2 and (b) C3. The white circles indicate the solar disk. Image credit: SOHO (NASA and ESA cooperation).

Observations at radio frequency can provide information about the large-scale restructuring of the corona during a CME event and the connectivity of the coronal magnetic field. The band 30-300 MHz brings to the identification of radio bursts, while the domain down to ∼30 kHz is well covered by ground-based instruments. Radio bursts give details about energetic electrons that can be trapped within magnetic structures or propagate along open field lines [19].

## 1.2 CME onset and evolution

Coronagraph observations have shown that a typical CME contains a mass of the order of $10^{11}$-$10^{12}$ kg, a speed between 400 and 1000 km/s and a kinetic energy that may exceed $10^{25}$ J [18].

The eruption of the magnetically closed volume that forms a CME is usually associated with the lower latitude regions of the solar corona. It may also be associated with the heliospheric current sheet (the surface where the polarity of the solar magnetic field changes from north to south). The occurrence of a CME follows the solar cycle, and it is around once a day during solar minimum, and around four or five times per day during solar maximum. Only a small percentage of CMEs are directed towards the Earth, and it is important to observe them in order to gain a better understanding of space weather phenomena.

With only 2D coronagraph images, very poor information about the 3D structure of CMEs can be deduced. Many geometrical techniques that take advantage of multi-viewing capabilities offered by the twin STEREO spacecraft have been developed in order to determine the whole CME 3D-shape, such as forward modeling, tie-pointing, inverse

reconstruction and other triangulation models, as well as techniques that place the CME within a volume bound by a polygon [71].

The CME plasma is driven by an expanding magnetic field, which usually has the form of helical field lines with changing pitch angles, i.e., a flux rope [71]. The "classic" shape of a CME is the so-called three-part CME, which includes a bright leading front, a following dark cavity and bright core. The current understanding is that the dark cavity is associated with an erupting flux rope, bright frontal loop results from pile-up of coronal loops over the erupting flux rope and bright core is the filament within. In such case, the CME is simply seen as the ejection of a magnetic flux-rope structure from the lower corona which takes the form of a three-part CME.

Recent studies based on LASCO and STEREO images [67], however, show that fast shock-driving CMEs have a five-part structure: the classic three-part CME described above is preceeded by a shock and the faint front caused by a density compression at the shock.

The element composition of the CME plasma remains uncertain. It seems reasonable that the material dominating the launch region of the CME could embody the major part of the mass of the CME, i.e., the CME abundance should be similar to that of its launch region. In reality, a CME is probably composed of different materials coming from various zones of the Sun, and the relative percentages of the elements is variable in different events [18].

The observation and study of energetic particles in the interplanetary (IP) medium allow investigating the structure and development of CMEs. Solar energetic particles (SEPs) originate from at least two different processes, both of which are likely related to CMEs: acceleration at CME-driven shocks and magnetic reconnection. Observations indicate that some solar particles originate from heated and/or dense plasma. Eruptive events, such as solar flares and CMEs, can transfer some of their energy to solar particles, which are accelerated to relativistic speeds.

A thorough understanding of the physics of SEPs may provide various answers: information about magnetic field topologies could be gained, because particles' paths tend to follow field lines through the heliosphere, and also the size of CME shocks can be better understood from the amount of accelerated populations. SEPs can in addition help to comprehend in a better way particle acceleration processes in general. Moreover, if galactic cosmic rays (energetic particles coming from outside the heliosphere) experience a decrease in their intensity, this may indicate the presence of a CME in the IP medium, known as an interplanetary coronal mass ejection (ICME). Particles track magnetic structures within ICMEs [3]. The initial process that gives acceleration to SEPs is still unknown.

### 1.2.1 CME onset

Due to the low value of plasma $\beta$ in the corona [18], CMEs are defined as magnetically-driven phenomena. The $\beta$-value in a plasma is described by the relation

$$\beta = \frac{2\mu_0 P}{B^2}\,, \tag{1.1}$$

i.e., the ratio between the plasma pressure, $P = nk_BT$, and the magnetic pressure, $P_{mag} = B^2/(2\mu_0)$.

However, initiation mechanisms of CMEs are currently not fully understood. The main reasons for such lack of information are both observational and theoretical. The principal observational difficulty is that it is not possible to measure directly the coronal magnetic field. Theoretical problems are related to the models, which appear to be incomplete and too idealized [45].

A good onset model should be able to describe a CME as it appears in coronagraphs and also all the CME-related phenomena, but no model yet is capable of fulfilling such requirements. It could be possible that different models are needed to describe different types of CMEs.

It is convenient to divide CMEs into two categories, in order to better describe both the onset and the early acceleration [59]. Slow and slowly accelerating CMEs take a long time to develop and they are associated with helmet streamers (Fig. 1.2a), while fast and highly accelerating CMEs have an explosive nature and are often associated with energetic events such as solar flares (Fig. 1.2b). The most significant theoretical difficulties are related to the energy release that can explain fast CMEs.

The general idea is that the CME onset should disrupt the gravitational, hydrodynamic and magnetic equilibrium of the corona, causing the eruption. In case the eruption is strong enough and without too many constraints, plasma is ejected into the interplanetary space. The mechanism that disturbs the equilibrium may be of various nature: it could be a structure (flux rope) that emerges from beneath the solar surface, or magnetic reconnection occurring somewhere in the coronal field, or a small reconfiguration of the local field [18].

Since a CME initiates in the corona, where the plasma $\beta$ is typically low, the energy a CME needs is mostly provided by the free energy available in the magnetic field, which must, therefore, contain significant electric currents. In consideration of the fact that the solar corona is assumed to be a force-free field, these electric currents are generally supposed to be field-aligned [1].

### 1.2.2 CME evolution and propagation

Like for the initiation process, the mechanism by which the CME propagates through the heliosphere after the eruption is not well understood. The reasons for such a lack of certain information are the same as for the launch mechanism: observational troubles and models that are too various.

The kinematic evolution of a CME can be described by a three-phase scenario: the initiation phase, the impulsive acceleration phase and the propagation phase [74]. The initiation phase is the onset process that gives rise to a CME from the solar corona. The duration of the impulsive acceleration phase is of the order of tens of minutes, and it is characterized by a fast and abrupt acceleration. After this phase, the CME is completely developed and its propagation starts, during which it usually travels at a nearly constant speed, that can undergo a minor acceleration or deceleration. In the outer corona, slow CMEs tend to accelerate, while fast CMEs are likely to decelerate [57]. This indicates that not all CMEs display a three-phase evolution and that the major acceleration takes place in the inner corona, while the subsequent development depends on the medium through which the CME propagates.

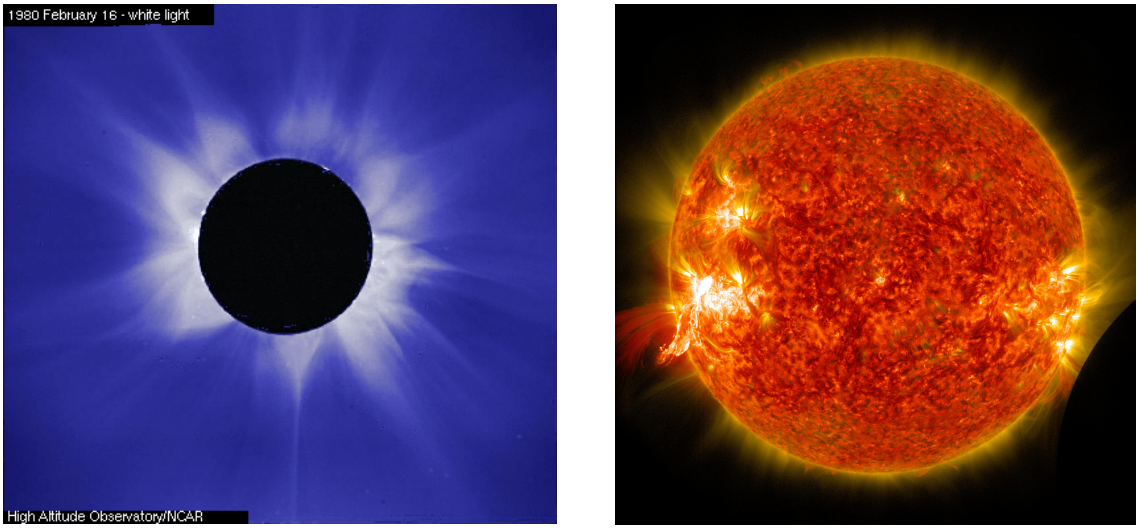


**(a)** Helmet streamers **(b)** Solar flare

**Figure 1.2:** a) Helmet streamers, bright and closed magnetic loop-like structures that develop over active regions and sunspots connect areas of the opposite magnetic polarity. They start out broad near the Sun and thin down to long pointed ends, and can be observed during eclipses. Image taken by the High Altitude Observatory of Boulder, Colorado, during solar maximum. b) Solar flare, here as the bright flash on the left side of the Sun. A solar flare is a sudden, rapid and intense variation in brightness observed over the Sun's surface or the solar limb, which is interpreted as a large energy release of magnetic energy that has built up in the solar atmosphere. Image captured by NASA's Solar Dynamics Observatory on Jan. 30, 2014.

Beyond a few solar radii, the value of the plasma $\beta$ reaches a value $> 1$ [18], which means that the magnetic field becomes less significant than the plasma and the surrounding fluid. As a consequence, the major role in the CME evolution is not played by magnetic processes, but by the hydrodynamics of the plasma.

The CME, after its abrupt formation and launch, propagates towards and through the interplanetary medium as an interplanetary coronal mass ejection (ICME), maintaining its integrity at quite large distances in the heliosphere.

## 1.3 In-situ CME characteristics

An interplanetary coronal mass ejection (ICME) is defined as the heliospheric counterpart of a CME, that is composed of two primary parts: an ejecta and a sheath. The ejecta is the ICME itself, which is energized in the eruption, and the sheath is a region of compressed and heated plasma ahead of it, Sheath properties are discussed in detail in Chapter 2. When a fast ICME drives an interplanetary shock, the term sheath refers to the region between the shock front and the ejecta, but slower CMEs may have also a sheath-like structure ahead of them. An ejecta may maintain its connection to the Sun or may disconnect from it, forming a magnetically closed structure, which is therefore named "plasmoid" [15] (Fig. 1.3).

Even though fast CMEs are decelerated while they travel in the heliosphere and only slow CMEs slightly accelerate, ICMEs often travel faster than the ambient solar wind. If

their relative speeds exceed the velocity of the local fast magnetosonic speed (see Section 1.3.2), then a shock wave must form [55]. The slower plasma ahead the shock is accelerated and flows around its path.

CMEs can be widely studied in situ, because they regularly pass through interplanetary spacecraft, even though the nature of the transition from CME to ICME still remains uncertain [34]. The physics that describes the two phenomena is different: while CMEs are magnetically and gravitationally dominated, the increase in the value of the plasma $\beta$ during their propagation makes ICMEs phenomena which are described by the physics of thermodynamics and hydrodynamics. ICMEs themselves are, however, characterized by a low plasma $\beta$, but their driving energy lies mainly in the bulk plasma motion, which is hydrodynamically dominated [18].

In-situ detection involves measuring certain parameters, such as magnetic field and bulk velocity, in a direct way, using the instruments onboard as the ICME passes the spacecraft. The in-situ spacecraft measurements are usually done only with one spacecraft, which presents a significant disadvantage: they are only able to follow one track within the extended ICME structure, and this leads to a loss in the complete vision of the phenomenon. In addition, most in-situ spacecraft are located at a distance of about 1 AU from the Sun. This is one of the reasons why the transition process from CME to ICME is still not well understood.

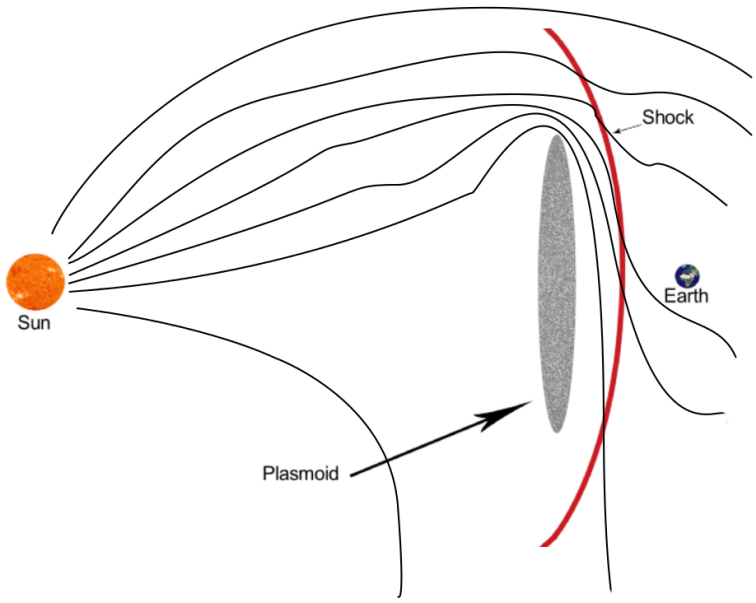


**Figure 1.3:** A sketch of a fast ejecta in a plasmoid configuration, disconnected from the Sun. The ICME is driving a shock (red line) and the IMF (black lines) within the region ahead of the ejecta drapes about the plasmoid. Image courtesy: Juhana Lankinen.

### 1.3.1 In-situ CME composition and signatures

Through the measurements provided by the spacecraft that operate in situ it is possible to detect a number of ICME signatures that are briefly summarized below. Measurements reveal that after an interplanetary shock the ICME experiences an enhancement in

the helium abundance. Moreover, it contains both high-temperature and low-temperature ions [18]. A CME usually spends several days travelling from the solar corona to the spacecraft, where it is detected, and its composition at 1AU might vary significantly from the one of the CME at its launch from the Sun because of the interactions with the ambient solar wind. However, charge states and elemental ratios can be used to probe the characteristics of CMEs at a few solar radii from the Sun. This is because ion charge states "freeze-in" at coronal altitudes, because ionization and recombination time scales become larger than the ion expansion time in the solar wind, and therefore they should not change significantly during the propagation of the CME from the Sun [51].

There are some signatures that are used for identifying ICMEs in situ, found in magnetic field, plasma dynamics, plasma composition, plasma waves and suprathermal particles [75] and briefly summarized in Table 1.1.

| **Magnetic field** | **Plasma dynamics** | **Plasma composition** | **Plasma waves** | **Suprathermal particles** |
|---|---|---|---|---|
| enhancement | density decrease | $\alpha/p$ ratio increase | ion acoustic waves | bidirectional ions |
| rotation | expansion decrease | high $^3He/^4He$ | | bidirectional electrons |
| variance decrease | $T_p$ decrease | $Fe/O$ enhancement | | cosmic ray depletion |
| discontinuities | $T_e$ increase | elevated $O^{7+}/O^{6+}$ | | bidirect. cosmic rays |
| magnetic cloud | forward shock | occurrence of $He^+$ | | |
| low beta | | | | |
| field draping | | | | |

**Table 1.1:** List of principal in-situ ICME signatures, discussed in Huttunen, 2005 [20], Zurbuchen and Richardson, 2006 [75], and references therein.

ICMEs, however, usually possess only a subset of the listed signatures. Forward shocks, mainly driven by fast ICMEs, are not proper signatures of ICMEs, but they are easily detectable, convenient and reasonably well-understood phenomena associated with ICMEs. The internal structure of interplanetary coronal mass ejections may be highly inhomogeneous. Moreover, to establish ICME boundaries is usually a difficult and complex task, even if they should ideally be a single tangential discontinuity that surrounds a region characterized by ICME signatures. More precisely, in practice different ICME signatures may indicate different boundaries, most likely because they arise from distinct phenomena [72].

The attempts to find a relation between in-situ parameters and coronagraph images of CMEs are aggravated by the fact that the ICMEs that are intercepted by the spacecraft at around 1 AU usually originate as Earth-directed front-side halos, for which the coronagraphs do not let a precise study of the CME structure and propagation speed. However, the twin STEREO spacecraft have provided a separated view of these phenomena, since the two satellites move around the Sun along two different orbits near 1 AU. A second complication is given by the detection methods, since a spacecraft takes measurements along a single trajectory through the whole ICME [10].

Indeed, the simplest case is the "classic" three-part CME, for which reasonably suitable models are available. In this case, the dark cavity observed in the corona should correspond to the flux rope in the ICME, even if the connection of the different structures

in a CME in remote sensing and in-situ surveys is not yet fully resolved [75].

In general, MHD simulations show that ICMEs' morphology undergoes a stretching and flattening of the shape as they propagate radially out in the heliosphere, phenomenon which is sometimes referred as "pancaking" [54].

Little is known about the behaviour of ICMEs in the outer heliosphere and at high heliographic latitudes. As they propagate, they might merge with co-rotating interaction regions (CIRs) or other ICMEs, in order to produce merged interaction regions (MIRs) or global merged interaction regions (GMIRs) [11]. MIRs and GMIRs are large-scale structures located in the outer heliosphere.

### 1.3.2 Interplanetary shocks

Interplanetary shocks can be explained by the MHD theory, where the plasma is considered as a single fluid. In the ideal MHD case (where the conductivity $\sigma \to \infty$) it is possible to define three different wave modes: slow, intermediate (shear Alfvén), and fast mode [36]. While the shear Alfvén mode, being non compressive, cannot form shocks, the slow and fast modes do. Their phase velocities are given by

$$\left(\frac{\omega}{k}\right)^2 = \frac{1}{2}(c_s^2 + v_A^2) \pm \frac{1}{2}[(c_s^2 + v_A^2)^2 - 4c_s^2 v_A^2 cos^2\theta]^{1/2}\,, \tag{1.2}$$

where the solution with plus sign describes the fast wave, while the minus sign represents the slow wave. Here, $c_s = \sqrt{(\gamma k_B T)/m}$ is the sound speed and $v_A = \sqrt{B^2/(\mu_0 \rho_m)}$ is the Alfvén speed.

When the plasma velocity exceeds the magnetosonic speed, defined as

$$c_{ms} = \sqrt{v_A^2 + c_s^2}\,, \tag{1.3}$$

a shock may develop. Through the introduction of the magnetosonic Mach number,

$$M_{ms} = \frac{V}{c_{ms}}\,, \tag{1.4}$$

where $V$ is the bulk speed in the shock frame, the condition for a shock to form becomes $M_{ms} > 1$. In MHD shocks, the plasma flow, super-magnetosonic in the upstream, is reduced to sub-magnetosonic in the downstream.

Other useful numbers in space plasma physics are the Mach number,

$$M = \frac{V}{c_s}\,, \tag{1.5}$$

and the Alfvén Mach number,

$$M_A = \frac{V}{v_A}\,. \tag{1.6}$$

Shocks and other discontinuities can be studied through the conservation equations known as Rankine-Hugoniot (RH) relations, that relate the upstream and the downstream states:

$$[\rho_m V_n] = 0\,, \tag{1.7}$$

$$\left[\rho_m V_n^2 + P + \frac{B_t^2}{2\mu_0}\right] = 0\,, \tag{1.8}$$

$$\left[\rho_m V_n \mathbf{V}_t + B_n \frac{\mathbf{B}_t}{\mu_0}\right] = 0\,, \tag{1.9}$$

$$\left[\rho_m V_n \left(\frac{V^2}{2} + \frac{\gamma}{\gamma - 1}\frac{P}{\rho} + \frac{B^2}{\mu_0 \rho}\right) - (V \cdot B)\frac{B_n}{\mu_0}\right] = 0\,, \tag{1.10}$$

$$[B_n] = 0\,, \tag{1.11}$$

$$[\mathbf{V}_n \times \mathbf{B}_t + \mathbf{V}_t \times \mathbf{B}_n] = 0\,, \tag{1.12}$$

where $[f] = f_2 - f_1$ represents the values at the jump over the shock (the subscript 1 stands for the upstream value, while the subscript 2 indicates the downstream value). The solutions of the RH relations describe different kinds of discontinuities and shocks in an ideal MHD plasma. A shock is characterized by the mass flux and compression across the discontinuity, while there is a discontinuity when no mass flow and compression occur together across the jump.

Discontinuities can be classified into three main classes:

- Contact discontinuities: characterized by an arbitrary density jump, but pressure and all other quantities are continuous
- Tangential discontinuities: plasma pressure and field change, but static pressure is conserved (i.e., $B^2/(2\mu_0) + nk_BT = \text{constant}$)
- Rotational discontinuities: field and flow change direction, but not magnitude

In the interplanetary medium it is possible to distinguish fast and slow shocks, according to, respectively, the increase or decrease in the magnetic field magnitude at the jump. Furthermore, shocks are divided to forward and reverse shocks depending on the frame-of-reference, see Fig. 1.4: fast forward (FF), slow forward (SF), fast reverse (FR) and slow reverse (SR). The majority of interplanetary shocks observed near 1 AU are fast forward shocks driven by CMEs. The CME rate correlates with the solar cycle phase, therefore also the occurence and structure of CME-driven shocks varies according to it [52].

An important parameter defining MHD shocks is the value of $\theta_{Bn}$, that is the angle between the magnetic field and the shock normal. A shock is parallel when $\theta_{Bn} = 0°$ and perpendicular when $\theta_{Bn} = 90°$. All other shocks, i.e. $0° < \theta_{Bn} < 90°$, are classified as oblique, but a useful convention in plasma physics defines shocks where $\theta_{Bn} < 45°$ as quasi-parallel, and similarly, shocks where $\theta_{Bn} > 45°$ as quasi-perpendicular.

Quasi-parallel and quasi-perpendicular shocks 1.5 show differences in their nature and structure. In the case of a quasi-parallel shock, magnetic field lines cross the shock and carry the particles (that follow field lines) through the shock relatively easily. In a quasi-perpendicular shock, on the other hand, the magnetic field lines are parallel to the shock surface, and the particle gyromotion along field lines does not let the particles pass through the shock, by reflecting particles back to the shock. As a result, the transition from the upstream to the downstream state occurs over a broad region for quasi-parallel shock, while shows a steep change in the magnetic field magnitude for quasi-perpendicular ones.

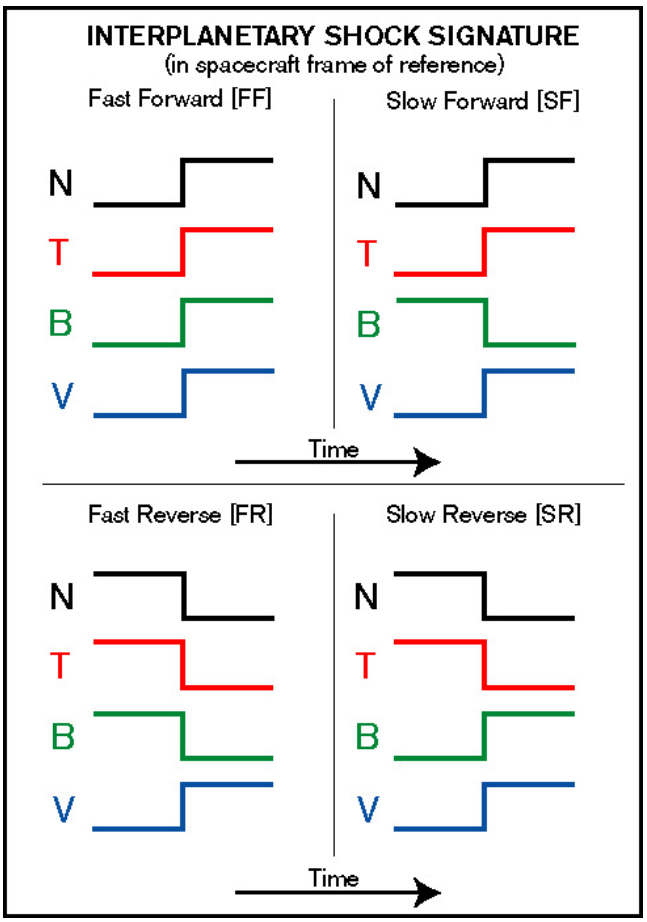


**Figure 1.4:** Sketch of the changes in some solar wind parameters for the four kinds of interplanetary shocks, from the point of view of the observing spacecraft. The reported parameters are: number density of the solar wind plasma $N$, proton plasma temperature $T$, magnitude of the magnetic field $B$, and plasma speed $V$. Image credit: NASA.

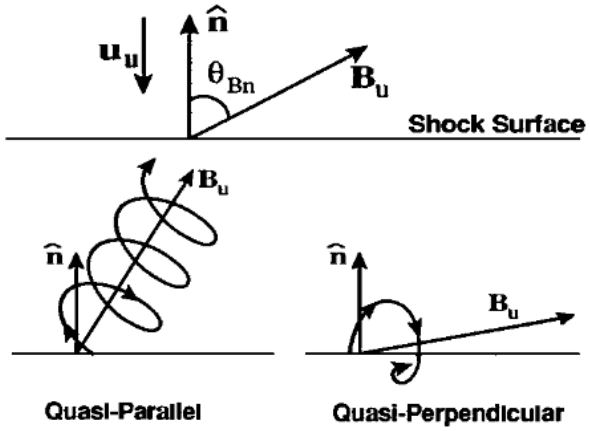


**Figure 1.5:** The shock angle $\theta_{Bn}$ and particle trajectories in quasi-parallel and quasi-perpendicular shocks. Image adapted from Kivelson and Russell, 1995 [35].

### 1.3.3 Flux-rope CMEs

Flux-rope ICMEs (Fig. 1.7a) usually have strong magnetic fields (> 10 nT), low proton temperatures and low plasma $\beta$ [75]. In addition, they are characterized by large and coherent internal magnetic field rotation [16]. If the above conditions are fulfilled, the ICME is typically referred as a magnetic cloud (MC, Fig. 1.6). MC-like features are found at $\approx$ 1 AU in about one-third of all ICMEs. Other kinds of ejecta, called "complex ejecta" (Fig. 1.7b), possess more complicated magnetic field configurations and lack large internal field rotation.

Since plasma is highly conductive, the interplanetary magnetic field is "frozen-in" to the plasma within the sheath. This prevents the solar wind and the ICME magnetic fields from merging. As a result of the large relative speed between fast CMEs and the ambient solar wind and of the high conductivity of plasma, the interplanetary magnetic field drapes around the ejecta [15]. Thus, in order to determine the topology of the magnetic field of an ICME it is necessary to distinguish the magnetic field of the actual ICME from the compressed ambient plasma and draped magnetic field.

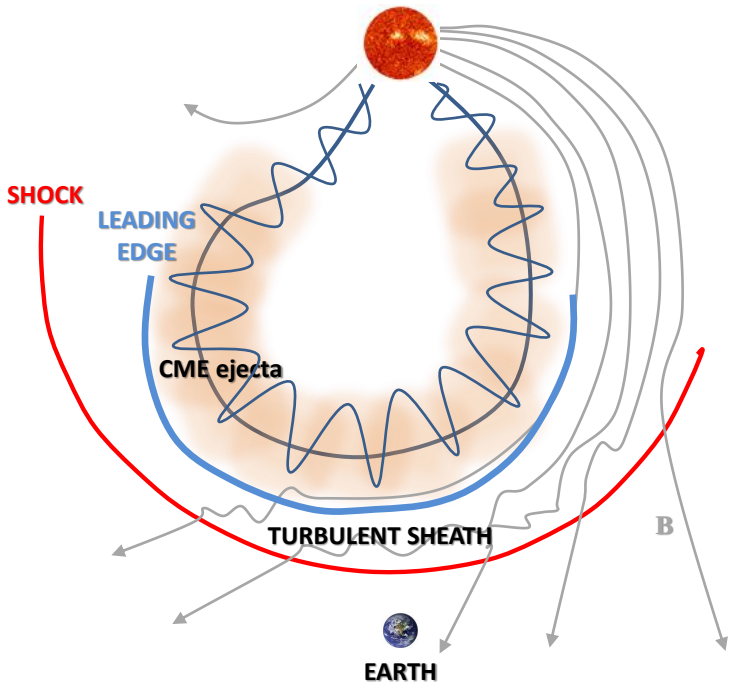


**Figure 1.6:** An ICME with a flux rope structure driving a shock. The blue line shows the ICME leading edge. Image courtesy: Emilia Kilpua.

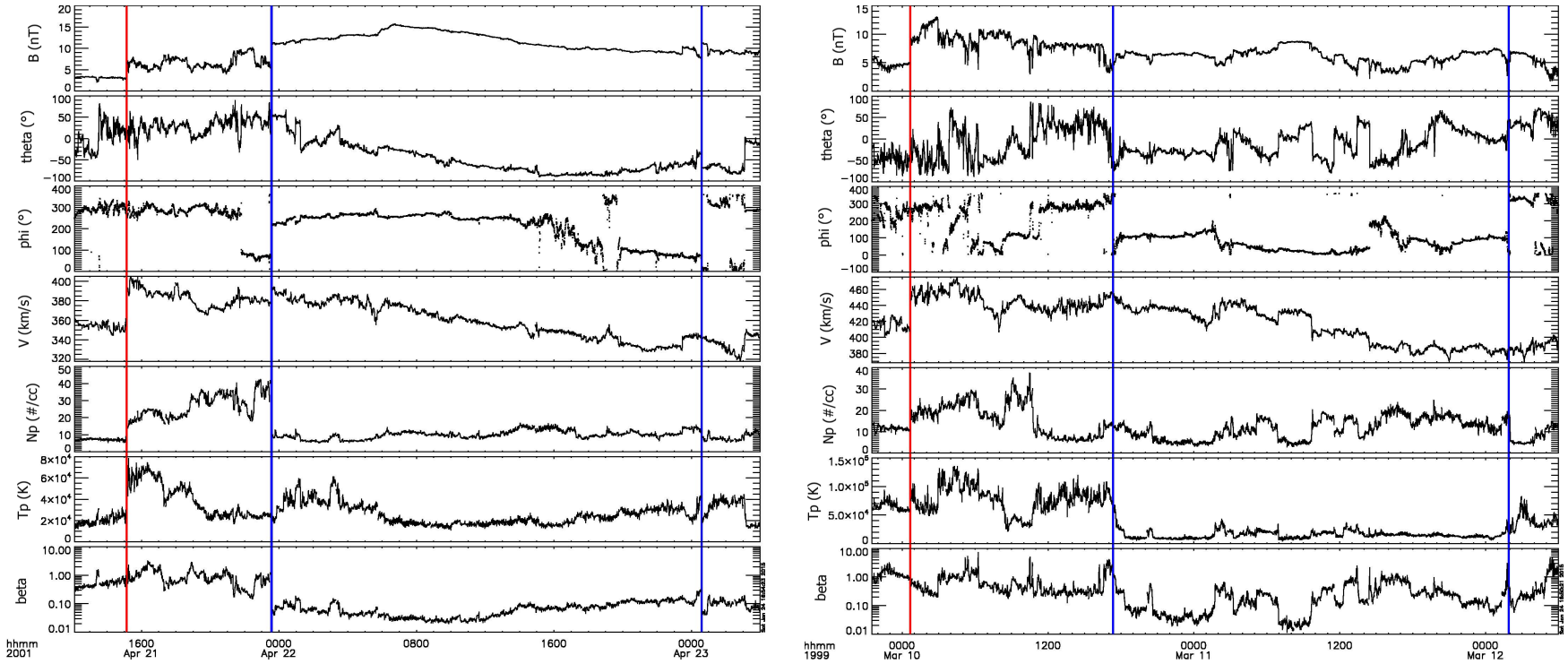


**(a)** Magnetic cloud **(b)** Complex ejecta

**Figure 1.7:** Two examples of interplanetary coronal mass ejections, as observed by the ACE (Advanced Composition Explorer) spacecraft. The shock is indicated by the red vertical line, while the ejecta is between the blue vertical lines. The region that lies between the shock and the ICME leading edge is the sheath region, formed by higly compressed and heated plasma. The shown plasma parameters are, from top to bottom: magnetic field magnitude, latitudinal (theta)- and longitudinal (phi)- components of the magnetic field in GSE angular coordinates, solar wind bulk speed, proton number density, proton temperature and plasma beta. The presented ejecta show different features. The event in Fig. (a) is a classic magnetic cloud, in which the magnetic field magnitude is enhanced and its angular components show a smooth rotation. Fig. (b) represents a complex ejecta, with a weak and irregular magnetic field. In both cases, the sheath region presents higly variable magnetic field, proton density, proton temperature and plasma beta.

Magnetic clouds can be considered as force-free fields [12], in which the electric current is parallel to the magnetic field (field-aligned current) and the magnetic force on the plasma is zero ($\mathbf{J} \times \mathbf{B} = 0$). The equation for the magnetic field in static conditions then reads

$$\nabla \times \mathbf{B} = \mu_0 \mathbf{J} = \alpha(r)\mathbf{B}\,. \tag{1.13}$$

Assuming that $\alpha$ is constant in all directions, the solution to the equation $\nabla^2\mathbf{B} + \alpha^2\mathbf{B} = 0$ describes magnetic clouds as flux ropes, magnetic structures with a cylindrical configuration and a two-component magnetic field, in which the magnetic field lines form helices whose pitch angle increases moving away from the axis.
Later studies have anyway shown that it is possible to find a pressure gradient within MCs [9], therefore the force-free and cylindrically symmetric model is to be seen as an approximation.

Since only about one-third of the detected ICMEs show magnetic cloud signatures, it is not well understood if this indicates that flux ropes and complex ejecta arise from different processes, or is it just due to observational effects: the eventual presence of MC signatures might depend on the trajectory of the spacecraft within the ICME structure. In addition, complex ejecta may be regarded as particular evolutions of magnetic clouds that interact with each other in the ambient solar wind. Moreover, often the MC represents only a portion of the region identified as an ejecta [34].

In this thesis, the study is performed on the sheath regions of ICMEs that show clear MC signatures, since the determination of the leading edge time for MCs is generally more precise compared to the case of complex ejecta.

# Chapter 2

# Sheath Regions

The solar wind forms sheath regions around the objects in the solar system: whenever a shock forms, the solar wind interacts with the obstacle through the sheath, by entering it and then flowing or piling up around the obstacle.

The majority of shocks observed in the solar wind are fast shocks. The fast shocks that take place in the solar wind also go under the general shock classification (see Section 1.3.2), based on the frame of reference: reverse shocks, which form upstream of quasi-stationary obstacles, such as planets or interstellar medium, and sometimes at the trailing edges of very fast expanding ICMEs, and forward shocks, that propagate ahead of drivers, such as ICMEs, through the solar wind.

Examples of sheaths that are found in the heliosphere are:

- **Heliosheath** (Fig. 2.1a), which is the region in the outer heliosphere where the solar wind dramatically slows down and starts to interact with the interstellar medium. It is comprised between the termination shock and the heliopause.

- **Cometosheaths**, regions that are downstream of cometary bow shocks, where the plasma population is made of solar wind, shocked particles and ionized atoms and molecules of cometary origin.

- **Magnetosheaths** (Fig. 2.1b), regions of space between the magnetopause and the bow shock of planetary magnetospheres, where the magnetic field generated by the planet becomes weak and irregular due to interactions with the solar wind.

- **Ionosheaths** (Fig. 2.1c), that form around unmagnetized bodies with atmospheres and are comprised between the ionopause (outer boundary of the ionosphere) and the bow shock that forms upstream from it.

- **ICME-sheaths** (Fig. 2.1d), that form ahead of fast interplanetary coronal mass ejections, are characterized by a complex internal structure and are often important drivers of magnetospheric activity and space weather events.

Sheaths in the heliosphere fall mainly in two categories: propagation sheaths, where the solar wind flows around the obstacle through the sheath in a quasi-stationary regime, and expansion sheaths, where the obstacle is expanding but not propagating with respect to the solar wind. In this view, ICME sheaths can be considered as hybrid sheaths, having

both properties of propagation and expansion sheaths, since the solar wind deflects from the side of the ejecta but tends to pile up instead of flowing.

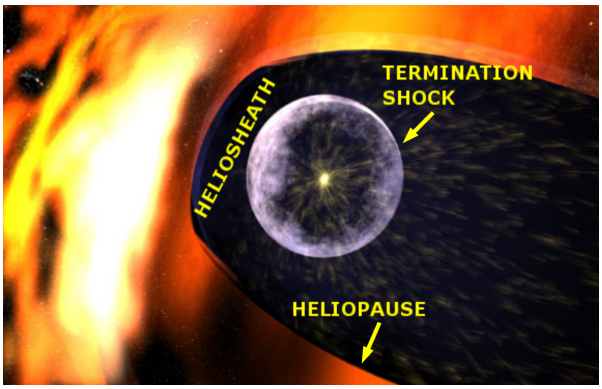


**(a)** Heliosheath

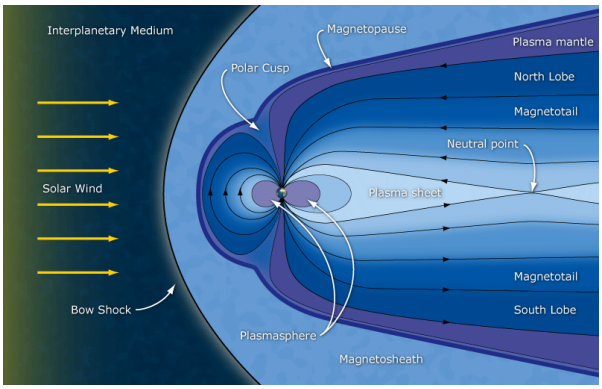


**(b)** Magnetosheath

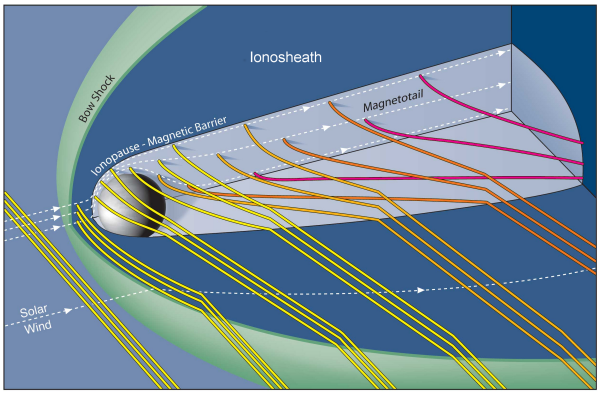


**(c)** Ionosheath

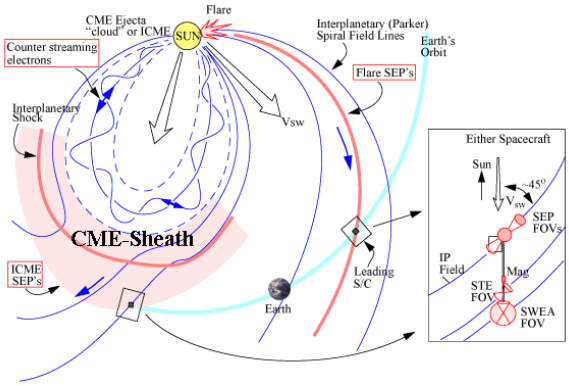


**(d)** CME-sheath

**Figure 2.1:** Representations of sheaths in the heliosphere.
a) The heliosphere, where it is possible to recognize the heliosheath located between the termination shock and the heliopause. Image credit: NASA Goddard.
b) Earth's magnetosphere, with its magnetosheath situated between the bow shock and the magnetopause. Image credit: ESA.
c) Venus' induced magnetosphere, with its ionotosheath situated between the bow shock and the ionopause.. Image credit: Laboratory for Atmospheric and Space Physics (LASP), University of Colorado.
d) Sketch of a CME travelling from the Sun, with its sheath region located between the shock and the ejecta leading edge. Image credit: Heliophysics Integrated Observatory (HELIO).

## 2.1 General sheath properties

Coronal mass ejection-driven sheath regions, due to their unique nature, have different geometrical properties compared to magnetosheaths and the heliosheath. ICMEs are obstacles that keep expanding in the heliosphere while they interact with the solar wind, therefore the spatial extension of ICMEs and ICME-driven sheaths can be roughly approximated as $\approx 10\%$ of the radius of curvature of the shock. This value shows that

ICME sheaths are thinner compared to magnetosheaths and the heliosheath, where the extension corresponds to $\approx 20\%$ of the radius of curvature of the shock [52]. Some characteristic length scales are from tens to a hundred AU for the heliosheath, from $10^{-4}$ AU (Mercury) to 0.1 AU (Jupiter) from planetary magnetosheaths, from 0.01 AU close to the solar corona to tens of AU nearby the termination shock for ICME sheaths [53].

Different kind of sheaths have anyway many similar features.

A plasma depletion layer (PDL) is a region observed in a sheath characterized by lower plasma density and higher magnetic field compared to the corresponding upstream values. The anticorrelation of the magnetic field with the plasma density makes it a slow-mode structure in MHD. PDLs stay as stable structures as long as the interplanetary magnetic field does not present major variations [68]. In the case of magnetosheaths, PDLs form when the IMF drapes around a planetary magnetosphere or piles up on the sunward side of the magnetopause, driving plasma away and leaving behind an impoverished region [69]. PDLs have been observed in few planetary magnetosheaths and in ICME sheaths, and have been predicted and modelled near the heliopause [53].

Magnetic field line draping and plasma depletion introduce a temperature anisotropy of $T_\perp > T_\parallel$, where $T_\perp$ and $T_\parallel$ are the temperatures in the parallel and perpendicular directions with respect to the magnetic field, respectively. When the temperature anisotropy satisfies the threshold condition

$$\frac{T_\perp}{T_\parallel} - 1 > \frac{1}{\beta_\perp}\,, \tag{2.1}$$

where $\beta_\perp$ is the plasma beta perpendicular to the magnetic field, mirror mode waves are generated [40]. These waves are very low frequency plasma wave phenomena, characterized by large amplitude spatially anticorrelated fluctuations in the magnetic field magnitude and in the plasma density. Mirror mode waves have been observed in all types of sheaths [53]. Large fluctuations in the plasma and in the magnetic field are common properties, since sheaths are very turbulent regions, even though different kinds of sheaths can have distinct time and amplitude scales in the fluctuations. For example, the heliosheath, being large compared to its boundary motions, takes a long time to respond to solar wind changes and its speed fluctuations are slower than in the case of narrower sheaths.

Small-scale motions of the termination and bow shocks can generate density compressions, that modify the shock speeds and normals. Such density fluctuations, anyway, are similar for both associated sheaths, suggesting that they are both characterized by similar small scale motions, despite the difference in size between the termination shock and planetary bow shocks [52].

Another common feature is represented by asymmetries, that can be generated by the magnetic field in the upstream flow or by a non-spherical obstacle. In particular, the magnetic field can drive an asymmetry when in the upstream it is at an oblique angle to the upstream flow direction [52]. As the field lines drape around the obstacle, they result more compressed on one side, and the consequent increase of the pressure gives rise to the asymmetry (see Fig. 1.3 for a representation of the asymmetric field-line draping around a fast CME).

A shock transfers energy from the bulk solar wind flow to the thermal plasma motion. In the case of a quasi-perpendicular shock (see Section 1.3.2), some of the ions encountering the shock are reflected upstream, then converted back to the shock where they are

heated again, generating a hot proton component and being more effective the higher the Mach number is (Eq. 1.5). The suprathermal ion component which forms can contain most of the total thermal energy of the solar wind in that region. The distribution of the reflected ions has been observed in several sheaths, and it seems to reach a higher percentage with the Mach number and with the distance from the Sun [52].

## 2.2 Coronal mass ejections-driven sheath regions

An ICME sheath is generally defined as the compressed region that is bounded by the shock and the ICME leading edge. ICMEs are not static obstacles, and their propagation through the ambient solar wind implies an expansion of the ICME itself and of the sheath region. The physical dimensions of an ICME sheath evolve therefore with the distance from the Sun. A main reason for this is that ICMEs change their shape in space due to kinematic expansion and interaction with the ambient solar wind, but preserving approximately a constant solid angle, at least close to the Sun [4]. This results in an increase in the dimensions of the ejecta and the sheath region perpendicular to the radial direction. Another reason is that ICME-shocks usually move faster than the corresponding ejecta [40], causing an increase in the spatial span and width of the sheath region.

### 2.2.1 Characteristics

As discussed above, ICME sheaths combine both aspects of propagation and expansion sheaths, and they tend to differ from other heliophysical sheaths for three main reasons: ICME sheaths are thinner than sheaths of other nature, the solar wind undergoes a reduced lateral deflection and it tends to pile up in front of ICMEs instead of flowing around it [61]. These properties are characteristics of an expansion sheath. The thinness is a result of the different geometry in the downstream flow between an expanding ejecta (that decreases its density) and a sheath which is propagating without expanding (and therefore with constant density). The rate of the lateral deflection of the solar wind flow around the ejecta decreases and the piling of the plasma around the ejecta edges increases when the later expansion of the ejecta becomes increasingly faster than the lateral flow deflection. [61].

Fig. 2.2) shows an example of an ICME-driven sheath region. It is a highly turbulent region, where both the magnetic field and the plasma parameters appear to undergo abrupt changes without ordered structure.

The shocks that precede fast-ICMEs are often quasi-perpendicular, but their Mach numbers are usually lower than the ones at planetary magnetosheaths [53]. The magnetic field lines drape around the obstacle because the IMF and solar wind plasma cannot penetrate the ICME. Therefore, ahead of the shock, the magnetic field has the form of a Parker spiral [40], but it becomes stretched and turbulent in the sheath region. The compression of the solar wind plasma in the sheath region in the direction perpendicular to the magnetic field may generate a PDL, because the plasma can flow along the draped field lines, and causes an enhancement in the plasma temperature in the perpendicular direction [40]. As a result, anisotropies in the ion distributions arise and mirror waves are generated 2.1. These features are observed at a high degree in shock-driving ejecta characterized by a MC structure, and at a reduced level in shock-driving complex

ejecta, but they are absent in all types of ICMEs without shocks [40]. The occurrence of these signatures may therefore depend on the level and extent of the compression of the upstream field by the ICME shock.

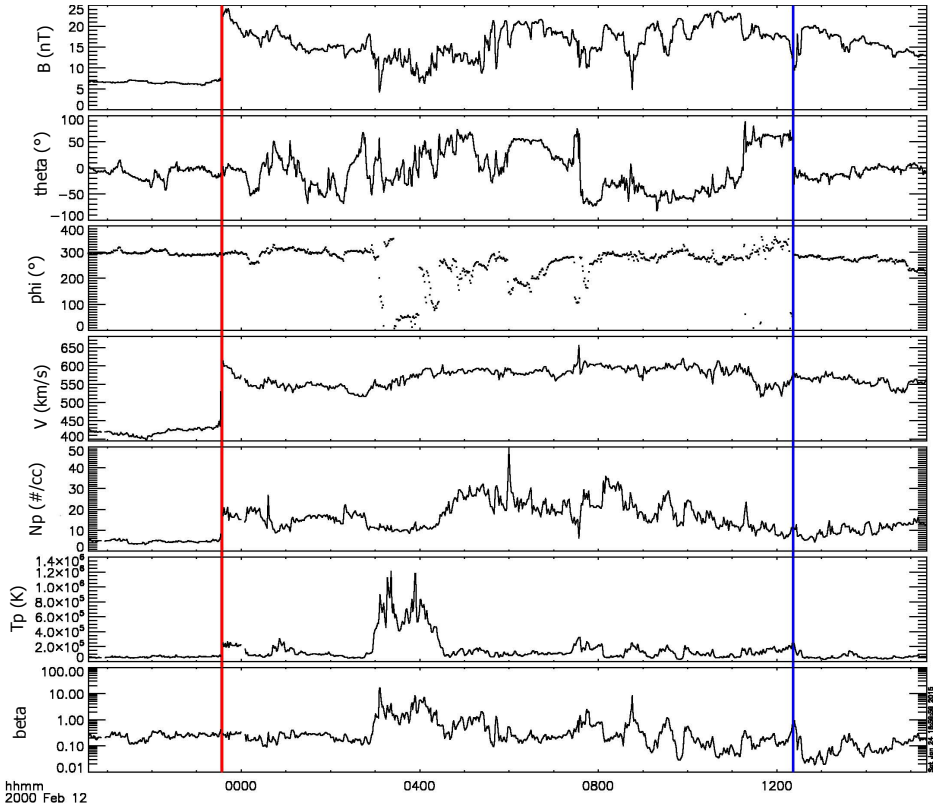


**Figure 2.2:** An example of coronal mass ejection-driven sheath region, as observed by the WIND spacecraft. The shock is indicated by the red vertical line, while the blue vertical line represents the ICME leading edge. The shown plasma parameters are, from top to bottom: magnetic field, theta- and phi- components of the magnetic field in GSE angular coordinates, solar wind bulk speed, proton number density, proton temperature and plasma beta. It is straightforward to notice the turbulent sheath nature in the values of magnetic field, proton density, proton temperature and plasma beta.

PDLs can develop only in the absence of strong local magnetic reconnection [76], because otherwise the plasma would connect with the ejecta field lines before being deflected away. Therefore, PDLs also become thinner if the reconnection rate increases.

The magnetic pressure pushes out and shapes the CME-pause. The plasma flow deflection angle that is measured in the sheath is sensitive to the pause, and therefore it depends on the direction of the magnetic field in the ICME and it is sensitive to the distance between the spacecraft and the ejecta's axis [6].

### 2.2.2 Sheath internal structure

As pointed out already, there are several differences between CME sheaths and other kinds of heliophysical sheaths, like planetary magnetosheaths. The internal structure of CME sheaths is complex, because during the CME long propagation from the Sun

through the heliosphere the IMF and the solar wind plasma gradually pile up in the sheath. Kaymaz and Siscoe [32] make an interesting comparison concerning the sheath structure:

> *ICME sheaths, even of halo CMEs, typically take five to ten hours to pass a spacecraft at one AU. This means that one should expect several significant deviations from the average-field direction during a typical sheath crossing. As a result, ICME sheaths are stratified, something like sedimentary rocks. For rocks the layers accumulate over time, and for ICME sheaths they accumulate over distance from the Sun.*

As a result of this IMF layering in the sheath, departures from the draping pattern arise, in which the field lines fluctuate from the general draping orientation in an irregular way [32]. The magnetic field does not strengthen from the shock to the ICME leading edge, on the contrary, it often tends to slightly decrease through its irregular profile towards the leading edge [32], most likely because of the sheath evolution as it moves in the heliosphere. The magnetic field close to the ejecta might have had time to be compressed and accreted through interactions at a shorter distance from the Sun compared to the one close to the shock front, which is less compressed and evolved.

Moreover, ICME sheaths are characterized by an east-west asymmetry: at 1 AU, the Parker spiral of the IMF is compressed on the western side of the ICME, therefore the magnetic field is stronger on that side [52]. This means that field lines in the east flanks should deviate more from the average Parker spiral orientation than those compressed in the west flanks [32].

Upstream of IP shocks, ultra-low frequency (ULF, $0.01 \div 0.05$ Hz) waves and higher-frequency ($\geqslant 1$ Hz) whistler waves had been observed, and the sheath regions downstream of shocks are characterized by irregular ULF fluctuations and regular higher-frequency waves, with frequencies that do not deviate from the upstream case [30]. In particular, ULF fluctuations have their strongest fluctuation power in the vicinity of the shock front and the ICME leading edge [33]. Studies performed over the ULF fluctuactions in the interplanetary magnetic field (IMF) and in the dynamic pressure ($P_{dyn}$) show different profiles within the sheath, where the IMF exhibits its highest ULF power in the vicinity of the shock and $P_{dyn}$ undergoes an enhancement near the ICME leading edge [33].

Because of the complex nature and constitution of the sheath region, it is possible to find fine structures within it. One clear example is given by the plasma depletion layers, discussed before. Observations of ICMEs have also found structures that have been named planar magnetic structures (PMS's) [47], which are characterized by the planarity within certain regions in the sheath of the magnetic field vectors, that remain all nearly parallel to a single plane despite the abrupt changes in direction and magnitude.

MHD simulations [39] divide the sheath region into two layers that can describe the transition of the ambient IMF to the field line draping configuration. In the first layer, the magnetic field lines remain coplanar and are unaffected by the draping process, while in the second layer the field lines start to rotate and align with the ejecta magnetic field. In this view, layer 1 can be thought as a PMS and layer 2 as a PDL, even though this two-layer structure has not been detected up to now.

### 2.2.3 Particle acceleration

Acceleration produced by CME-driven shocks is one of the processes that can give orgin to solar energetic particles (see Section 1.2). This phenomenon strongly depends on the geometry of the shock and on the structure of the sheath region.

Events in which SEPs are accelerated by CME-driven shocks that propagate throughout the heliosphere and are observed near Earth take place over a period of time that can last several hours or days, and for this reason are called gradual events [41]. These processes can accelerate electrons and ions of the local plasma up to energies of order $\gtrsim$ GeV [50]. From the accelerated particles it is possible to gain information about the energy spectra, the ionization states, the element abundances and other properties. The sheath region immediately behind shocks is characterized by strong acceleration.

A simulation of a fast CME propagating in an inhomogeneous solar wind [41] shows that the characteristics of the shock acceleration depend on the local shock Mach number and the angle between the shock normal and the upstream magnetic field. The interaction of a CME with a bimodal solar wind provokes a shock and a large postshock compression, and acceleration of electrons is possible in a small depression in the draping field lines near the equator, where the magnetic field lines bend first towards the equator and then towards the poles, in order to move around the ejecta. Moreover, there are strong velocity shears in the sheath that could cause Kelvin-Helmholtz instabilities, increasing therefore turbulence and particle diffusion, and in turn the rate of particle acceleration.

A more recent simulation [5] between 2 and 7 $R_\odot$ from the Sun found regions of substantial increase in the plasma density in the sheath, called piled up compression (PUC) regions, that are considered as a result of the lateral expansion of the CME. The observed density gradient between a PUC and the rest of the sheath is usually much larger than the density jump at the shock [37]. These PUCs, together with PDLs, are regarded as important structures within the sheath (Fig. 2.3). Even if PDLs and PUCs appear to be two phenomena that are in contrast, they can be both present within one single sheath. In this sense, the two opposing mechanisms work together: the CME pushes plasma ahead of it, causing the formation of a PUC, but also pushes the magnetic field lines ahead of it, driving plasma away, so that it is possible to observe a PDL. These two phenomena, when working together, may try to limit each other.

Whenever the ICME expansion speed is large, a large PUC will form in the lower corona. The high-density regions between a PUC and an interplanetary shock may favour the acceleration of charged particles in the lower corona. PUCs contribute therefore to particle acceleration in the sense that a CME that produces a larger PUC will produce a greater amount of SEPs [5].

As the CME expands from the solar corona, the sheath becomes wider and the PUC more dense. Behind the PUC, there is the expanding low-density ejecta. As the ejecta propagates, the distance between the PUC and the shock increases. When the CME reaches a distance of about $\sim 7R_\odot$, the PUC remains completely close to the ejecta, and becomes relatively thinner as the sheath expands [37].

### 2.2.4 Geomagnetic activity

Geomagnetic storms are magnetospheric disturbances characterized by enhanced particle fluxes in the ring current and radiation belts. Because of the field line compression

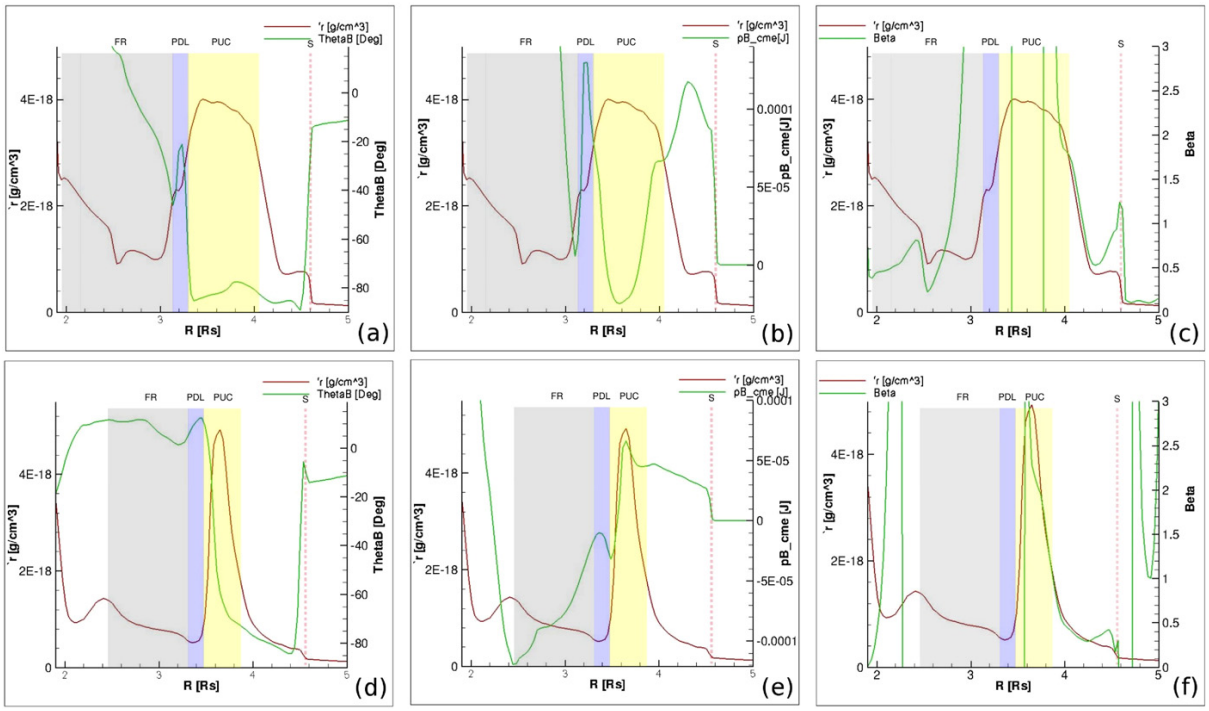


**Figure 2.3:** One-dimensional plots of two different flux-rope structures indicating the flux rope (FR) with light gray, PDL with light blue, PUC with light yellow shaded regions, respectively, while the red-dashed line represents the shock (S). The two rows show, for the two flux ropes, from left: plots for (a) density and $\theta_{Bn}$, (b) density and magnetic pressure, and (c) density and plasma beta. Image adapted from Das *et al.*, 2011 [5].

and the stronger magnetic field arising on the western part of ICMEs (see Section 2.2.2), this side results in being more geoeffective [52].

In solar physics, the east and west directions are defined according to the astronomical convention, that projects Earth's east and west directions onto the celestial sphere. When looking at the Sun from the northern hemisphere, the east is to the left and the west is to the right. As a consequence of this convention, the Sun rotates from east to west.

CME sheaths are important drivers of geomagnetic activity, it seems in fact that most CME-driven storms where the CME has a source longitude $\geqslant 40°$ are pure-sheath induced storms [60].

ICMEs are considered as the major cause of strong and intense storms on Earth, even if the Earth may not encounter them directly: since ICME-driven shocks are much larger than ICMEs themselves, it is possible for the Earth to come into contact with the disturbed solar wind after the shock and not with the ejecta [58].

The most widely used geomagnetic indices used for evaluating storms are the $D_{st}$ and $K_p$ indices [42]. The $D_{st}$ measures the decreases in the horizontal component of the geomagnetic field caused by the diamagnetic effect generated by the ring current, and it is proportional to the total kinetic energy of $20 - 200$ keV particles within the outer radiation belt. The minimum $D_{st}$ is then used in order to define the strength of a magnetic storm. The $K_p$ measures a wider and most general magnetic disturbance, taking into account a larger range of latitudes.

The z component of the IMF is a good indicator of geomagnetic storms: a value of $B_z \leqslant -10$ nT for a period of time longer than three hours is usually suggesting an intense storm, characterized by $D_{st} \leqslant -100$ nT [13]. An increase in the solar wind dynamic pressure can also bring a growth in the geoeffectiveness of N-S polarity clouds, where the field is initially northward and rotates southward [8].

It is reasonable to divide the storms caused by the sheath region and the ones caused by the ejecta, because each one of them can cause a storm independently from the other one, especially since their structures are different: sheath region-driven events are normally characterized by short-duration negative $B_z$ value and high dynamic pressure, while ejecta can cause events with long-duration negative $B_z$ value and, especially in the case of magnetic clouds, low dynamic pressure [22].

Sheath regions and post-shock streams cause the largest percentage of intense geomagnetic storms and are associated with an irregular behaviour of the plasma parameters in the solar wind and with a large $K_p$ activity, as well as with a significant compression of the magnetopause, which causes an enhancement in the losses of particles moving towards the dayside magnetosphere and therefore an obstacle to the development of the $D_{st}$ index at low latitudes [21].

In general, MC-events are characterized by low occurrence rate and low efficiency, but also by high geoeffectiveness (that is, high probability to give rise to a large and long-lasting southward IMF $B_z$ component); while sheaths are defined by low geoeffectiveness, but high occurrence rate and efficiency of magnetic storms [73].

A deep study of the overall sheath structure and the fine structures that it is possible to find within it is therefore essential for space weather forecasting and for getting a better knowledge of origin and evolution of the solar disturbances from the Sun to the Earth.

# Chapter 3

# Planar Magnetic Structures

The Sun's rotation winds the IMF lines into a spiral shape, which is known as the Parker spiral (Fig. 3.1). The IMF lines resemble an Archimedean spiral, which is described in polar coordinates at the equation $r = a + b\theta$, with $a$ and $b$ real numbers, and the $B_z$ component of the field is zero. This model describes very well the average IMF, but there are many local phenomena that can make the IMF deviate from the average Parker direction. The origin of such nonspiral fields can be associated, for example, with fast streams, transverse waves or CMEs [47].

In 1989, Nakagawa *et al.* [47], after analyzing the magnetic field in the solar wind in order to obtain further information about deviations from the Parker spiral, reported that a particular magnetic structure was found by the spacecraft Sakigake at a distance of $0.8 \div 1.0$ AU from the Sun. Its main characteristic was the close relationship between azimuthal and latitudinal angles of the magnetic field vectors. Such structure was named "planar magnetic structure" (PMS), since the magnetic field vectors are nearly parallel to a fixed plane that includes the spiral direction, but is inclined to the ecliptic plane from 30° to 85° [47].

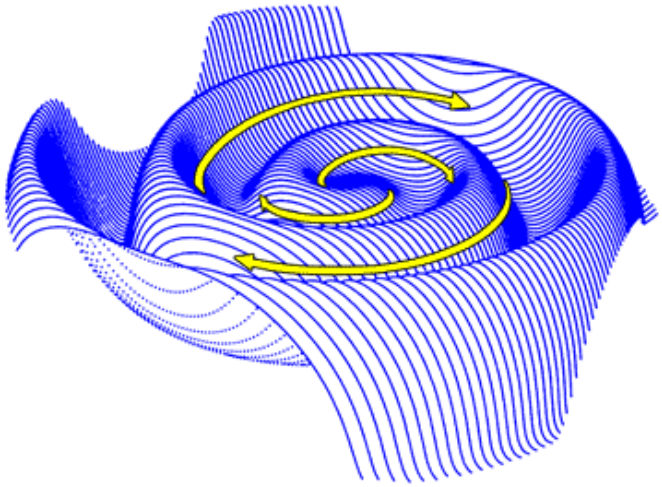

**Figure 3.1:** The heliospheric current sheet, which is often called the "ballerina skirt" because of its shape. The arrows are indicating the Parker spiral direction. Image credit: J. Jokipii, University of Arizona.

Any deviation from the average spiral condition of the solar wind and the IMF is important for studies of the solar-interplanetary physics and dynamics, and for the phenomenon of the solar wind-magnetosphere coupling [46].

A systematic study of PMS events [48] shows that many of them ($\sim 42\%$) occur in CME sheath regions, while others ($\sim 39\%$) are related to crossings of the heliospheric current sheet (HCS). This suggests that CMEs play a central role in the formation of PMSs. It has been suggested that they provoke the amplification and the alignment of pre-existing discontinuities by compression of the solar wind at the CME-driven shock. Moreover, PMS in CME sheaths could be also related to the draping of the magnetic field lines around the CME ejecta.

In addition, the presence of PMSs in sheath regions suggests that PMSs themselves can have a certain importance in space weather events, and a deep study of PMS formation and structure is necessary for a better understanding of the phenomenon.

## 3.1 PMSs: structure and properties

A PMS is defined as a feature in the solar wind in which all magnetic field vectors are parallel to a single plane that is inclined to the ecliptic plane. The field vectors are in a nearly two-dimensional space for a time interval of several hours and they are characterized by abrupt changes, in the sense that they take almost all directions parallel to a fixed plane. A PMS can be therefore considered as a laminar structure, composed of sheets that contain parallel but differently oriented magnetic vectors (Fig. 3.2).

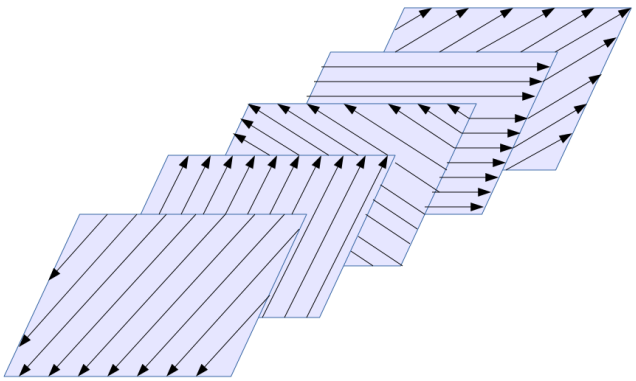

**Figure 3.2:** A sketch of the magnetic field configuration in a PMS. The planes containing the magnetic field vectors are separated by discontinuities that are parallel to the same plane [26].

### 3.1.1 Planarity of a PMS: the $\theta$ and $\phi$ angles

When a PMS occurs, the $\theta$ and $\phi$ angles are related [47], where the angles are defined as

$$\theta = \arctan\left(\frac{B_z}{\sqrt{B_x^2 + B_y^2}}\right) \tag{3.1}$$

and

$$\phi = \arctan\left(\frac{B_y}{B_z}\right). \tag{3.2}$$

The relation between the two angles can be studied through $\theta$-$\phi$ diagrams of the IMF (Fig. 3.3).

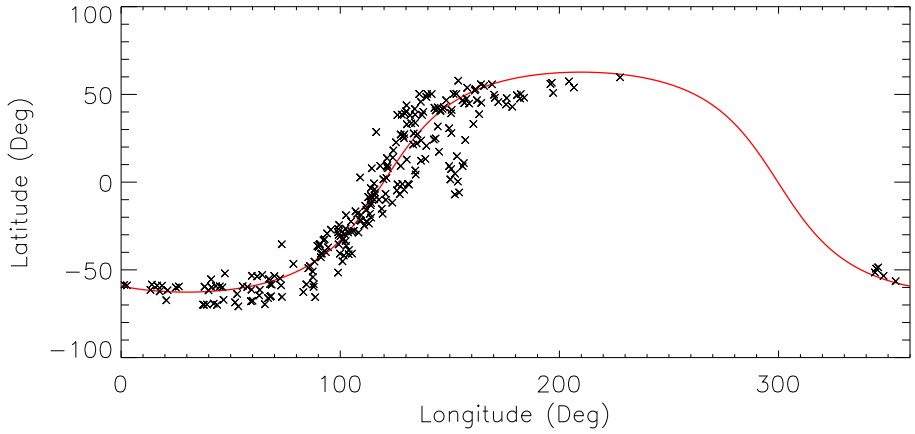


**Figure 3.3:** An example of $\theta$-$\phi$ diagram, showing a characteristic PMS wave-like curve described by Eq. 3.4.

In $\theta$-$\phi$ diagrams, the relationship between the two angles is represented by their arrangement along a wave-like curve that suggests the planar distribution of the field vectors. Considering a magnetic field $\mathbf{B}$ with components

$$\mathbf{B} \equiv (B_x, B_y, B_z) \equiv (B\cos\theta\cos\phi, B\cos\theta\sin\phi, B\sin\theta)\,, \tag{3.3}$$

its planarity to a plane with normal $\mathbf{n} \equiv (n_x, n_y, n_z)$ is described by the curve [46]

$$n_x\cos\theta\cos\phi + n_y\cos\theta\sin\phi + n_z\sin\theta = 0\,. \tag{3.4}$$

In this model, the inclination of the PMS plane to the ecliptic is represented by the value of $\theta_{max}$, the maximum value that $\theta$ assumes along a $\theta$-$\phi$ curve [47]. The wide distribution of $\phi$ over almost its whole region, with $0° < \phi < 360°$, shows that the vectors could take any direction within the planarity plane. The value $\theta = 0°$ in PMS curves tends to be intersected at about $\phi = 135°$ and $\phi = 315°$, which means that the Archimedean spiral direction is also included in the plane [47].

The resulting diagrams can be classified into three classes: those exhibiting a clear spiral field shape, those showing a wide distribution around one of the spiral directions and those showing a non-spiral structure [47]. In the last case, it is possible to find a subgroup of events in which the distribution of the magnetic field vectors is not casual, but rather located along a precise curve in the $\theta$-$\phi$ diagram. This is the case of PMSs, where the field vectors lie parallel to a plane that includes the spiral direction, but is inclined with respect to the ecliptic [47].

It is important to remark that the data points in a $\theta$-$\phi$ diagram are not following the PMS curve smoothly with respect to time, but they are rather randomly distributed along it, making often large jumps that reflect the abrupt changes in the field directions due to directional discontinuities [47].

The two-dimensionality of the field vectors in PMS events can be confirmed through the value of $|B_n|/B$ [46], where $B$ is the magnetic field magnitude and $B_n$ is defined as

$$B_n = \mathbf{B} \cdot \mathbf{n}\,, \tag{3.5}$$

that is the component of the magnetic field normal to the PMS plane.

A perfect planarity of the magnetic field vectors would imply $B_n = 0$, therefore a low value of $|B_n|/B$ is a good indicator of a situation in which the vectors are almost parallel to a plane.

### 3.1.2 Solar wind conditions related to PMSs

Several studies of solar wind parameters in correspondence of PMS events have been performed, in order to identify an eventual combination of plasma conditions that could give rise to planar structures.

The values of solar wind speed during PMS events do not differ significantly from the average solar wind velocity values. Velocity gradients have been found in a large number of events, although a clear correlation between PMSs and velocity gradients has not been found, since the encountered gradients can be both positive and negative (i.e., respectively, compression and expansion of the solar wind) and in many cases they occur after the PMS event has begun [47]. More generally, there is no evident pattern of the velocity profiles that would be connected to the generation of PMS [46].

During PMS events, ion densities are generally higher than usual, ion temperatures are normally equal or higher than the ones in the ambient plasma and magnetic field magnitudes do not experience significant changes with respect to the average values in the solar wind [47]. As a consequence, the plasma $\beta$ assumes high values in PMS events.

The directional discontinuities that are observed during the passage of a PMS can be rotational and/or tangential, with the highest percentage represented by tangential discontinuities [47].

Statistical studies show that PMSs are best observed when the Alfvén Mach number (Eq. 1.6) $M_A > 2$, the upstream plasma beta (Eq. 1.1) $\beta > 0.05$ [31] and if related to shocks, they tend to occur downstream of quasi-perpendicular shocks [28].

### 3.1.3 PMS duration and solar cycle dependence

PMSs typically last several hours. It is not easy to establish the exact duration of a PMS event, but their durations are typically less than 24 hours [47]. This upper limit is valid also in the case of PMSs that form after an interplanetary shock, because they are confined within the sheath region, that usually lasts less than 24 hours, compared to the average duration of 1-2 days of magnetic clouds. However, exceptions have been observed: for example, a PMS lasting $\approx 53$ hours [46] and one lasting $\approx 66$ hours [26].

It is difficult to define a minimum duration for PMS events, because in previous studies a lower limit has usually been imposed, ranging from 2 [47] [31] to 6 hours [27] [26].

The study of 667 PMSs between 1990 and 1998 [26], in which the minimum time span considered is 6 hours, shows that the peak in PMS durations corresponds to minimum possible event length established in the survey, suggesting that a large number of PMS

events may last less than 6 hours.

PMS are also characterized by a solar cycle dependence, being more common near solar maximum [29] and following therefore the trend in the occurrence rate of CMEs, that intensifies during solar maximum up to 4-5 CMEs per day.

## 3.2 PMS formation and related phenomena

PMSs are complex events that could be linked with different phenomena, and several hypothesis has been given in order to explain their origin, starting from the question of whether PMSs have their genesis on the Sun or in the interplanetary space. A number of solar and interplanetary hypotheses and PMS-related phenomena is presented below.

### 3.2.1 Solar phenomena related to PMSs

It is important to examine the connection between PMS events and phenomena of solar origin, because if PMSs have their source in some specific region on the Sun, then the characteristic features of that region should account for generation of PMSs. The projection of PMSs into the solar surface is therefore necessary in order to know what regions of the Sun could generate a PMS.

It is generally not straightforward to correlate interplanetary phenomena to something that happens in the photosphere, because of the complex magnetic field configuration and the irregular plasma motion in the solar surface, and it would be imprecise to assume that the interplanetary phenomenon just expanded radially from the photosphere.

Nevertheless, an attempt has been made [46], in order to correlate PMSs to solar flares, active prominences and filaments, by projecting the planar events onto a wide range of latitude ($\pm 30^\circ$) on the solar surface, not to miss a large amount of solar phenomena. No correlation between PMSs and any of those events has been found. Only 24% of the PMS events had a solar flare observed in a spatial span of $\pm 30^\circ$ in longitude around the PMS source region, and only 37% of PMSs were able to be connected, in the same spatial span, to active prominences or filaments.

Solar phenomena such as flares and processes rising from other active regions do not show an association to PMS events, but a large portion of planar structures can be related to the coronal neutral line at the source surface [46], and therefore to the HCS. In this view, tongue-like magnetic structures (Fig. 3.4) could be a good candidate.

The chronologically first hypothesis regarding PMS formation [47], in fact, relates PMS events to two basic magnetic field topologies: magnetic tongues and magnetic islands (i.e., plasmoids).

Magnetic tongues and plasmoids are both re-entrant field lines that form beneath the photosphere, rise up to the solar corona and are then transported into the interplanetary space by the solar wind. They both maintain their loop-like structure as they propagate through the heliosphere, but while magnetic tongues remain connected to the Sun and have a topology similar to the one of magnetic bottles, magnetic islands are disconnected from the Sun by reconnection and gain a closed topology.

If the re-entrant loops are initially all parallel to a plane that involves the Archimedean spiral and while they are transported by the solar wind they maintain their inclination, tongues and plasmoids would be observed as PMS events by the spacecraft. In addition,

the fact that both topologies can be formed by reconnection of open field lines could be consistent with the high number of PMS observation in the vicinity of the heliospheric neutral sheet, suitable for magnetic reconnection.

This model would also take into account the wide range of distribution of the $\phi$ angle, because the spacecraft would be able to observe all the orientations parallel to a plane while passing through different tongues, and is not in contradiction with the high number of PMS events recorded at the sector boundary.

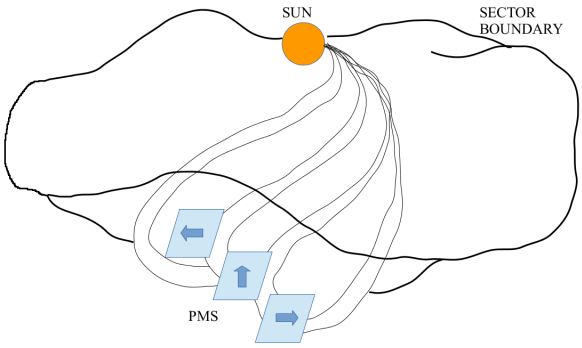


**Figure 3.4:** A sketch of the overall appearance of a PMS in the presence of magnetic tongues.

### 3.2.2 Interplanetary phenomena related to PMS

Several interplanetary candidates for PMS origin have been proposed. They include: compression of plasma by fast streams, sector boundary crossings, draping of magnetic field lines about some magnetic structure, propagation of a fast shock and alignment of pre-existing discontinuities caused by the passage of a shock [46].

Compression is essential for the formation of PMSs. There are two large-scale structures in the solar wind where compression frequently occurs: corotating interaction regions (CIRs), that form in the interplanetary space when fast solar wind streams, emanating from coronal holes, interact with slow ones, and sheath regions of CMEs. The observation of PMSs in CIRs can be related to the occurrence of PMSs in sector boundary crossings, since the two phenomena are often observed close to each other.

The compression hypothesis takes into account the fact that a large number of PMS events are found in correspondence of interplanetary shocks and/or ahead of CMEs. In this scenario, the characteristic compression of the magnetic field ahead of CMEs would reduce the field variations in the direction perpendicular to the surface of the ejecta, giving as result a structure that is quasi-parallel to the CME surface [48].

Another hypothesis for PMS formation is represented by the draping hypothesis, that accounts for the large-scale deviation from the Parker spiral direction in the IMF. A plasma cloud that moves with a high velocity causes the magnetic field lines to drape about itself, and as a result the solar wind microstructures and discontinuities might obtain a disposition that is parallel to the obstacle's surface [7]. This hypothesis would explain the presence of a high number of PMS events in CME sheaths, since they are the

regions where the IMF draping takes place.

The change in the directions of the field vector in the downstream region after the passage of a fast-mode shock is well explained by Neugebauer *et al.* [48]:

> *The passage of a fast-mode interplanetary shock across a tangential discontinuity (TD) both increases the amplitude ($|\Delta\mathbf{B}|$) of the discontinuity and changes its alignment so that it is more parallel to the shock.*

Thus, this process may explain the existence of planar magnetic structures in case the component of the magnetic field normal to the shock surface is small enough.

PMSs are frequently observed near the heliospheric sector boundaries, and PMSs and sector boundary crossings share several common properties in the magnetic field and plasma parameters [47]. Both events are characterized by high ion number density, large rotations of the magnetic field vectors and high variability of the field magnitude, that can occasionally approach a close-to-zero value. A statistical study of 35 PMS events during the period of investigation 1995-1997 [46] reports that 49% of them are projected in the neighbourhood of the sector boundary.

Another study [26] shows that 66 out of 667 PMS events studied during the period 1990-1998 coincides with corotating interaction regions (CIRs), that form in the interplanetary space when fast solar wind streams, emanating from coronal holes, interact with with the preceding slower streams. Of these 66 events, 35 PMSs are associated at the same time with HCS crossings.

Moreover, the same study carried out over 6 hours-minimum windows of data [26] shows that 35 out of 52 CMEs have an associated PMS. Of these, 24 PMSs are found in the sheath region (Fig. 3.5), while 28 PMSs coincide with the electron counterstreaming, i.e., the observation of suprathermal electrons with pitch-angle distributions aligned both parallel and antiparallel to the field, signature of the CME-ejecta. None of these events is connected to CIRs, while 28 PMS are linked to both CMEs and heliospheric boundary crossings.

Despite the number of phenomena that can be linked to PMSs, none of them can account for the formation of all planar structures that are observed. It appears, in fact, that about 35% of PMSs are not connected with the above mentioned solar wind features [26], and it seems that more than one formation mechanism is needed to explain the presence of PMSs on a general and complete scale.

Moreover, all the interplanetary phenomena listed above imply the presence of strong velocity gradients or jumps and/or shocks, but not all of the observed PMSs are accompanied by them. Moreover, these processes are not able to explain the wide range of distribution of the $\phi$ angle in a PMS event, that includes almost all directions as well as antiparallel orientations [46].

It should also be remarked that the occurrence rate and the characteristics of PMSs can change significantly with respect to their heliocentric distance. For example, considering the case of CME-driven PMS events, a multi-spacecraft study of the same CME from 1 to 93 AU [23] shows that, in general, the PMS planes get a better definition as the sheath region propagates farther out through the heliosphere.

## 3.3 Open problems

Many problems concerning PMSs still remain unsolved. Regarding the PMS origin, each model can explain some aspect of the phenomenon, but none of them can give a complete presentation of PMS formation processes. Anyway, as for the CME onset, there are probably many different mechanisms that create PMSs, and in such a case a number of different models would be needed.

Another problem is related to the PMS plane orientation, especially in the case of shock-related PMSs. Unsolved questions arise also about the preferable shock upstream conditions for the formation of a PMS in the downstream region, and about the relationship between planar structures and the turbulent interplanetary magnetic field.

Ultimately, great importance is represented by the eventual geoeffectiveness of PMS events, issue that is currently lacking systematic analysis.

The work presented in this thesis aims at giving a wider view of PMSs, by analysing flux-rope CME-driven sheath regions and studying the presence of PMSs within them. Shock and magnetic cloud properties are investigated in order to find the preferable conditions for the formation of PMS ahead of CMEs.

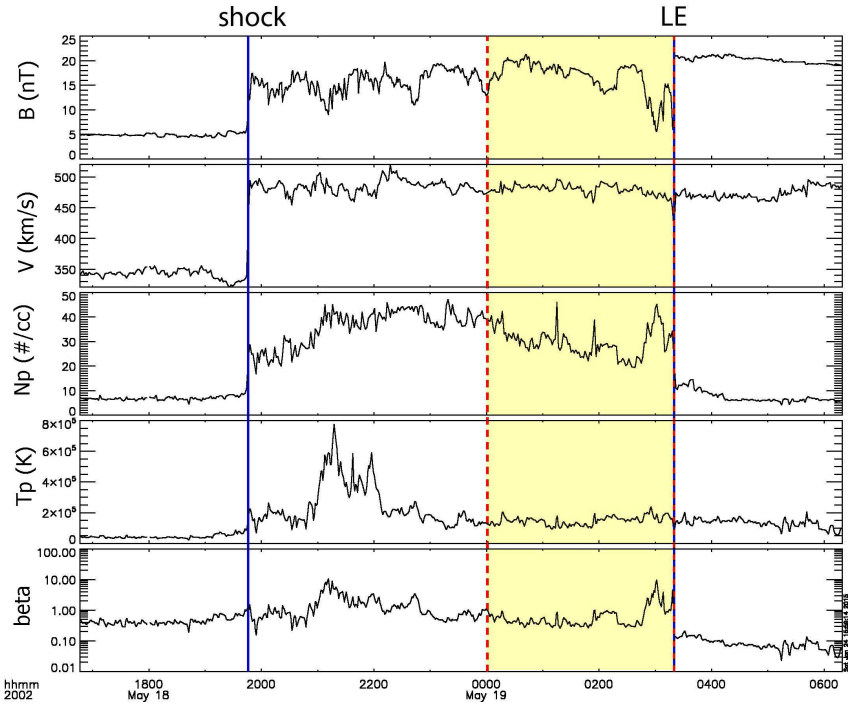


**Figure 3.5:** An example of PMS located in a CME-driven sheath region, as observed by the WIND spacecraft. The shown plasma parameters are, from top to bottom: magnetic field magnitude, solar wind bulk speed, proton number density, proton temperature and plasma beta. The PMS span is indicated by the yellow background. CME-driven sheaths are good regions for PMSs, because they are characterized by high values of proton number density, proton temperature and plasma beta and by abrupt changes in the field magnitude, compared to the ambient solar wind and the ejecta that follows the sheath, and by positive velocity gradients within the sheath, where the compression of the solar wind in such regions might be decisive for the existence of CME-driven PMSs [26].

# Chapter 4

# PMS Detection and Analysis

This thesis focuses on CME-associated planar magnetic structures that can be identified in CME-driven sheath regions. This chapter is based on the analysis performed over a number of sheaths, in which a first consistent amount of work is represented by the PMS detection. Then, the actual PMS analysis is introduced, where the sheath properties are evaluated in relation to the eventual presence and type of PMS(s) encountered.

## 4.1 Data set

The analysis introduced in this thesis is performed over 61 sheath regions (see Appendix A for the complete event list) associated to flux-rope-CMEs with interplanetary shocks. The IP shock and sheath region list is compiled by Dr. Emilia Kilpua with the help of the online ICME UCLA catalog (`http://www-ssc.igpp.ucla.edu/~jlan/ACE/Level3/ICME_List_from_Lan_Jian.pdf`), generated and maintained by Dr. Lan Jian at UCLA (now at University of Maryland, College Park and NASA/GSFC) and containing data during the time interval 1995-2009. The period of investigation covers a time range from 1997 to 2013. Solar wind and IMF measurements are taken from the Wind and ACE spacecraft.

The Wind satellite was launched in November 1994 by NASA, with the purpose of making accurate in-situ measurements of the interplanetary space and detecting interplanetary disturbances. It spent its first years at the Lagrangian point L1 and between 1999 and 2004 it acquired a complex petal-shaped orbit that brought it further and further away from the Sun-Earth line, until the completion of an L2 campaign in 2003. Since 2004, Wind has been operating at L1 [65]. The Advanced Composition Explorer (ACE) satellite was launched in August 1997 by NASA and it has been operating close to L1 since then.

In the work presented, the data from the Wind Magnetic Fields Investigation (MFI) [38] and the Wind Solar Wind Experiment (SWE) [49], both available from November 1994, are taken as main data source. The ACE Magnetic Field Investigation (MFI) [62] data, available from September 1997, and the ACE Solar Wind Electron Proton Alpha Monitor (SWEPAM) [43] data, available from February 1998, are used when the Wind measurements are not available or not reliable.

The provided sheath list depends mostly on the ACE data, therefore the times for the shocks and the magnetic cloud leading edges at Wind are searched visually. The search

"by eye" of the shock times is based on the abrupt increase in the values of magnetic field magnitude, velocity, plasma density and plasma temperature, according to the definition of fast forward shock (see Section 1.3.2). The magnetic cloud leading edge times are determined by looking for magnetic cloud signatures (see Section 1.3.1): a clear rotation of one or more magnetic field components ($B_x$, $B_y$ and $B_z$, reported in GSE coordinates [1]), a drop in the values of ion density and temperature and/or a brief peak of the plasma beta with a subsequent sharp decrease of its value.

The Wind and ACE data are obtained from the NASA Goddard Space Flight Center Coordinated Data Analysis Web (CDAWeb, `http://cdaweb.gsfc.nasa.gov/`).

For Wind, the MFI data are 1-minute resolution data and the SWE data are registered about every 1.5 minutes. For ACE, the MFI and the SWEPAM data are, respectively, 16-second and 64-second level 2 data.

## 4.2 PMS detection

As the first step, the key plasma parameters of every sheath region are obtained from CDAWeb, using Wind or ACE data according to the satellite that has been chosen for each event. The examined parameters are: magnetic field magnitude ($B$), magnetic field components in GSE coordinates ($B_x$, $B_y$ and $B_z$), theta and phi angles ($\theta$, Eq. 3.1 and $\phi$, Eq. 3.2), solar wind bulk speed ($V$), solar wind proton number density ($N_p$), proton temperature ($T_p$) and plasma beta ($\beta$).

As the two spacecraft do not record in a direct way all the parameters under consideration, it is necessary to extrapolate some of the missing parameters.

ACE data do not provide $\theta$ and $\phi$ values, therefore they are simply obtained using Eqs. 3.1 and 3.2 from the magnetic field components.

WIND data include the solar wind most probable thermal speed, defined as

$$V_{th} = \sqrt{\frac{2k_B T}{m}}\,, \tag{4.1}$$

therefore the value for $T_p$ is deduced from $V_{th}$.

The detection of PMSs in the sheath regions under analysis is achieved through the analysis of the magnetic field values and the implementation of the minimum variance technique.

### 4.2.1 $\theta$-$\phi$ diagrams

As pointed out in Section 3.1.1, the values of $\theta$ and $\phi$ are crucial for determining the presence of a planar magnetic structure. Therefore, a $\theta$-$\phi$ diagram spanning the whole sheath region is produced for each sheath. Three different outcomes are possible:

- **Case 1**: the magnetic field vectors are characterized by poor planarity, as a characteristic PMS curve is not possible to distinguish within the diagram (Fig. 4.1)

[1] In the Geocentric Solar Ecliptic (GSE) coordinates, the x-axis is represented by the Earth-Sun line and the z-axis passes through the ecliptic North Pole, being therefore perpendicular to the plane of the Earth's orbit around the Sun (positive North).

- **Case 2**: the points in the $\theta$-$\phi$ diagram are spread, but within the figure a PMS-like curve is possible to identify (Fig. 4.2)

- **Case 3**: the whole sheath region (or the largest part of it) shows good planarity, as the magnetic vectors are distributed according to a clear PMS-like curve (Fig. 4.3)

In Case 1, the magnetic field vectors do not follow a PMS curve. This is the case for eight of the analysed sheath regions.

In Case 2, an attempt is made in order to define the exact time span of the investigated PMS. Periods of roughly $\sim 3$ hours are plotted separately, with the aim of isolating the PMS-like curve. Then, the time span is slowly adjusted so that the maximum amount of data points that satisfy the same $\theta$-$\phi$ relation (Eq. 3.4) are included in the diagram. Generally, discontinuities in the values of $\theta$ and/or $\phi$ are used as the extremities of the eventual-PMS span. 31 events with the above described characteristics are found. Moreover, in four sheath regions two distinct PMS-like curves are possible to observe.

In Case 3, the time span of the suspected planarity event is adjusted only if there are data points that deviate from the wave-like curve and that belong to the leading and/or trailing part of the sheath, in order to maintain a unique block to be analysed. The remaining 18 events belong to this group.

Sheath regions usually have a temporal span of few hours, and since the list of sheath regions under analysis includes events that last $\approx 2$ hours, an interval of 1 hour is considered as the lower limit for PMS duration, criterion that takes into account the short duration of CME-driven sheaths and the minimum duration of PMS events observed in previous studies (see Section 3.1.3).

### 4.2.2 Mininum variance analysis

The next step in the PMS identification process is the determination of the normal $\hat{\mathbf{n}}$ of the selected time spans and the evaluation of the eventual planarity of the events.

In order to achieve this, the powerful tool known as minimum variance analysis (MVA, see Appendix B) is used. Sonnerup and Scheible [64] give a full presentation of the method in their article, where they make a short but clear description of the main goal of the procedure:

> *The purpose of the minimum variance analysis (MVA) is to find, from single-spacecraft data, an estimator for the direction normal to a one-dimensional or approximately one-dimensional current layer, wave front or other transition layer in a plasma.*

The MVA technique deals with non-ideal 1D layers, for which PMSs represent a good example, since the magnetic field vectors are almost planar to the PMS plane. After performing the MVA over the time spans under analysis, three new directions for the magnetic field are generated: maximum ($B_l$), intermediate ($B_m$) and minimum ($B_n$) variance (Fig. 4.4).

$B_n$ (Eq. 3.5) represents the magnetic field component to the PMS plane. The values of $B_n$ and $B$ (magnetic field magnitude) during the analysis periods are averaged, and the ratios $B_n/B$ are estimated for each event, in order to confirm the planarity of the

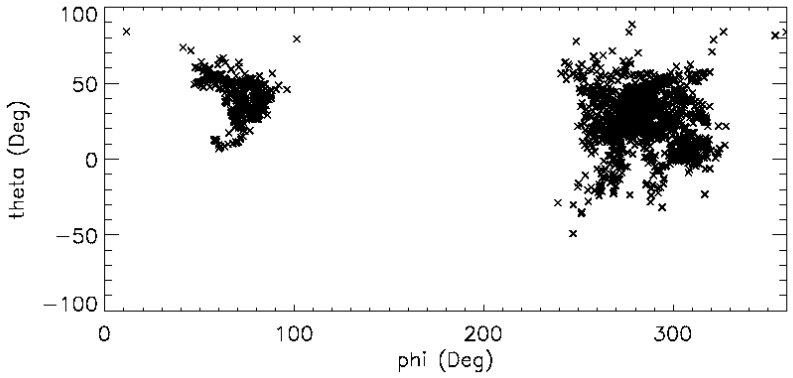


**Figure 4.1:** An example of $\theta$-$\phi$ diagram of a sheath region in which a planar magnetic structure is not found. In this case, the magnetic field vectors are all concentrated in two regions of the diagram, and a PMS-like curve is not found.

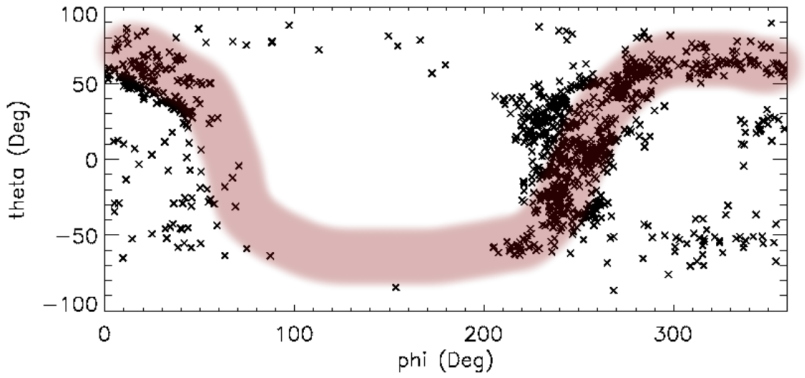


**Figure 4.2:** An example of $\theta$-$\phi$ diagram of a sheath region in which it is possible to recognize a PMS-like curve, highlighted in the shaded coloured region.

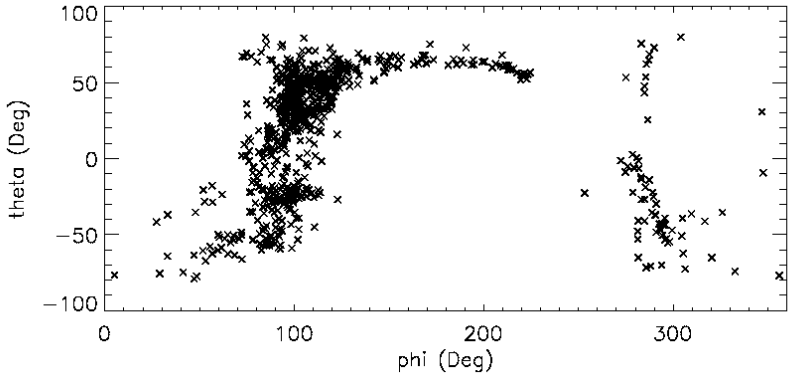


**Figure 4.3:** An example of $\theta$-$\phi$ diagram of a sheath region in which almost all magnetic field vectors are disposed along a PMS-like curve.

magnetic field vectors in the investigated sheaths.

The value of $B_n/B$ considered as the upper limit for the presence of a PMS in a sheath region is $B_n/B \leq 0.2$ [31]. In this way, it is possible to verify the actual presence of a PMS in each event and eventually adjust the PMS span.

It is worth to clarify that for the events characterized by a very good planarity (i.e., roughly $B_n/B \lesssim 0.1$), a small enlargement of the interval over which the MVA is performed still produces, in most of the cases, a value of $B_n/B \leq 0.2$, even if new data points that deviate significantly from the PMS curve are included. In such cases, the good value of the ratio is considered as due to an average between highly-planar and non-planar field vectors and, therefore, the points that deviate from the wave-like curve are excluded as much as possible from the analysis. This feature, in particular, makes the PMS span determination a task that cannot be fully-automated in the case of CME-driven sheath regions, where the temporal intervals considered last only a few hours.

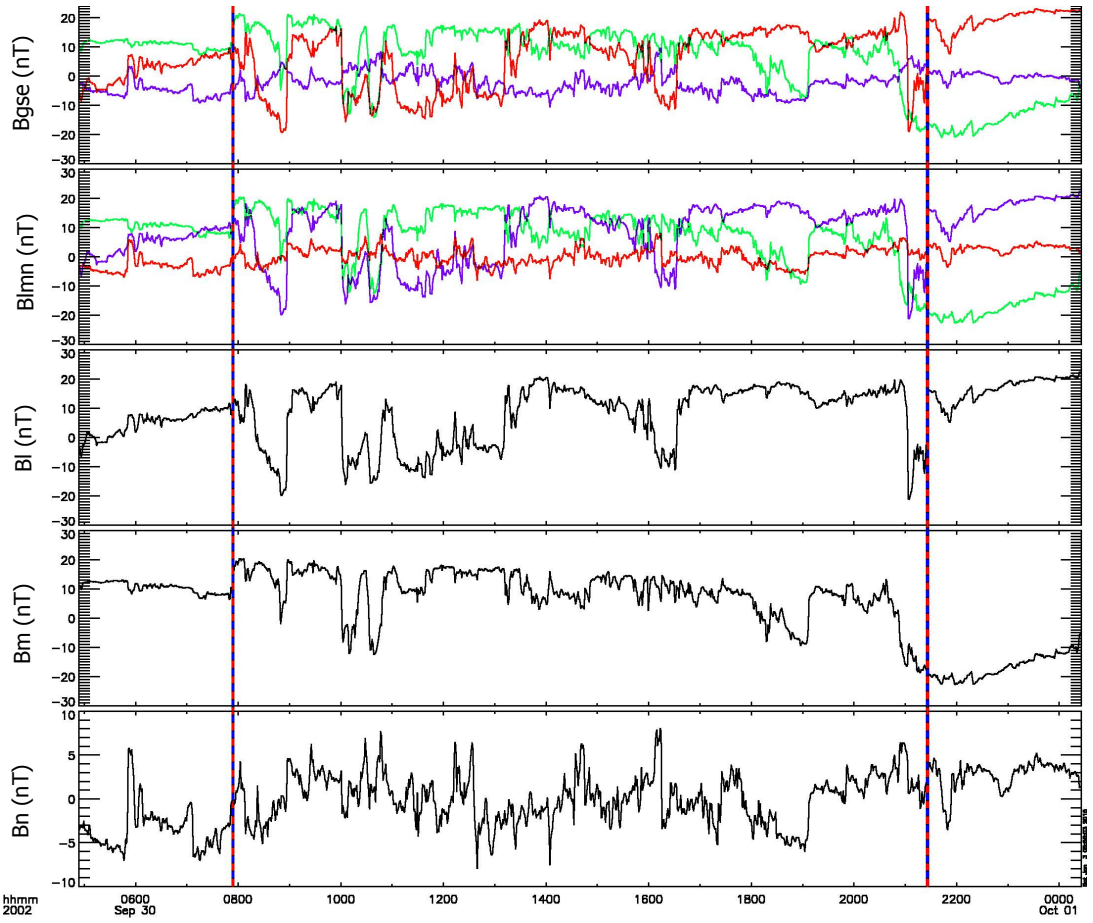


**Figure 4.4:** An example of magnetic field quantities obtained after performing the minimum variance analysis over an entire sheath region. The two vertical lines indicate, from left to right, the interplanetary shock and the magnetic cloud leading edge. The shown parameters are, from top to bottom: magnetic field components in GSE Cartesian coordinates (purple: $B_x$, green: $B_y$, red: $B_z$) as observed by the WIND spacecraft, minimum variance components of the magnetic field generated by the MVA, and then the three different directions reported separately: maximum ($B_l$, purple), intermediate ($B_m$, green) and minimum ($B_n$, red) variance directions.

The three magnetic field parameters generated by the MVA (maximum ($B_l$), intermediate ($B_m$) and minimum ($B_n$) variance directions) are associated with three eigenvalues ($\lambda_1$, $\lambda_2$ and $\lambda_3$, respectively) and three eigenvectors ($\hat{\mathbf{n}}_1$, $\hat{\mathbf{n}}_2$ and $\hat{\mathbf{n}}_3$, respectively, where $\hat{\mathbf{n}}_3 \equiv \hat{\mathbf{n}}$ represents the normal to the plane). The efficiency of the MVA technique can be evaluated by checking the intermediate-to-minimum eigenvalue ratio [55] (see Appendix B for the definition of the eigenvalues),

$$R = \frac{\lambda_2}{\lambda_3}\,. \tag{4.2}$$

It is noticed, in fact, that events with a good planarity ($B_n/B \leq 0.2$) and a low value of $R$ are highly unstable, meaning that a small change (order of minutes) in the MVA span usually brings to a large change in the normal vector and, in most cases, to a large change in the value of $B_n/B$, that assumes a value $> 0.2$. In this case, it is possible to argue that the suspected planar structure is not a PMS, but just a casual distribution over a PMS-like curve of field vectors in a restricted time span.

Being aware of this feature, it is noticed that a reasonable lower limit for the eigenvalue ratio is $R \geq 3$: all events with this minimum ratio do not present noticeable changes in the normal vector (and therefore in the PMS plane) under a small MVA-span change. In this way, two events that are initially listed as PMSs are moved to the non-PMS list.

The last criterion for the PMS detection process is related to the distribution of the $\phi$ angle in the resulting $\theta$-$\phi$ diagrams: as stated in Section 3.1.1, PMSs are characterized by a wide distribution of the $\phi$ angle, $0° < \phi < 360°$. In a few events that are reported as PMSs by the MVA, the field does not cover a large $\phi$ range (Fig. 4.5), since the magnetic vectors are distributed on a narrow window on the $\phi$ axis and spread along the $\theta$ axis. In such cases, the events are excluded from the PMS list, since they do not fulfil one of the basic definitions of a PMS. This is the case for two occurrences.

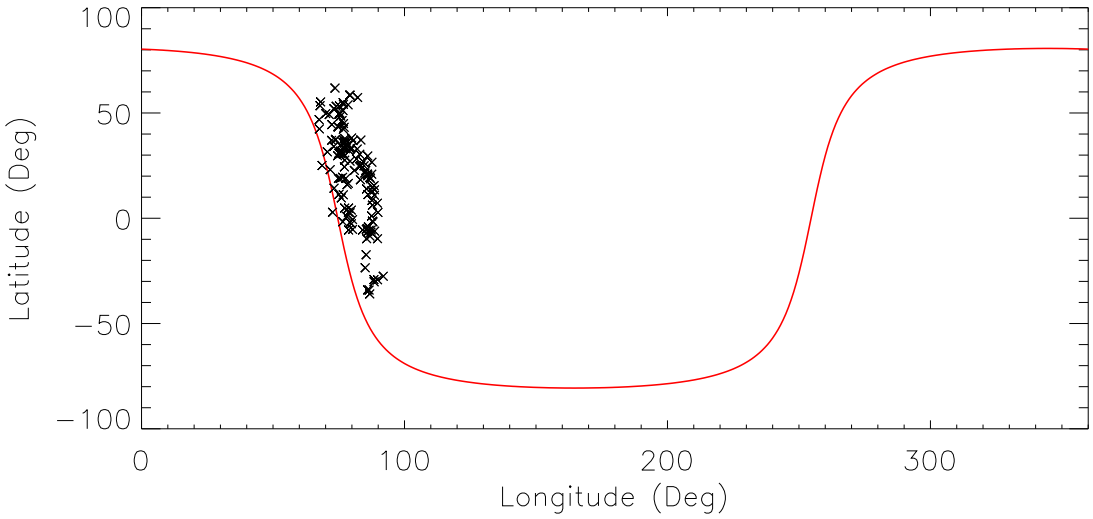


**Figure 4.5:** An example of event that shows a good planarity according to the MVA technique, but does not present a wide distribution of the magnetic field vectors over the $\phi$ angle. The red solid line shows the PMS curve described by Eq. 3.4. It is possible to notice the vertical structure in the $\theta$-$\phi$ diagram. This event is not listed as a PMS.

## 4.3 PMS analysis

The analysis performed with the help of the MVA technique over the 61 CME-driven sheath regions gives as result a total of 53 planar magnetic structures. First, the position of each PMS within its corresponding sheath region is determined and the encountered cases are divided into different groups. Later, a number of plasma parameters is analysed for each group, aiming to perform a statistical analysis.

### 4.3.1 PMS locations within the sheaths

In order to investigate the position of the encountered PMSs within the sheath, the sheath is separated into three regions (Fig. 4.6): near-shock, mid-sheath and near-LE (magnetic cloud leading edge) parts. In this way, it is possible to evaluate in which places within the sheath PMSs tend to occur, and if they follow a common pattern in their positions and extensions.

It is found out that all investigated PMSs are located next to the shock or next to the magnetic cloud leading edge, and eventually extending through the mid-sheath, except for three events (1999.04.16, 2005.05.15 and 2012.10.11) in which the PMS is exclusively located in the mid-sheath region. These events are therefore excluded from the statistical analysis.

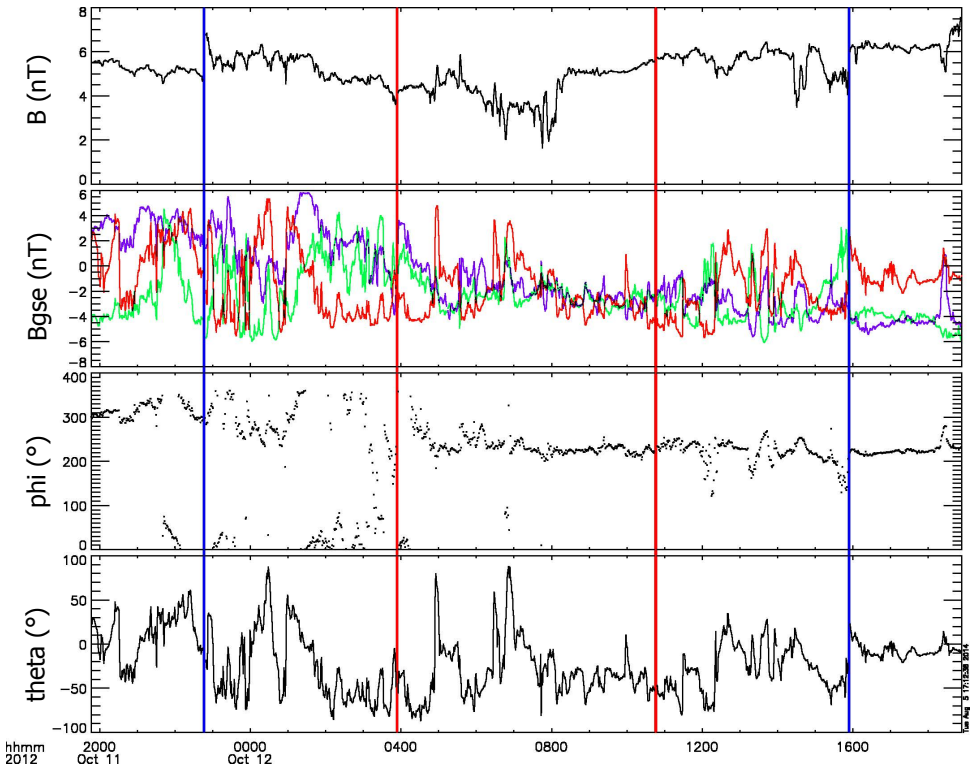


**Figure 4.6:** An example of sheath region, as observed by the WIND spacecraft, divided into three regions. The blue lines indicate the shock and the MC leading edge, while the red lines separate the sheath region into 30%-40%-30% of its duration. The plotted parameters are, from top to bottom: magnetic field magnitude, magnetic field components in GSE Cartesian coordinates, $\phi$ and $\theta$ angles.

The remaining 58 sheath events are divided into 4 groups (Fig. 4.7), according to the eventual presence and position of PMS(s):

- **Group 1**: no PMS encountered in the whole sheath (12 events)
- **Group 2**: one PMS located close to the interplanetary shock (9 events)
- **Group 3**: one PMS located close to the magnetic cloud leading edge (15 events)
- **Group 4**: one PMS covering the whole sheath region or 2 PMSs within one sheath (22 events)

The division of the events under analysis into three regions does not contribute strictly to the PMS grouping, meaning that a PMS span that starts from the shock and ends in the exact middle of the sheath region would still belong to Group 2, since the major part of the PMS lays in the near-shock part of the sheath. A similar argument applies to the elements of Group 3, while the criterion for events in Group 4 is that the PMS occupies an interval that covers $\gtrsim 85\%$ of the sheath region, or that two distinct PMSs are observed.

In the case of the four sheath regions that present two separated PMSs, for two events one PMS is located in the close-shock region and the other one is found in the close-LE region. In the remaining two events, the two PMSs are located in the close-shock and mid-sheath regions. For all sheaths of this kind, the two different PMSs do not share their plane orientations, meaning that the two structures could arise because of two different phenomena.

The subsequent step in the PMS analysis consists of a statistical analysis of a number of parameters, in order to try to associate different PMS groups with different sheath characteristics and properties of the associated shocks and magnetic clouds. The statistical analysis of the 61 sheath regions is performed by averaging the parameters under analysis within each PMS group, and by plotting the results through histograms. The standard deviation of the mean is obtained through the formula

$$\sigma_{\bar{x}} = \frac{\sigma}{\sqrt{N}}\,, \tag{4.3}$$

where

$$\sigma = \sqrt{\frac{1}{N-1}\sum_{i=1}^{N}(x_i - \bar{x})^2}\,, \tag{4.4}$$

$N$ is the number of elements in a PMS group and $\bar{x}$ is the mean value of the parameter under consideration within a group.

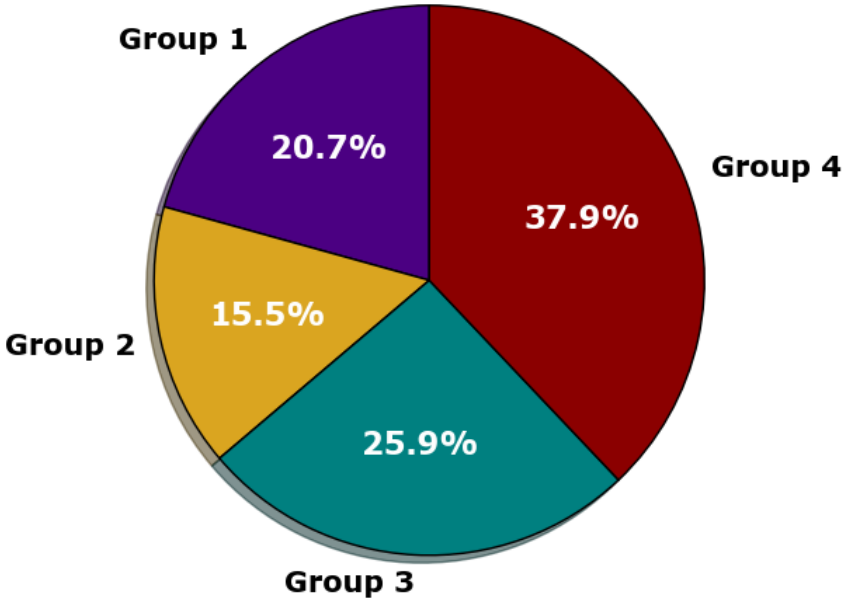


**Figure 4.7:** Chart that gives a quick visual cognition of the amount of elements classified into the four PMS groups during the analysis.

### 4.3.2 Shock parameters

The shock parameters investigated for the statistical analysis are:

- **Magnetic field ratio**, $B_d/B_u$, where the subscript $d$ indicates the shock downstream region and the subscript $u$ the upstream region.
- **Proton number density ratio**, $N_{pd}/N_{pu}$, where the subscript $d$ indicates the shock downstream region and the subscript $u$ the upstream region.
- **Magnetosonic Mach number** (Eq. 1.4), it gives a measure of the plasma velocity at the shock.
- **Shock angle**, the angle $\theta_{Bn}$ between the magnetic field and the shock normal. Its range of values is $0° \leq \theta_{Bn} \leq 90°$.

All the shock parameters have been provided by Erkka Lumme and Dr. Katerina Andreeova.

### 4.3.3 Sheath parameters

The quantities that are averaged during the whole sheath span (from the shock time to the MC leading edge time) are:

- **Magnetic field magnitude**, $<B>$.
- **Proton number density**, $<N_p>$.
- **Plasma beta**, $<\beta>$.

Moreover, the **sheath temporal duration** is calculated for each event.

### 4.3.4 Magnetic cloud parameters

The parameters calculated in the magnetic cloud are:

- **Mean velocity** calculated as a 3h average from the LE time onwards, $V_{LE}$. Since all sheath regions are compressed (and therefore the velocity slightly increase in the sheath), the velocity at the LE is a good measure of how fast the CME is.

- **Maximum magnetic field magnitude**, $B_{maxLE}$, is calculated as the maximum value that the magnetic field obtains from the LE and for the successive 3 hours.

- **Velocity gradient**, $\Delta V$, is the difference in velocity between the MC leading and trailing edges. A positive value of the velocity gradient indicates a compression of the cloud, while a negative $\Delta V$ represents an expansion of the cloud. Since only five clouds out of 58 present compression, the statistical analysis is performed exclusively on the expanding MCs.

The velocity gradient values in the period 1997-2009 (except for the event of August 17, 2003) have been compiled by Dr. Lan Jian at UCLA/IGPP (`http://www-ssc.igpp.ucla.edu/~jlan/ACE/Level3/ICME_List_from_Lan_Jian.pdf`).

## 4.4 Analysis of shock, sheath and MC properties related to PMS occurence

The results of the statistical analysis, that studies how occurrence of PMSs and their position depend on shock, sheath and MC properties, are presented below. The results are discussed, including possible sources of errors, and compared with the previous studies in Chapter 5.

### 4.4.1 Histograms for the shock parameters

The histograms of the investigated shock parameters are shown in Fig. 4.8. The histograms show averages, and the vertical lines in each bar represent the STD.

The magnetosonic Mach number (Eq. 1.4) is an indicator of the shock strength, and also the downstream-to-upstream magnetic field magnitude and proton density ratio can be used as proxies of the shock strength.

It is possible to note from the graphs that, generally, sheaths that present a PMS over the whole sheath span or two distinct PMSs (Group 4) are characterized by strong shocks, while sheaths that are lacking in planarity (Group 1) usually form in the downstream of weak IP shocks. The high value of the magnetic field ratio (Fig. 4.8a) for sheaths belonging to Group 1 can be partially attributed to an exceptional event, July 26, 2004, that presents an extremely high value of the magnetic field ratio $B_d/B_u = 4.6$ even though a PMS is not observed. The events of Groups 2 and 3 present intermediate characteristics. Mach number, $B$ and $N_p$ ratio give roughly the same results.

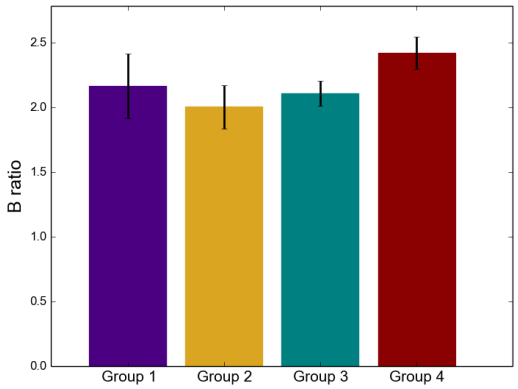


**(a)** Magnetic field ratio

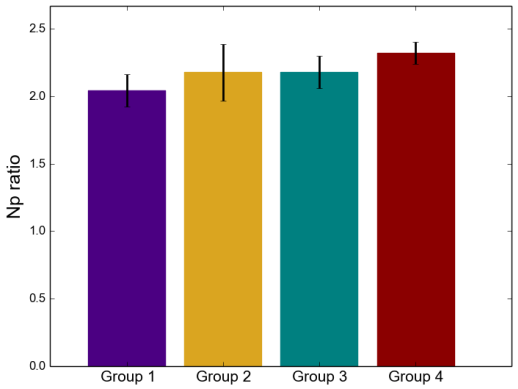


**(b)** Proton number density ratio

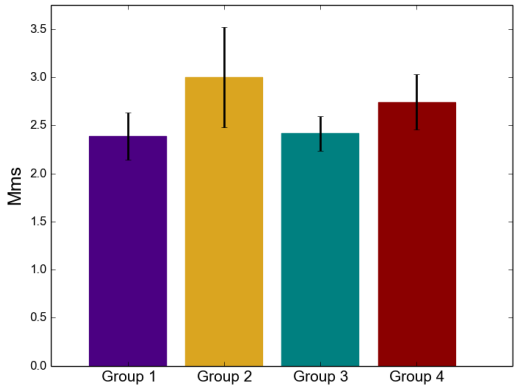


**(c)** Magnetosonic Mach number

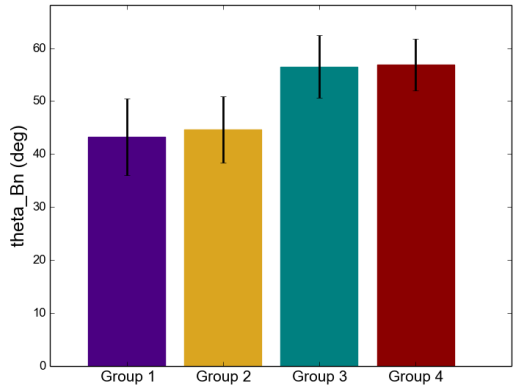


**(d)** Shock angle

**Figure 4.8:** The investigated shock parameters and their relation to PMS groups. Histograms show averages, and the vertical lines in each bar represent the STD. Group 1: no PMS, Group 2: PMS near the shock, Group 3: PMS near the MC leading edge, Group 4: PMS over the whole sheath or 2 PMSs.

It is worth to spend some additional words about the magnetosonic Mach number (Fig. 4.8c). The histograms reveal that the highest values of the Mach number were observed for Groups 2 and 4, that means, for the sheaths for which a PMS is observed in the immediate shock downstream. From this result, it is possible to argue that strong shocks characterized by high Mach numbers are more likely to produce a PMS immediately after the shock than weak shocks related to lower Mach numbers.

The shock angle $\theta_{Bn}$ between the upstream magnetic field and the shock normal (Fig. 4.8d) is larger for sheaths in Groups 3 and 4, meaning that quasi-perpendicular shocks tend to have a PMS in the vicinity of the MC leading edge.

### 4.4.2 Histograms for the sheath parameters

The histograms of the investigated average sheath parameters and their relation to PMS groups are shown in Fig. 4.9.

Again, it is possible to state that the sheaths characterized by the weakest parameters belong to Group 1, where a PMS is not observed. For the events presenting a PMS, the plasma parameters in the sheath are in agreement with the general solar wind conditions during PMS events (see Section 3.1.2): magnetic field magnitudes do not experience significant changes with respect to the average values in the solar wind (Fig. 4.9a), proton number densities are generally higher than usual (Fig. 4.9b) and the plasma $\beta$ assumes high values (Fig. 4.9c).

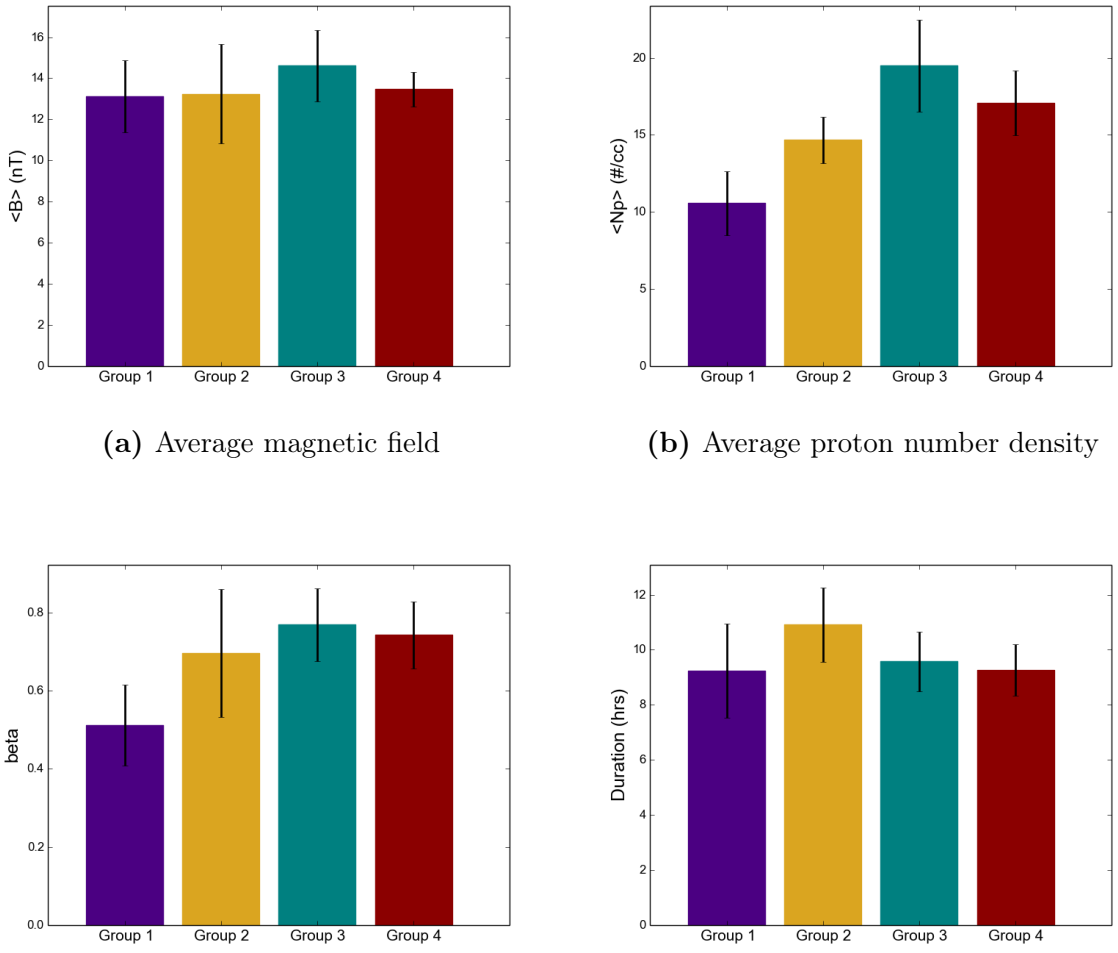


**(a)** Average magnetic field

**(b)** Average proton number density

**(c)** Average plasma beta

**(d)** Sheath duration

**Figure 4.9:** The investigated sheath parameters and their relation to PMS groups. The parameters are averaged during the whole sheath span. Histograms show averages, and the vertical lines in each bar represent the STD. Group 1: no PMS, Group 2: PMS near the shock, Group 3: PMS near the MC leading edge, Group 4: PMS over the whole sheath or 2 PMSs.

The results regarding the proton number density are interesting: the histogram shows the highest values of proton density for events belonging to Groups 3 and 4, which present a PMS in the vicinity of the MC leading edge. This suggests that there might be some mechanism responsible for the presence of a PMS in the end region of a sheath. Such a mechanism is hypothesized to be a piled-up compression region (see Section 2.2.3), and an eventual correlation between the two phenomena is investigated (see Section 4.4.4).

The graph that reports sheath duration data (Fig. 4.9d) outlines that the longest sheaths belong to Group 2 (PMS in the vicinity of the shock). Since PMSs usually last as much as or less than sheath regions, it is not surprising that the events that present a PMS over the whole sheath are among the shortest in duration. The long duration of sheaths in Group 2, on the other hand, suggests that the PMS that forms in the shock downstream in the events of Groups 2 and 4 is originated by the same mechanism, but for sheaths of Group 2 the PMS cannot be carried on to the MC leading edge because of the large temporal duration of the sheath. A short duration (Group 4) might indicate that the CME is cut close to its nose, while sheaths characterized by longer duration (Group 2) are associated to CMEs that are crossed close to the edge. The duration of a sheath also depends on the CME speed and geometry. It might even argued that the temporal duration itself of events belonging to Group 2 is due to the presence or the lack of a certain process along the trailing edge of the sheath region, i.e. for example the lack of a high-level compression that can shorten the sheath duration.

### 4.4.3 Histograms for the MC leading edge parameters

The histograms of the investigated MC leading edge parameters and their relation to PMS groups are shown in Fig. 4.10.

Non-PMSs (Group 1) show high velocities at the leading edge and high expansion rates of the clouds, while the magnetic field magnitude at the leading edge is usually low. The high value of the velocity gradient (Fig. 4.10b) for events in both Groups 1 and 4 suggests that a certain uniformity in the sheath structure (full planarity or full non-planarity) might lead to a high expansion rate in the MC.

The highest MC leading edge speed resulting for events in Group 1 is an interesting result. If the draping hypothesis is assumed, non-PMS sheaths should be the slower ones, since the faster the CME is the stronger the magnetic field line draping about the ejecta should be [44].

Sheaths belonging to Group 3 (PMS near the MC leading edge) present the highest values in the magnetic field magnitude at the leading edge, indicating a possible correlation between the two phenomena.

Finally, it is worth to mention that, for a number of events in the performed analysis, a PMS extends during the first hours of the MC. Even though such a feature is not investigated further because it goes beyond the scope of this thesis, it is argued that such findings can be due to an effective presence of PMSs right after the MC leading edge, or because some parts that have been defined as MC might actually be coronal loops that are dragged ahead of the flux rope, and hence show a PMS. Such a region can be defined as "MC front region", that is the region between the ICME and MC boundaries when they do not coincide , i.e., when the boundaries resulting from plasma and field data do not coincide with compositional/charge state signatures [34] and is different from the sheath

region.

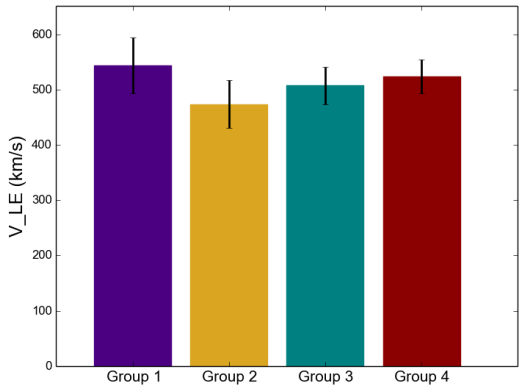


**(a)** Average velocity

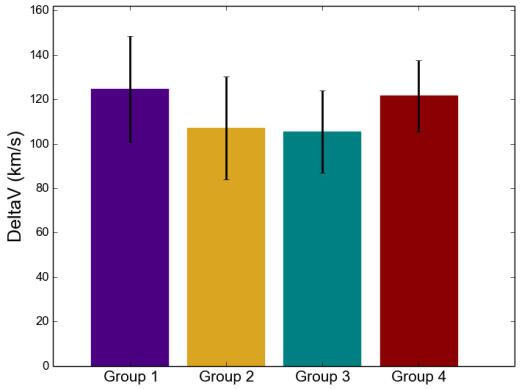


**(b)** Velocity gradient

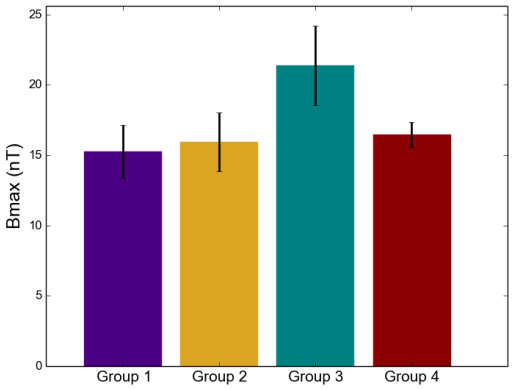


**(c)** Maximum magnetic field

**Figure 4.10:** The parameters calculated in the magnetic cloud and their relation to PMS group. The parameters in histograms (a) and (c) are calculated over the first 3 hours after the MC leading edge, while the speed gradient in histogram (b) is calculated over the whole MC span and only for expanding MCs. Histograms show averages, and the vertical lines in each bar represent the STD. Group 1: no PMS, Group 2: PMS near the shock, Group 3: PMS near the MC leading edge, Group 4: PMS over the whole sheath or 2 PMSs.

### 4.4.4 Correlation with PUCs

It is worth to mention that in 10 sheath regions a clear signature of PUCs (see Section 2.2.3) is observed. Such signature is represented by a substantial increase in the plasma density in the vicinity of the MC leading edge (Fig. 4.11). Since compression is essential in both PMSs and PUCs, an eventual correlation between the two phenomena is searched.

Among the 10 sheaths for which a PUC is found, six events belong to Group 3 (PMS near the MC leading edge) and four events are part of Group 4 (PMS over the whole

sheath or 2 PMSs).

All observed PUC events coincide with a PMS, therefore a correlation between the two phenomena can be argued.

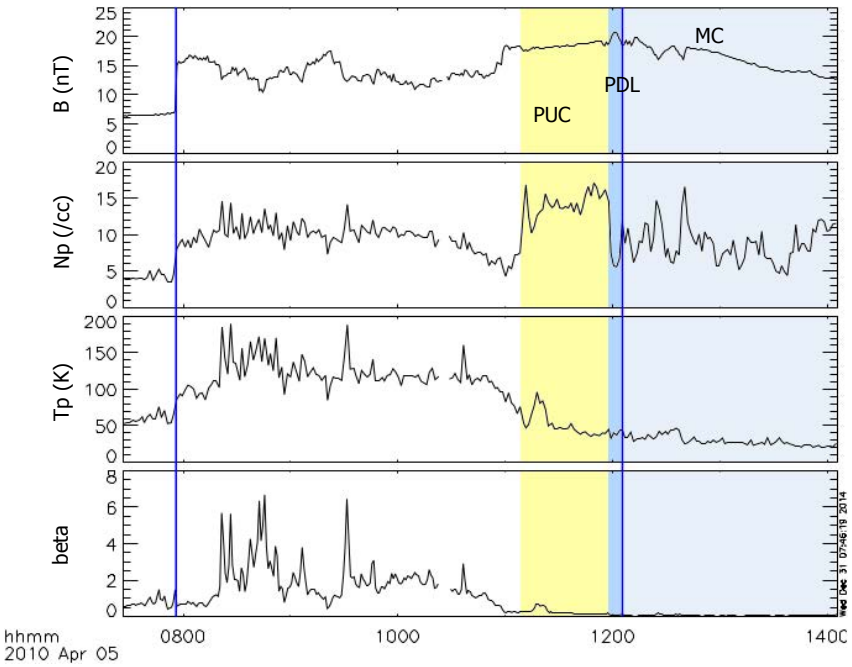


**Figure 4.11:** Example of a sheath region that presents a PUC signature, as observed by the WIND spacecraft. The shock and the leading edge are indicated by the blue vertical solid lines. The shown parameters are, from top to bottom: magnetic field magnitude, proton number density, proton temperature and plasma beta. The PUC, PDL and first 2 hours of the MC are highlighted by the shaded colored regions and labelled on the figure.

# Chapter 5

# Discussion of the Results

The main results of the analysis performed over the 61 sheath regions can be summarized as follows:

- PMSs are not always detected in CME-driven sheaths. PMSs are observed in 80% of the studied sheath events.
- PMSs tend to form in certain locations within the sheath: they are generally observed close to the CME-driven shock, close to the MC leading edge or they span the whole sheath.
- For a large number of cases, the highest level of planarity is found by taking the full period between the shock and the MC leading edge.
- It is possible to find more than one PMS within a single sheath: in such a case, encountered in 4 events, the two PMSs are well separated and characterized by different plane orientations. The first PMS is located close to the shock for all five events, while the second PMS is found in the mid-sheath in two events and close to the LE in the remaining three events.
- A PMS is found in the mid-sheath region for three events. These cases are not included in the statistical analysis.
- The duration of the examined PMS events ranges from 1.1 to 18.5 hours, with an average duration of 5.3 hours.
- The analysis of the shock parameters in relation to the different PMS groups shows that events characterized by a high magnetosonic Mach number are more likely to produce a PMS in the immediate shock downstream and that quasi-perpendicular shocks are more likely to produce a PMS close to the MC leading edge.
- The analysis of the sheath parameters in relation to the different PMS groups shows that non-planar events present low values of proton number density and plasma beta in the sheath region.
- The analysis of the MC parameters in relation to the different PMS groups shows that non-planar events are characterized by high leading edge speeds and high

negative velocity gradients (i.e. implying strong expansion), while sheaths that present a PMS close to the MC leading edge have high **B** magnitudes at the MC leading edge.

## 5.1 Sources of errors

The analysis is characterized by a number of conditions that may result in systematic errors.

The shock normal is a very uncertain parameter. In this work, it is calculated with the mixed mode normal method, that is an improved method of the magnetic field coplanarity theorem. The calculation of the mixed mode normals requires both plasma and field data [56]. Even if the normals calculated with both the mixed mode method and the MVA method are in acceptable agreement for most of the cases, there is still no way to determine a shock normal with high precision. For this reason, the magnetosonic Mach number $M_{ms}$ and the shock angle $\theta_{Bn}$, that directly depend on the calculated shock normal, are parameters that should be taken with caution. However, downstream-to-upstream magnetic field magnitude and proton density ratios shown in Fig. 4.8 show roughly similar results as the magnetosonic Mach number. This implies that the shock normal determined for the investigated events can be considered more or less reliable.

Another difficulty is represented by the choice of the MC leading edge times. As pointed out several times before (see Section 1.3.1), in-situ CMEs usually show only a subset of their characteristic signatures, and it is complicated to establish their boundaries. For this reason, while the detection of the shock times is an easy task, since they show clear signatures, the evaluation of the leading edges is not unambiguous, since in several cases different signatures are observed at different instants of time. Because of such issue, even if the research aims to find the most reasonable boundaries for the analysed sheath regions, there is still a possibility for a number of events to be studied within an imprecise time span. As a result, some of the events under study might fall under an incorrect PMS group, and also the planar ordering that is in some cases found in the first hours of a MC (see Section 4.4.3) might be due to a selection of the MC leading edge time that is not precise.

The last complication, but not least in importance, is represented by the unavoidable subjectivity of the PMS search, that is largely conducted "by eye". The evaluation of the PMS spans is performed by seeking for the best combinations of the ratios $\lambda_2/\lambda_3$ (as high as possible) and $B_n/B$ (as low as possible) and, at the same time, by visually looking for the periods for which the magnetic field vectors' ordering remains planar, i.e., the data points follow a PMS-like curve and the same $\theta$-$\phi$ relation. Nevertheless, the search is not characterized by unquestionable precision, and this aspect could affect the resulting PMS grouping.

## 5.2 Comparison with previous studies

The results obtained from the analysis are here briefly compared with previous studies.

The duration of the PMS events that are observed in the sheaths that present planarity (49 in total) goes from 1.1 to 18.5 hours, with an average value of 5.3 hours. This is in

agreement with previous studies, as, for example, the study of 35 PMS events from 1985 to 1987 [46] reports that the duration of PMSs ranges from 2 to 16 hours, with one extreme event that lasts more than two days, and with an average value of 6 hours. The amount of observed PMS events lasting less than 6 hours agrees with the argument by Jones and Balogh, 2000 [26] that a large number of events lasting less their minimum interval of investigation of 6 hours may exist. All studies reported here investigate PMSs on a general scale, and the connection of the observed PMSs to any large-scale structure in the solar wind is performed only after the detection.

Another observed feature in the analysis of this thesis that has been pointed out already in previous studies is represented by the fact that the most consistent MVA results are found by considering a span that includes the whole sheath region [55] [28]. In most of the cases, in fact, the highest values of the intermediate-to-minimum eigenvalue ratio and, at the same time, the lowest ones in the value of $B_n/B$ are observed when the entire sheath region is analysed through the MVA technique.

As stated in previous studies [28], PMSs are best observed in the case of quasi-perpendicular shocks, even though a number of quasi-parallel shocks that contain a PMS is detected.

A statistical study of 17 PMS events in the 2 hours downstream of a IP shock during solar cycle 23 [31] points out that PMSs are usually generated downstream of a strong shock with Alfvén Mach number (Eq. 1.6) $M_A > 2.0$. Even though the number examined in this work is the magnetosonic Mach number (Eq. 1.4) instead of the Alfvénic one, the results are in agreement, showing that PMSs are usually generated downstream of a strong shock with $M_{ms} > 2.5$.

The same study [31] shows that PMSs are not observed in the shock downstream when $M_A < 2.0$ and the plasma beta (Eq. 1.1) $\beta < 0.05$. Here the plasma beta is studied during the whole sheath span and not only in the 2 hours downstream of the shock, but the lowest values of the plasma beta are indeed found for non-planar sheaths, with $\beta < 0.5$.

## 5.3 Outlook

The innovation of this study is represented by the investigation of PMSs and their location within the associated sheath regions and by the study of shock, sheath and MC parameters in relation to the position of the PMS events within the sheath. In order to achieve this, the low minimum-PMS span of one hour is chosen with the aim to detect all the PMSs that are effectively present. This thesis presents therefore the most comprehensive analysis so far on PMSs in CME-driven sheath regions and their correlation with shock, sheath and MC properties.

The research aimed to correlate different kinds of PMSs to different mechanisms in the solar wind, and a satisfying result has been reached. PMS events that start from the IP shock time can be correlated to strong shocks, while PMSs in the vicinity of the MC leading edge can be associated to high ion densities and high magnetic field magnitudes at the beginning of the clouds. The high ion densities can be themselves correlated to compressed regions in the vicinity of the sheath trailing edge (PUCs).

In such a way, PMSs might help in the future to better understand sheath and MC

structures, goal that has already been the aim of a number of previous studies [28] [55].

However, the study here presented can be improved and extended in various directions.

A first improvement could be given by a PMS detection procedure characterized by a lower amount of subjective steps. In the work presented, in fact, a number of events has been classified by visual cognition. Some features might be calculated through an automated PMS search, even though a few analysis passages might still need an evaluation "by eye".

Another improvement could be represented by a better estimation of the shock normal. This could be achieved by a simultaneous analysis through different methods, in order to find an eventual agreement between various shock normal determination techniques.

The research could be then extended to include complex ejecta in the analysis procedure, in order to determine if the distinction between flux ropes and complex ejecta has any relevance to the study.

It is also intriguing to question if a combined-parameter analysis could carry out significant results, meaning that the study of more than one parameter per time might produce relevant outcomes. This would, however, need a larger statistics of sheath events than the one analysed in this thesis.

Another parameter that could be included in the sheath analysis is the number of discontinuities related to sheath and PMS intervals. Such analysis has already been carried out by Kataoka *et al.*, 2005 [31], in a time interval of 2 hours before and after the IP shock, but it could be extended to cover the whole sheath region span.

Another addition could be the detailed investigation of how PMSs are related to the spacecraft crossing distance from the CME center. This could be achieved by determining the impact parameter (i.e. the closest distance reached from the flux rope center) using e.g. the Grad-Shafranov reconstruction method, that estimates the orientation (invariant axis) and cross-section of magnetic flux ropes using single-spacecraft data [24], or perpendicular pressure profiles, given in the UCLA list and described by Jian *et al.*, 2006 [25].

A last extension for the presented study is represented by the evaluation of the eventual differences in plasma parameters between the PMS and non-PMS regions for events in which a PMS does not extend over the whole sheath, as this could highlight a number of fine structures responsible for the PMS formation and/or propagation within sheath regions.

# Appendix A

# Sheath Regions List

## A.1 Sheath parameters



| **Shock time (UT)** | **LE time (UT)** | **Spacecraft** | **<B> (nT)** | **<$N_p$> ($cm^{-3}$)** | **<$T_p$> (K)** | **<$\beta$>** | **Duration (hrs)** | **PMS group** |
|---|---|---|---|---|---|---|---|---|
| 1997.01.10, 00:52 | 1997.01.10, 04:58 | Wind | 9.16 | 12.85 | 84676.6 | 0.5 | 4.1 | 4 |
| 1997.11.06, 22:19 | 1997.11.07, 05:28 | Wind | 15.02 | 20.47 | 268847.8 | 0.87 | 7.15 | 4 |
| 1998.01.06, 13:29 | 1998.01.07, 02:50 | Wind | 12.22 | 23.62 | 106974.6 | 0.86 | 13.35 | 2 |
| 1998.05.01, 21:21 | 1998.05.02, 09:12 | Wind | 17.16 | 9.97 | 192903.3 | 0.3 | 11.85 | 4 |
| 1998.08.19, 18:40 | 1998.08.20, 09:00 | Wind | 10.03 | 17.35 | 47447.3 | 0.7 | 14.33 | 4 |
| 1998.09.24, 23:13 | 1998.09.25, 06:17 | ACE | 20.84 | 8.62 | 440510.8 | 0.26 | 7.07 | 4 |
| 1998.10.18, 19:29 | 1998.10.19, 04:22 | Wind | 12.41 | 49.28 | 93943.4 | 1.59 | 8.88 | 4 |
| 1999.02.18, 02:47 | 1999.02.18, 10:28 | Wind | 25.76 | 6.4 | 528420.6 | 0.22 | 7.68 | 1 |
| 1999.04.16, 10:35 | 1999.04.16, 15:21 | ACE | 8.03 | 36.1 | 71330.3 | 3.13 | 4.77 | - |
| 2000.02.11, 23:34 | 2000.02.12, 12:22 | Wind | 16.46 | 17.7 | 180065.4 | 0.62 | 12.8 | 4 |
| 2000.02.20, 21:04 | 2000.02.21, 05:27 | Wind | 12.79 | 26.33 | 154373.4 | 1.06 | 8.38 | 4 |
| 2000.08.11, 18:11 | 2000.08.12, 04:45 | ACE | 20.69 | 8.43 | 247166.2 | 0.17 | 10.57 | 3 |
| 2000.09.04, 12:45 | 2000.09.04, 21:45 | ACE | 7.86 | 9.08 | 51420.9 | 0.29 | 9 | 1 |
| 2000.10.03, 01:02 | 2000.10.03, 17:00 | Wind | 13.27 | 9.44 | 84224.8 | 0.21 | 15.97 | 4 |

| | | | | | | | | |
|---|---|---|---|---|---|---|---|---|
| 2000.10.12, 22:33 | 2000.10.13, 05:52 | Wind | 16.25 | 18.1 | 163689.2 | 0.85 | 7.32 | 4 |
| 2000.11.06, 09:30 | 2000.11.06, 22:27 | Wind | 11.49 | 12.25 | 259232.4 | 0.6 | 12.95 | 3 |
| 2001.03.19, 11:34 | 2001.03.19, 18:01 | Wind | 16.33 | 13.08 | 129870.2 | 0.28 | 6.45 | 3 |
| 2001.03.27, 17:15 | 2001.03.27, 21:44 | ACE | 22.12 | 20.05 | 219258.1 | 0.33 | 4.48 | 4 |
| 2001.04.11, 13:15 | 2001.04.11, 22:14 | ACE | 23.18 | 22.71 | 492034.3 | 0.83 | 8.98 | 3 |
| 2001.04.21, 15:06 | 2001.04.21, 23:35 | ACE | 6.63 | 26.95 | 39537.6 | 0.94 | 8.48 | 1 |
| 2001.04.28, 04:31 | 2001.04.28, 15:49 | ACE | 16.69 | 8.35 | 433548.7 | 0.67 | 11.3 | 4 |
| 2001.05.27, 14:16 | 2001.05.28, 04:00 | ACE | 11.11 | 3.47 | 193711.7 | 0.18 | 13.73 | 1 |
| 2001.09.29, 09:05 | 2001.09.29, 11:30 | ACE | 10.55 | 5.43 | 523129.9 | 0.97 | 2.42 | 4 |
| 2001.10.31, 12:53 | 2001.10.31, 19:50 | ACE | 7.39 | 19.64 | 51550.5 | 0.81 | 5.25 | 2 |
| 2002.02.28, 04:03 | 2002.02.28, 16:41 | ACE | 9.55 | 20.95 | 95138.5 | 0.87 | 12.63 | 3 |
| 2002.03.23, 11:24 | 2002.03.24, 11:39 | Wind | 10.21 | 9.67 | 67813.2 | 0.26 | 24.25 | 1 |
| 2002.05.18, 19:46 | 2002.05.19, 03:20 | Wind | 16.06 | 33.12 | 202591.6 | 1.2 | 7.57 | 3 |
| 2002.08.01, 05:19 | 2002.08.01, 12:50 | Wind | 14.1 | 7.72 | 154653.8 | 0.2 | 7.52 | 1 |
| 2002.09.30, 07:54 | 2002.09.30, 21:26 | Wind | 17.67 | 33.45 | 87926.9 | 0.41 | 13.53 | 4 |
| 2002.11.16, 23:04 | 2002.11.17, 06:45 | ACE | 10.18 | 8.83 | 130264.2 | 0.4 | 7.68 | 1 |
| 2003.03.20, 04:20 | 2003.03.20, 08:30 | ACE | 10.46 | 3.69 | 474796.1 | 0.69 | 4.17 | 1 |
| 2003.08.17, 13:41 | 2003.08.18, 06:00 | ACE | 19.21 | 12.96 | 97960.2 | 0.17 | 16.32 | 2 |
| 2003.11.20, 07:27 | 2003.11.20, 10:48 | ACE | 28.27 | 16.97 | 349019 | 0.4 | 3.35 | 3 |
| 2004.07.22, 09:45 | 2004.07.22, 13:01 | Wind | 10.69 | 13.64 | 216049.7 | 1.05 | 3.27 | 1 |
| 2004.07.24, 05:38 | 2004.07.24, 12:05 | ACE | 18.93 | 10.3 | 188290.2 | 0.22 | 6.45 | 2 |
| 2004.07.26, 22:28 | 2004.07.27, 01:40 | ACE | 17.95 | 3.42 | 931708.9 | 0.36 | 3.2 | 1 |
| 2004.08.29, 09:08 | 2004.08.29, 18:31 | Wind | 7.29 | 11.35 | 54526 | 0.57 | 9.38 | 2 |
| 2005.05.15, 02:11 | 2005.05.15, 05:32 | Wind | 20.1 | 20.31 | 1277274 | 4.56 | 3.35 | - |
| 2005.06.14, 17:56 | 2005.06.15, 05:15 | Wind | 9.47 | 10.49 | 169937.2 | 0.83 | 11.32 | 4 |
| 2005.07.10, 02:42 | 2005.07.10, 10:10 | Wind | 23.25 | 20.87 | 290972.1 | 0.37 | 7.47 | 1 |
| 2005.07.17, 00:53 | 2005.07.17, 15:17 | Wind | 9.16 | 13.07 | 170391.6 | 1.18 | 14.4 | 1 |
| 2005.09.02, 13:50 | 2005.09.02, 18:43 | Wind | 14.82 | 9.16 | 440813.1 | 0.71 | 4.88 | 4 |
| 2006.04.13, 11:12 | 2006.04.13, 15:15 | ACE | 9.9 | 15.62 | 134256 | 1.05 | 4.05 | 4 |

| | | | | | | | | |
|---|---|---|---|---|---|---|---|---|
| 2006.12.14, 13:52 | 2006.12.14, 22:27 | Wind | 13.46 | 10.95 | 857481.1 | 1.74 | 8.58 | 4 |
| 2007.11.19, 17:16 | 2007.11.19, 23:06 | ACE | 7.1 | 21.54 | 54473.3 | 1.03 | 5.83 | 4 |
| 2009.02.03, 19:21 | 2009.02.04, 02:13 | Wind | 9.65 | 12.94 | 35421.3 | 0.23 | 6.87 | 4 |
| 2009.12.12, 04:38 | 2009.12.12, 18:07 | Wind | 5.4 | 12.38 | 27745.6 | 0.44 | 13.48 | 2 |
| 2010.04.05, 07:56 | 2010.04.05, 12:06 | Wind | 15.08 | 10.5 | 709807.4 | 1.38 | 4.17 | 3 |
| 2010.05.28, 01:53 | 2010.05.28, 19:50 | Wind | 6.6 | 19.46 | 49411.6 | 0.95 | 17.95 | 3 |
| 2011.03.29, 15:10 | 2011.03.30, 00:21 | Wind | 6.97 | 23.55 | 47194.5 | 1.02 | 9.18 | 3 |
| 2011.09.17, 02:57 | 2011.09.17, 15:40 | Wind | 9.38 | 13.51 | 116720.9 | 0.84 | 12.72 | 3 |
| 2012.04.23, 02:15 | 2012.04.23, 16:43 | Wind | 11.3 | 23.58 | 72255.9 | 0.65 | 14.47 | 4 |
| 2012.06.16, 19:35 | 2012.06.16, 22:15 | Wind | 23.98 | 52.52 | 115262.5 | 0.39 | 2.67 | 3 |
| 2012.07.14, 17:39 | 2012.07.15, 06:19 | Wind | 13.05 | 16.51 | 345457.7 | 1.78 | 12.67 | 2 |
| 2012.10.08, 04:12 | 2012.10.08, 17:15 | Wind | 12.9 | 15.03 | 119669.5 | 0.52 | 13.05 | 3 |
| 2012.10.11, 22:47 | 2012.10.12, 15:52 | Wind | 5.01 | 5.14 | 106982.2 | 0.8 | 17.08 | - |
| 2012.10.31, 14:28 | 2012.10.31, 23:34 | Wind | 9.71 | 24.28 | 100085.9 | 1.1 | 9.1 | 3 |
| 2012.11.23, 20:51 | 2012.11.24, 11:34 | Wind | 11.35 | 14.68 | 98573.6 | 0.46 | 14.72 | 2 |
| 2013.03.17, 05:22 | 2013.03.17, 11:55 | Wind | 14.34 | 10.68 | 373634.7 | 0.96 | 6.55 | 2 |
| 2013.04.13, 22:13 | 2013.04.14, 16:40 | Wind | 10.3 | 13.85 | 130230.6 | 0.75 | 18.45 | 4 |
| 2013.07.12, 16:43 | 2013.07.13, 04:56 | Wind | 8.97 | 5.83 | 179212.4 | 0.98 | 12.22 | 3 |

**Table A.1:** List of the 61 investigated sheath regions with associated sheath parameters. The given quantities, from left to right, are: shock time, leading edge time, spacecraft used in the analysis, averaged magnetic field magnitude, averaged proton number density, averaged proton temperature, averaged plasma beta, sheath time span, PMS group.

## A.2 Shock and MC parameters

| **Shock time (UT)** | **LE time (UT)** | **Spacecraft** | **B ratio** | **$N_p$ ratio** | **$M_{ms}$** | **$\theta_{Bn}$ (°)** | **$B_{max}$ (nT)** | **$<V>$ (km/s)** | **$\Delta V$ (km/s)** | **PMS group** |
|---|---|---|---|---|---|---|---|---|---|---|
| 1997-01-10, 00:52 | 1997-01-10, 04:58 | Wind | 2.96 | 2.57 | 1.82 | 50.78 | 15.96 | 462.08 | -140 | 4 |
| 1997-11-06, 22:19 | 1997-11-07, 05:28 | Wind | 3.11 | 2.86 | 3.91 | 62.28 | 17.5 | 452.47 | -70 | 4 |
| 1998-01-06, 13:29 | 1998-01-07, 02:50 | Wind | 1.61 | 2.73 | - | 32.60 | 17.49 | 409.29 | -85 | 2 |
| 1998-05-01, 21:21 | 1998-05-02, 09:12 | Wind | 2.14 | 2.16 | 2.73 | 29.28 | 14.74 | 643.15 | -215 | 4 |
| 1998-08-19, 18:40 | 1998-08-20, 09:00 | Wind | 2.20 | 2.26 | 2.37 | 50.54 | 14.47 | 333 | -63 | 4 |
| 1998-09-24, 23:13 | 1998-09-25, 06:17 | ACE | 2.75 | 2.05 | 3.23 | 69.73 | 18.78 | 808.42 | -280 | 4 |
| 1998-10-18, 19:29 | 1998-10-19, 04:22 | Wind | 2.12 | 2.10 | 2.20 | 53.50 | 27.46 | 415.36 | -75 | 5 |
| 1999-02-18, 02:47 | 1999-02-18, 10:28 | Wind | 2.40 | 2.12 | 3.57 | 57.79 | 26 | 647.2 | -280 | 1 |
| 1999-04-16, 10:35 | 1999-04-16, 15:21 | ACE | 1.57 | 1.85 | 1.98 | 30.12 | 6.33 | 453.97 | -80 | - |
| 2000-02-11, 23:34 | 2000-02-12, 12:22 | Wind | 3.32 | 3.43 | 3.19 | 88.53 | 20.19 | 558.28 | -90 | 5 |
| 2000-02-20, 21:04 | 2000-02-21, 05:27 | Wind | 2.27 | 2.52 | 2.47 | 88.81 | 15.26 | 453.4 | -148 | 4 |
| 2000-08-11, 18:11 | 2000-08-12, 04:45 | ACE | 1.98 | 2.01 | 1.83 | 62.11 | 28.47 | 614.36 | -93 | 3 |
| 2000-09-04, 12:45 | 2000-09-04, 21:45 | ACE | 1.62 | 2.21 | - | 11.54 | 7.73 | 420.14 | -80 | 1 |
| 2000-10-03, 01:02 | 2000-10-03, 17:00 | Wind | 1.89 | 1.83 | 1.71 | 47.05 | 16.3 | 416.71 | -57 | 4 |
| 2000-10-12, 22:33 | 2000-10-13, 05:52 | Wind | 2.71 | 2.57 | 2.69 | 73.78 | 19.02 | 472.78 | -105 | 4 |
| 2000-11-06, 09:30 | 2000-11-06, 22:27 | Wind | 2.03 | 2.10 | 2.38 | 46.00 | 17.11 | 575.21 | -185 | 3 |
| 2001-03-19, 11:34 | 2001-03-19, 18:01 | Wind | 2.10 | 1.65 | 2.25 | 83.61 | 17.9 | 462.3 | -175 | 3 |
| 2001-03-27, 17:15 | 2001-03-27, 21:44 | ACE | 2.03 | 2.17 | 1.80 | 84.10 | 14.9 | 625.96 | -85 | 4 |
| 2001-04-11, 13:15 | 2001-04-11, 22:14 | ACE | 1.86 | 2.33 | 1.71 | 52.48 | 31.14 | 714.24 | -140 | 3 |
| 2001-04-21, 15:06 | 2001-04-21, 23:35 | ACE | 2.10 | 2.39 | 2.18 | 41.02 | 11.66 | 381.84 | -60 | 1 |
| 2001-04-28, 04:31 | 2001-04-28, 15:49 | ACE | 2.35 | 2.22 | 5.03 | 85.92 | 16.64 | 634.25 | -160 | 5 |
| 2001-05-27, 14:16 | 2001-05-28, 04:00 | ACE | 2.13 | 2.12 | 2.46 | 51.23 | 8.67 | 546.25 | -145 | 1 |
| 2001-09-29, 09:05 | 2001-09-29, 11:30 | ACE | 2.49 | 2.27 | 1.58 | 17.86 | 11.06 | 682.15 | -265 | 4 |
| 2001-10-31, 12:53 | 2001-10-31, 19:50 | ACE | 1.95 | 2.54 | 2.05 | 18.04 | 12.44 | 375.18 | -95 | 2 |
| 2002-02-28, 04:03 | 2002-02-28, 16:41 | ACE | 1.85 | - | - | 30.87 | 9.55 | 396.59 | -60 | 3 |
| 2002-03-23, 11:24 | 2002-03-24, 11:39 | Wind | 2.58 | 2.32 | 2.70 | 65.71 | 14.01 | 439.99 | -80 | 1 |
| 2002-05-18, 19:46 | 2002-05-19, 03:20 | Wind | 2.95 | 2.47 | 4.09 | 21.72 | 21.34 | 473.65 | -95 | 3 |

| | | | | | | | | | | |
|---|---|---|---|---|---|---|---|---|---|---|
| 2002-08-01, 05:19 | 2002-08-01, 12:50 | Wind | 1.55 | 1.40 | 3.42 | 5.68 | 15.27 | 464.72 | -33 | 1 |
| 2002-09-30, 07:54 | 2002-09-30, 21:26 | Wind | 1.63 | 1.99 | 1.24 | 64.54 | 25.72 | 360.16 | +80 | 4 |
| 2002-11-16, 23:04 | 2002-11-17, 06:45 | ACE | 1.54 | 1.47 | 1.96 | 12.72 | 8.76 | 471.34 | -100 | 1 |
| 2003-03-20, 04:20 | 2003-03-20, 08:30 | ACE | 1.55 | 1.62 | 1.42 | 58.69 | 10.66 | 750.49 | -205 | 1 |
| 2003-08-17, 13:41 | 2003-08-18, 06:00 | ACE | 2.43 | 1.36 | 5.09 | 61.85 | 19.04 | 490.4 | -75 | 2 |
| 2003-11-20, 07:27 | 2003-11-20, 10:48 | ACE | 2.58 | 3.06 | 3.12 | 25.63 | 47.3 | 647.08 | -200 | 3 |
| 2004-07-22, 09:45 | 2004-07-22, 13:01 | Wind | 2.37 | 2.42 | 3.03 | 16.88 | 18.36 | 491.55 | +250 | 1 |
| 2004-07-24, 05:38 | 2004-07-24, 12:05 | ACE | 2.01 | - | - | 30.87 | 21.22 | 582.69 | -180 | 2 |
| 2004-07-26, 22:28 | 2004-07-27, 01:40 | ACE | 4.66 | 2.74 | - | 58.57 | 23.13 | 991.71 | -225 | 1 |
| 2004-08-29, 09:08 | 2004-08-29, 18:31 | Wind | 1.29 | 2.04 | - | 53.78 | 10.36 | 410.03 | -75 | 2 |
| 2005-05-15, 02:11 | 2005-05-15, 05:32 | Wind | 5.50 | 6.21 | 5.43 | 61.34 | 56.71 | 902.87 | -520 | - |
| 2005-06-14, 17:56 | 2005-06-15, 05:15 | Wind | 3.56 | 2.21 | 3.95 | 71.16 | 10.59 | 509.82 | -113 | 4 |
| 2005-07-10, 02:42 | 2005-07-10, 10:10 | Wind | 1.79 | 1.88 | 1.58 | 78.82 | 25.32 | 461.36 | -100 | 1 |
| 2005-07-17, 00:53 | 2005-07-17, 15:17 | Wind | 1.69 | 1.83 | 1.55 | 60.02 | 13.49 | 449.03 | -64 | 1 |
| 2005-09-02, 13:50 | 2005-09-02, 18:43 | Wind | 2.02 | 2.22 | 2.09 | 55.69 | 15.1 | 641.28 | -90 | 4 |
| 2006-04-13, 11:12 | 2006-04-13, 15:15 | ACE | 1.73 | 1.92 | - | 14.89 | 16.02 | 526.88 | -80 | 5 |
| 2006-12-14, 13:52 | 2006-12-14, 22:27 | Wind | 3.51 | 2.93 | 6.59 | 25.06 | 18.05 | 860.86 | -225 | 4 |
| 2007-11-19, 17:16 | 2007-11-19, 23:06 | ACE | 1.81 | 1.83 | 1.57 | 36.56 | 13.83 | 450.09 | -40 | 4 |
| 2009-02-03, 19:21 | 2009-02-04, 02:13 | Wind | 1.59 | 2.16 | 1.39 | 73.62 | 11.48 | 373.19 | -60 | 4 |
| 2009-12-12, 04:38 | 2009-12-12, 18:07 | Wind | 1.40 | 1.20 | 1.97 | 58.86 | 7.74 | 288.59 | -42 | 2 |
| 2010-04-05, 07:56 | 2010-04-05, 12:06 | Wind | 2.38 | 2.19 | 2.58 | 53.83 | 19.89 | 787.7 | -230 | 3 |
| 2010-05-28, 01:53 | 2010-05-28, 19:50 | Wind | 1.44 | 2.97 | 1.68 | 28.72 | 13.79 | 369.68 | -32 | 3 |
| 2011-03-29, 15:10 | 2011-03-30, 00:21 | Wind | 1.79 | 1.86 | 1.98 | 75.45 | 14.57 | 369.23 | -20 | 3 |
| 2011-09-17, 02:57 | 2011-09-17, 15:40 | Wind | 2.42 | 2.24 | 2.86 | 86.76 | 13.47 | 458.28 | -18 | 3 |
| 2012-04-23, 02:15 | 2012-04-23, 16:43 | Wind | 2.45 | 2.44 | 2.37 | 66.48 | 15.95 | 384.3 | +20 | 4 |
| 2012-06-16, 19:35 | 2012-06-16, 22:15 | Wind | 1.87 | 1.73 | 1.93 | 47.37 | 41.14 | 512.1 | -86 | 3 |
| 2012-07-14, 17:39 | 2012-07-15, 06:19 | Wind | 2.08 | 2.53 | 3.64 | 31.96 | 27.76 | 613.47 | -190 | 2 |
| 2012-10-08, 04:12 | 2012-10-08, 17:15 | Wind | 1.96 | 2.01 | 1.96 | 73.85 | 16.7 | 393.68 | +40 | 3 |
| 2012-10-11, 22:47 | 2012-10-12, 15:52 | Wind | 1.31 | 1.57 | 1.12 | 15.12 | 7.55 | 509.16 | +6 | - |

| | | | | | | | | | | |
|---|---|---|---|---|---|---|---|---|---|---|
| 2012-10-31, 14:28 | 2012-10-31, 23:34 | Wind | 2.37 | 2.36 | 2.70 | 86.24 | 16 | 364.71 | -60 | 3 |
| 2012-11-23, 20:51 | 2012-11-24, 11:34 | Wind | 2.81 | 2.35 | 3.37 | 76.14 | 16.44 | 404.09 | -12 | 2 |
| 2013-03-17, 05:22 | 2013-03-17, 11:55 | Wind | 2.45 | 2.68 | 1.89 | 37.92 | 10.84 | 686.29 | -210 | 2 |
| 2013-04-13, 22:13 | 2013-04-14, 16:40 | Wind | 2.61 | 2.39 | 3.64 | 37.28 | 12.99 | 456.04 | -72 | 4 |
| 2013-07-12, 16:43 | 2013-07-13, 04:56 | Wind | 1.98 | 1.56 | 2.74 | 73.24 | 12.91 | 465.65 | -84 | 3 |

**Table A.2:** List of the 61 investigated sheath regions with associated shock and MC parameters. The given quantities, from left to right, are: shock time, leading edge time, spacecraft used in the analysis, magnetic field ratio (shock), proton number density ratio (shock), magnetosonic Mach number (shock), shock angle, maximum magnetic field magnitude at the MC leading edge, mean bulk velocity at the MC leading edge, velocity gradient in the MC, PMS group.

# Appendix B

# Minimum Variance Analysis

The minimum variance analysis (MVA) technique was first introduced by Sonnerup and Cahill, 1967 [63] and successively described in a systematic way by Sonnerup and Scheible [64].

The MVA method is applied to magnetic field vector data from single spacecraft and it aims to give an estimation of the normal vector for an idealized one-dimensional ($\partial/\partial x = \partial/\partial y = 0$) current layer, where therefore

$$\nabla \cdot \mathbf{B} = \frac{\partial B_z}{\partial z} = 0\,. \tag{B.1}$$

From Faraday's law ($\nabla \times \mathbf{E} = -\partial \mathbf{B}/\partial t$) it follows that

$$\frac{\partial B_z}{\partial t} = 0\,, \tag{B.2}$$

so that a spacecraft that crosses the structure measures a constant value of $\partial B_z$.

In such system, three vector measurements ($\mathbf{B}^{(1)}$, $\mathbf{B}^{(2)}$ and $\mathbf{B}^{(3)}$) are sufficient for the determination of the normal vector $\hat{\mathbf{n}}$. Since

$$\mathbf{B}^{(1)} \cdot \hat{\mathbf{n}} = \mathbf{B}^{(2)} \cdot \hat{\mathbf{n}} = \mathbf{B}^{(3)} \cdot \hat{\mathbf{n}}\,, \tag{B.3}$$

it follows that

$$\hat{\mathbf{n}} = \pm \frac{(\mathbf{B}^{(1)} - \mathbf{B}^{(2)}) \times (\mathbf{B}^{(2)} - \mathbf{B}^{(3)})}{\mid (\mathbf{B}^{(1)} - \mathbf{B}^{(2)}) \times (\mathbf{B}^{(2)} - \mathbf{B}^{(3)}) \mid}\,. \tag{B.4}$$

In real layers in space, there are deviations from the ideal one-dimensional situation. The MVA technique deals with such non-ideal layers where, however, there are no temporal changes in the normal direction $\hat{\mathbf{n}}$. Through the method, it is possible to identify that direction in space along which the set $\{\mathbf{B}^{(m)} \cdot \hat{\mathbf{n}}\}$, with $m = 1, 2, 3, \ldots, M$, has minimum variance. The normal vector is therefore determined through the minimization of

$$\sigma^2 = \frac{1}{M} \sum_{m=1}^{M} \mid (\mathbf{B}^{(m)} - < \mathbf{B} >) \cdot \hat{\mathbf{n}} \mid^2\,, \tag{B.5}$$

where

$$< \mathbf{B} >= \frac{1}{M} \sum_{m=1}^{M} \mathbf{B}^{(m)} \tag{B.6}$$

is the averaged magnetic field and the normalization constraint $|\hat{\mathbf{n}}|^2 = 1$ is applied.

Such constraint is implemented through a Lagrange multiplier $\lambda$ and by solving the set of equations

$$\begin{cases} \frac{\partial}{\partial n_x}\big(\sigma^2 - \lambda(|\hat{\mathbf{n}}|^2 - 1)\big) = 0 \\ \frac{\partial}{\partial n_y}\big(\sigma^2 - \lambda(|\hat{\mathbf{n}}|^2 - 1)\big) = 0 \\ \frac{\partial}{\partial n_z}\big(\sigma^2 - \lambda(|\hat{\mathbf{n}}|^2 - 1)\big) = 0\,. \end{cases} \tag{B.7}$$

The resulting set can be written in matrix form as

$$\sum_{\nu=1}^{3} M^B_{\mu\nu} n_\nu = \lambda \nu_\mu\,, \tag{B.8}$$

where

$$M^B_{\mu\nu} =< B_\mu B_\nu > - < B_\mu >< B_\nu > \tag{B.9}$$

is the magnetic variance matrix. From Eq. B.8, it follows that three eigenvalues of $M^B_{\mu\nu}$ are allowed: $\lambda_1$, $\lambda_2$ and $\lambda_3$, given in order of decreasing magnitude. Since $M^B_{\mu\nu}$ is symmetric, the eigenvalues are all real and their corresponding eigenvectors $\mathbf{x}_1$, $\mathbf{x}_2$ and $\mathbf{x}_3$ are orthogonal. The eigenvectors represent, respectively, the maximum, intermediate and minimum variance directions of the field. Therefore,

$$M^B_{ii} =< B_i B_i > - < B_i >< B_i >= \lambda_i\,. \tag{B.10}$$

It follows that the minimum eigenvector $\mathbf{x}_3$ represents the vector normal to the current layer, and its associated eigenvalue $\lambda_3$ is the variance of the magnetic field component along the normal $\mathbf{x}_3$.

# Appendix C

# $\theta$-$\phi$ Diagrams of the Studied Sheaths

## C.1 Group 1: no PMS observed

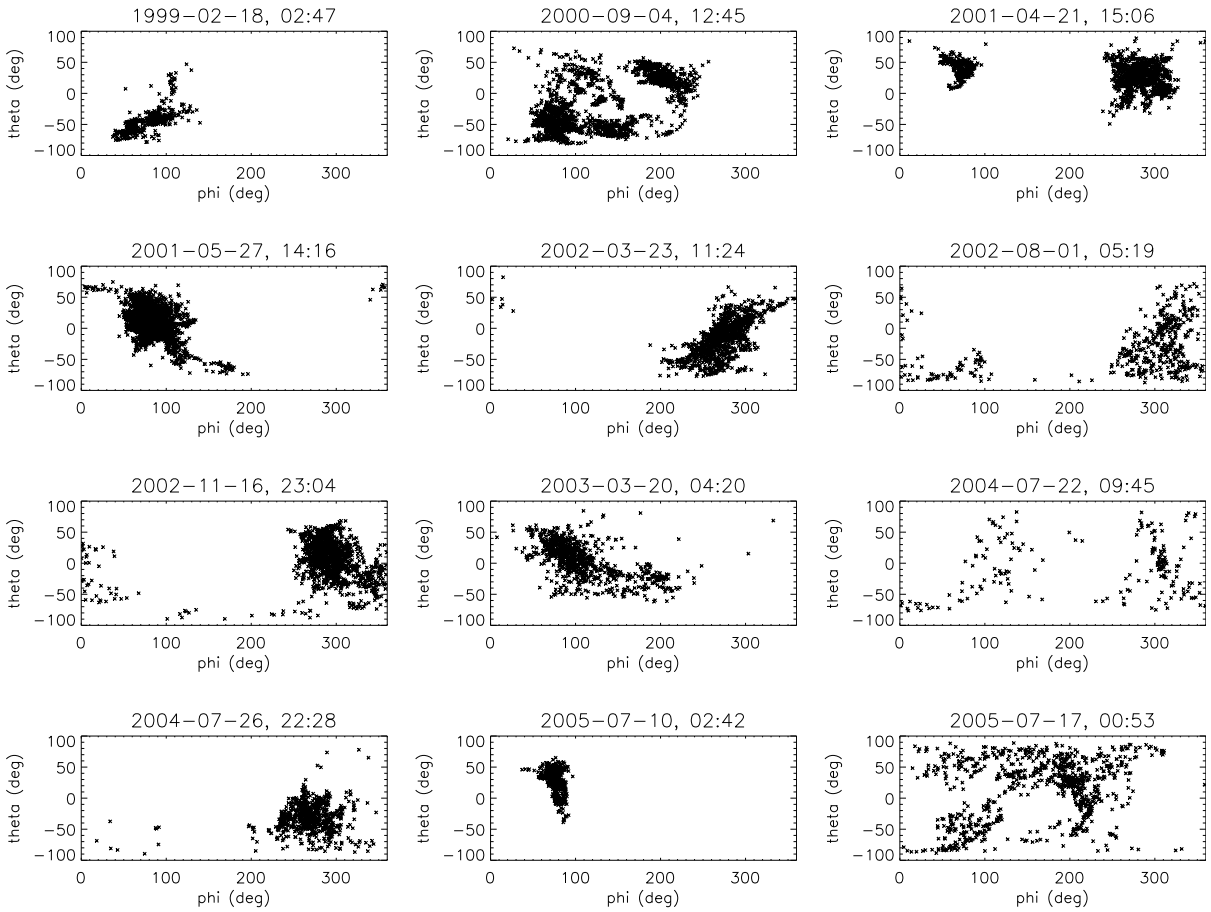


**Figure C.1:** Sheats in Group 1 (no PMS observed). The shock time (UT) is given for each image.

## C.2 Group 2: one PMS close to the shock

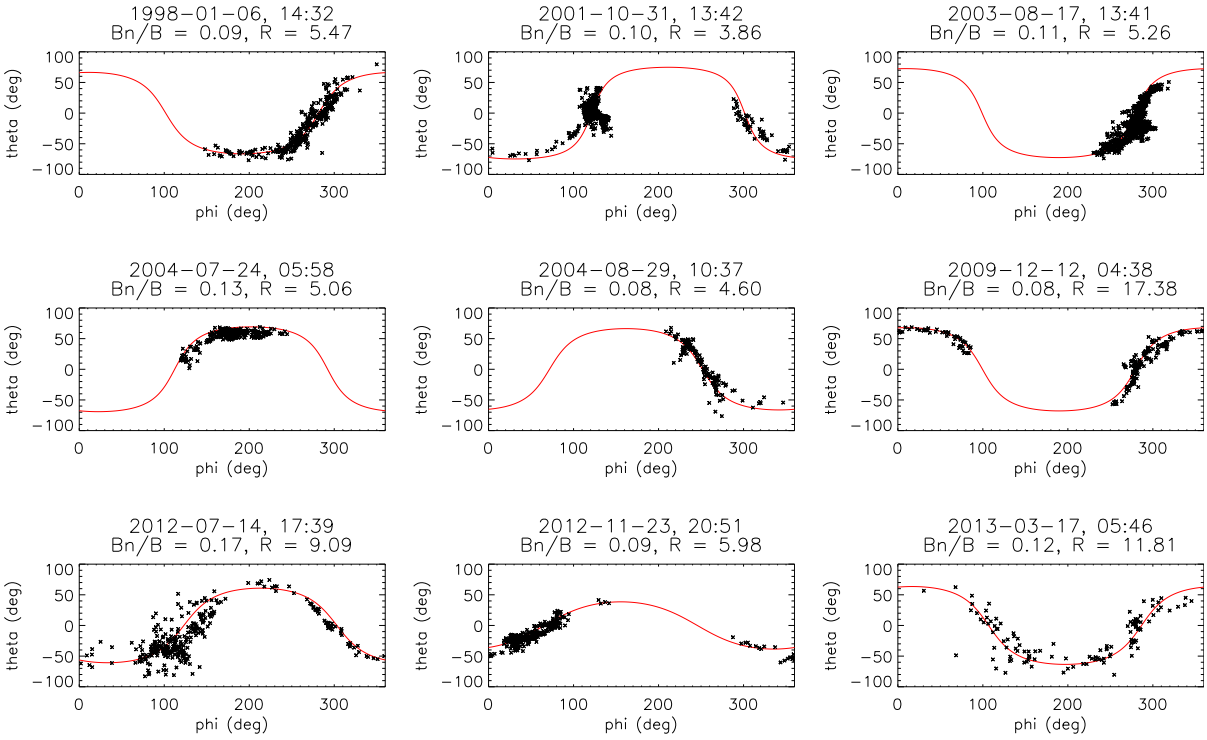


**Figure C.2:** PMSs observed for the sheaths in Group 2 (one PMS close to the shock). The PMS starting time (UT), the value or $B_n/B$ and the intermediate-to-minimum eigenvalue ratio $R$ (Eq. 4.2) are given for each image.

## C.3 Group 3: one PMS close to the leading edge

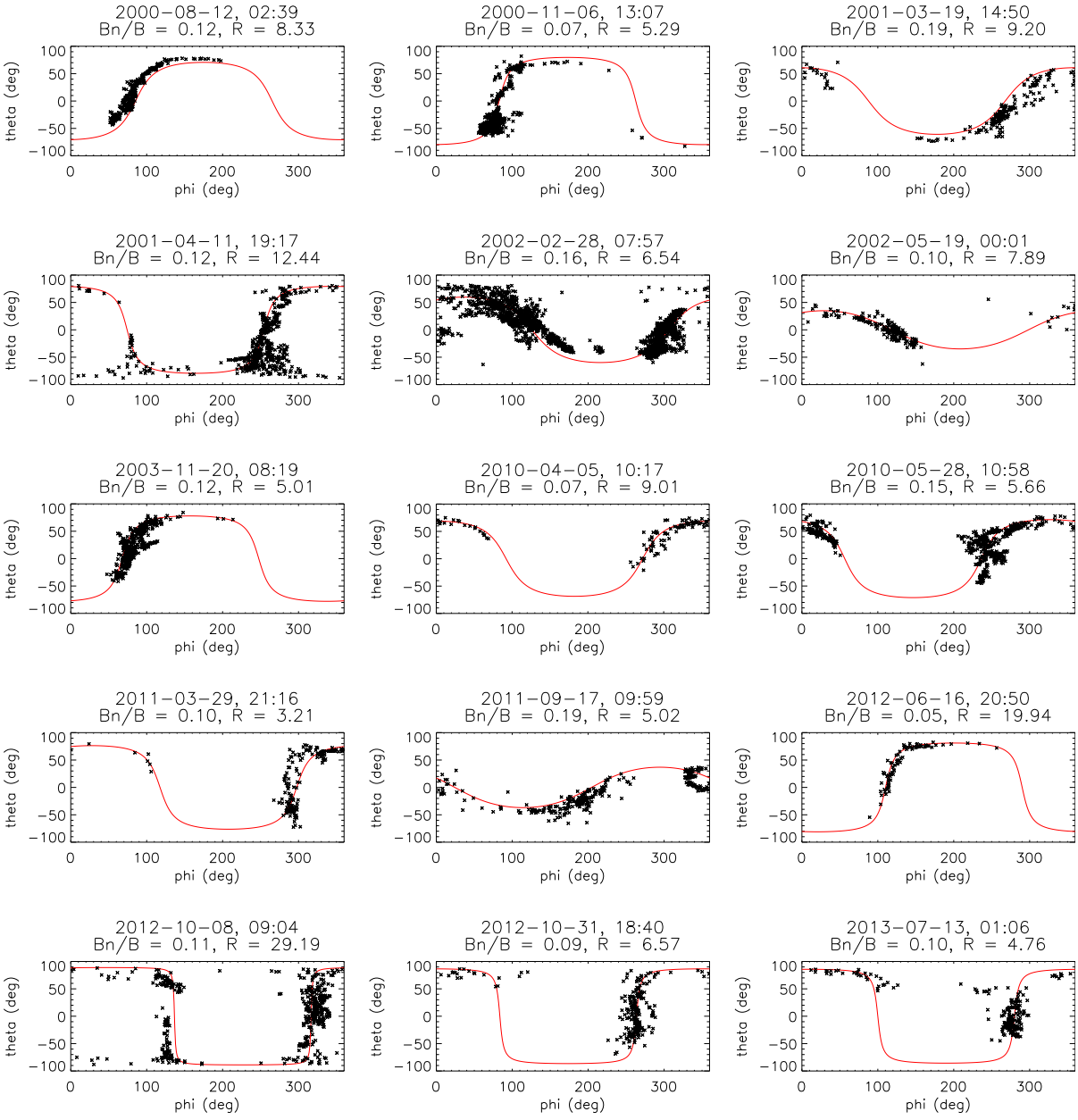


**Figure C.3:** PMSs observed for the sheaths in Group 3 (one PMS close to the MC leading edge). The PMS starting time (UT), the value or $B_n/B$ and the intermediate-to-minimum eigenvalue ratio $R$ (Eq. 4.2) are given for each image.

## C.4 Group 4: PMS over the whole sheath or 2 PMSs

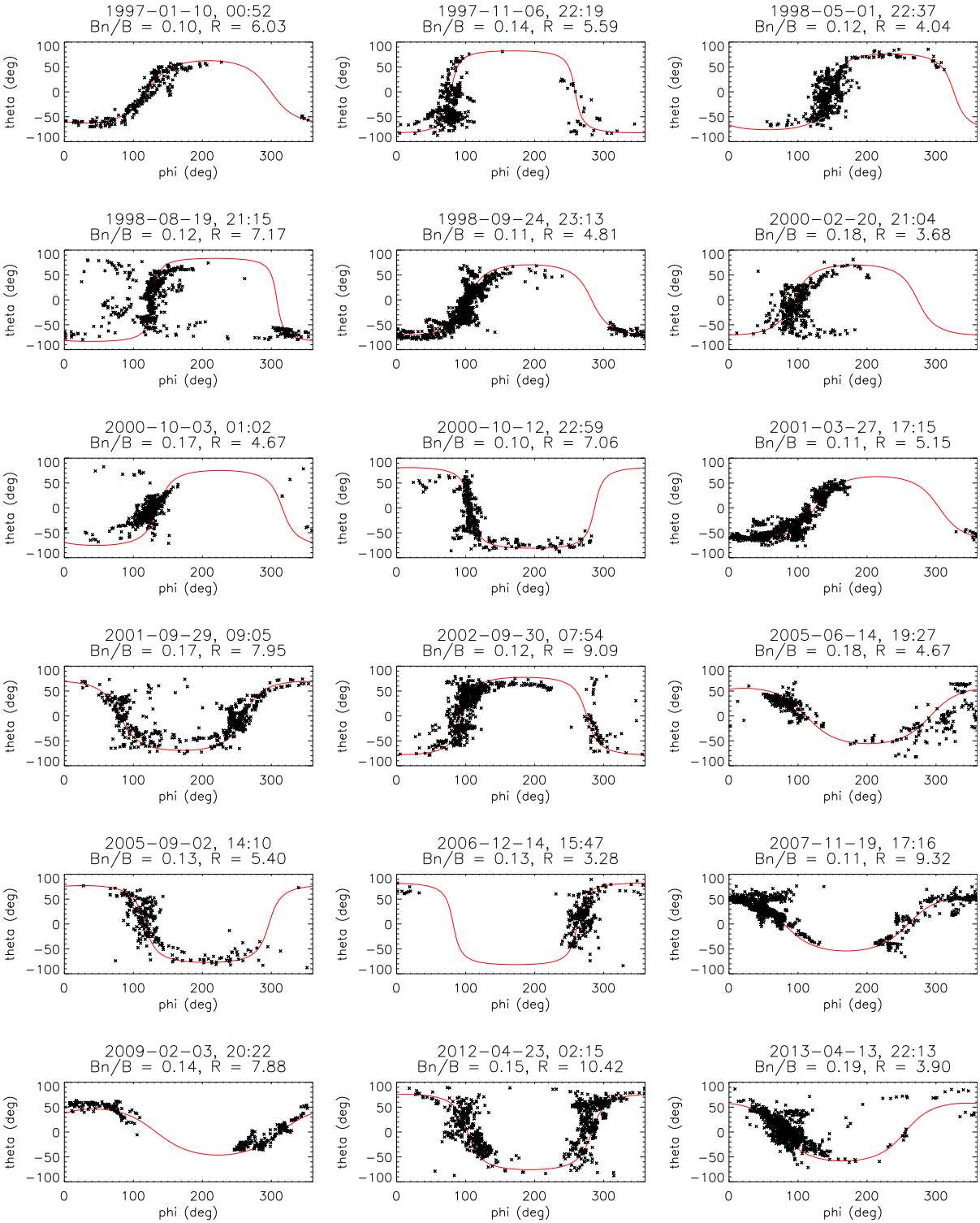

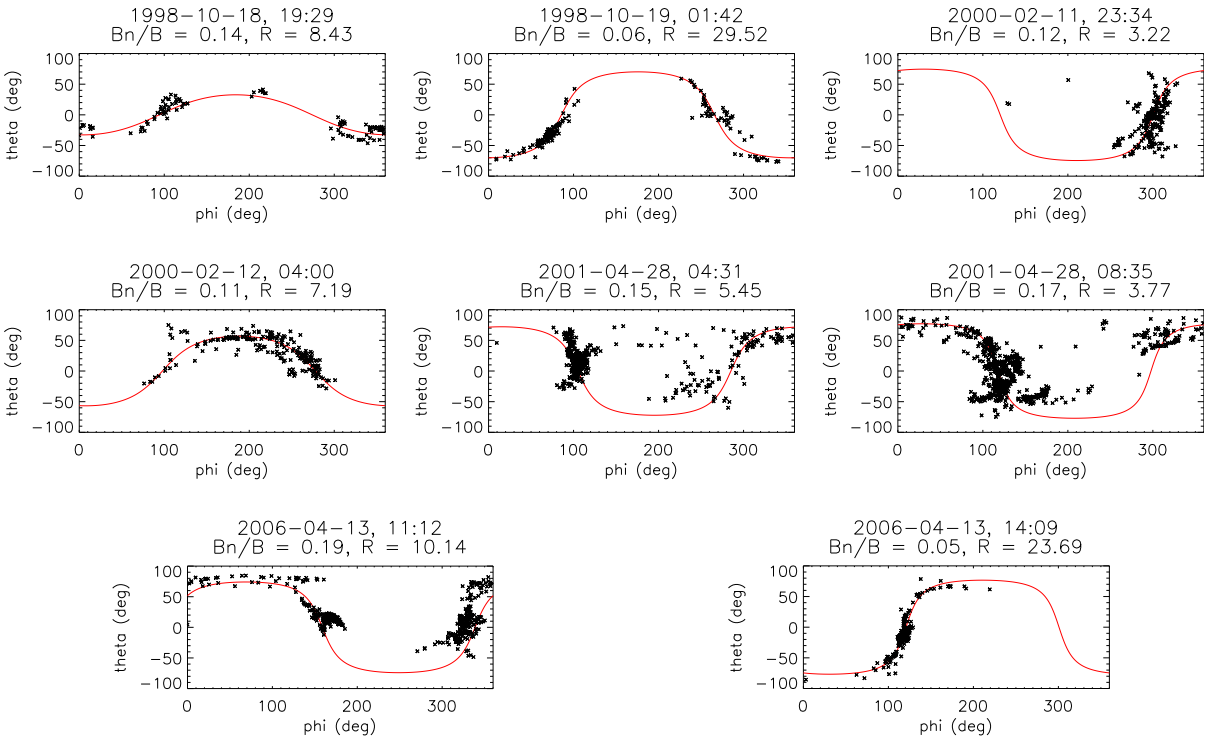


**Figure C.4:** PMSs observed for the sheaths in Group 4 (one PMS covering the whole sheath or 2 PMSs). The PMS starting time (UT), the value or $B_n/B$ and the intermediate-to-minimum eigenvalue ratio $R$ (Eq. 4.2) are given for each image. The first 18 images show the observed PMSs that cover the whole sheath, the last 8 images show the double PMSs (encountered in 4 sheaths).

## C.5 No Group: one PMS in the mid-sheath

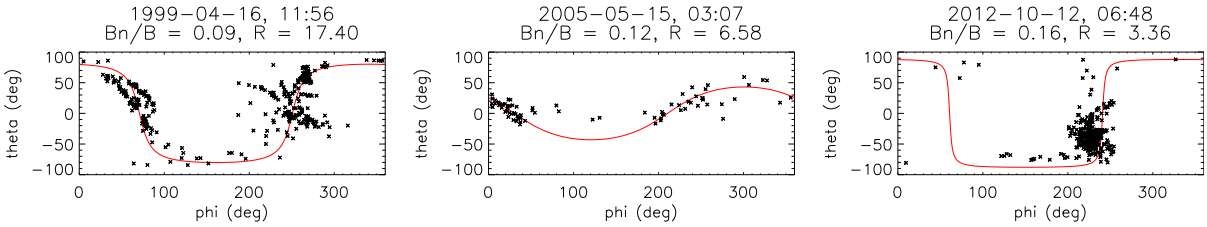


**Figure C.5:** PMSs observed for the sheaths that have been excluded from the statistics (one PMS in the mid-sheath. The PMS starting time (UT), the value or $B_n/B$ and the intermediate-to-minimum eigenvalue ratio $R$ (Eq. 4.2) are given for each image.

# Acronyms

| | |
|---|---|
| ACE | Advanced Composition Explorer (spacecraft) |
| AU | Astronomical Unit |
| CME | Coronal Mass Ejection |
| Dst | Disturbance Storm Time (index) |
| GSE | Geocentric Solar Ecliptic (coordinate system) |
| HCS | Heliospheric Current Sheet |
| ICME | Interplanetary Coronal Mass Ejection |
| IMF | Interplanetary Magnetic Field |
| LASCO | Large Angle and Spectrometric COronagraph |
| LE | Leading Edge |
| MC | Magnetic Cloud |
| MHD | Magnetohydrodynamics |
| MVA | Minimum Variance Analysis |
| PMS | Planar Magnetic Structure |
| SOHO | SOlar and Heliospheric Observatory |
| STD | Standard Deviation |
| STEREO | Solar TErrestrial RElations Observatory |
| UT | Universal Time |

# Bibliography


[1] Alexander, D. An introduction to the pre-cme corona. In *Coronal Mass Ejections*. Springer, 2006, pp. 81–92.

[2] Brueckner, G., Howard, R., Koomen, M., Korendyke, C., Michels, D., Moses, J., Socker, D., Dere, K., Lamy, P., Llebaria, A., et al. The large angle spectroscopic coronagraph (lasco). *Solar Physics 162*, 1-2 (1995), 357–402.

[3] Cane, H., and Lario, D. An introduction to cmes and energetic particles. *Space science reviews 123*, 1-3 (2006), 45–56.

[4] Crooker, N., and Horbury, T. Solar imprint on icmes, their magnetic connectivity, and heliospheric evolution. *Space science reviews 123*, 1-3 (2006), 93–109.

[5] Das, I., Opher, M., Evans, R., Loesch, C., and Gombosi, T. I. Evolution of piled-up compressions in modeled coronal mass ejection sheaths and the resulting sheath structures. *The Astrophysical Journal 729*, 2 (2011), 112.

[6] Evans, R., Opher, M., and Gombosi, T. Learning from the outer heliosphere: Interplanetary coronal mass ejection sheath flows and the ejecta orientation in the lower corona. *The Astrophysical Journal 728*, 1 (2011), 41.

[7] Farrugia, C., Dunlop, M., Geurts, F., Balogh, A., Southwood, D., Bryant, D., Neugebauer, M., and Etemadi, A. An interplanetary planar magnetic structure oriented at a large ( 80 deg) angle to the parker spiral. *Geophysical Research Letters 17*, 8 (1990), 1025–1028.

[8] Fenrich, F., and Luhmann, J. Geomagnetic response to magnetic clouds of different polarity. *Geophysical Research Letters 25*, 15 (1998), 2999–3002.

[9] Forbes, T., Linker, J., Chen, J., Cid, C., Kóta, J., Lee, M., Mann, G., Mikić, Z., Potgieter, M., Schmidt, J., et al. Cme theory and models. In *Coronal Mass Ejections*. Springer, 2006, pp. 251–302.

[10] Forsyth, R., Bothmer, V., Cid, C., Crooker, N., Horbury, T., Kecskemety, K., Klecker, B., Linker, J., Odstrcil, D., Reiner, M., et al. Icmes in the inner heliosphere: Origin, evolution and propagation effects. In *Coronal Mass Ejections*. Springer, 2006, pp. 383–416.

[11] Gazis, P., Balogh, A., Dalla, S., Decker, R., Heber, B., Horbury, T., Kilchenmann, A., Kota, J., Kucharek, H., Kunow, H., et al. Icmes at

high latitudes and in the outer heliosphere. In *Coronal Mass Ejections*. Springer, 2006, pp. 417–451.

[12] Goldstein, H. On the field configuration in magnetic clouds. In *NASA conference publication* (1983), vol. 228.

[13] Gonzalez, W. D., and Tsurutani, B. T. Criteria of interplanetary parameters causing intense magnetic storms ($dst \leqslant -100nt$). *Planetary and Space Science 35*, 9 (1987), 1101–1109.

[14] Gosling, J., Hildner, E., MacQueen, R., Munro, R., Poland, A., and Ross, C. Direct observations of a flare related coronal and solar wind disturbance. *Solar Physics 40*, 2 (1975), 439–448.

[15] Gosling, J., and McComas, D. Field line draping about fast coronal mass ejecta: A source of strong out-of-the-ecliptic interplanetary magnetic fields. *Geophysical Research Letters 14*, 4 (1987), 355–358.

[16] Gosling, J. T. Coronal mass ejections and magnetic flux ropes in interplanetary space. *Physics of Magnetic Flux Ropes* (1990), 343–364.

[17] Gosling, J. T. The solar flare myth. *Journal of Geophysical Research: Space Physics (1978–2012) 98* (Nov. 1993), 18937–18950.

[18] Howard, T. *Coronal mass ejections: An introduction*, vol. 376. Springer, 2011.

[19] Hudson, H., Bougeret, J.-L., and Burkepile, J. Coronal mass ejections: Overview of observations. In *Coronal Mass Ejections*. Springer, 2006, pp. 13–30.

[20] Huttunen, E. *Interplanetary shocks, magnetic clouds and magnetospheric storms*. Finnish Meteorological Institute, 2005.

[21] Huttunen, K., and Koskinen, H. Importance of post-shock streams and sheath region as drivers of intense magnetospheric storms and high-latitude activity. *Annales Geophysicae 22*, 5 (2004), 1729–1738.

[22] Huttunen, K. E. J., Koskinen, H. E., and Schwenn, R. Variability of magnetospheric storms driven by different solar wind perturbations. *Journal of Geophysical Research: Space Physics (1978–2012) 107*, A7 (2002), SMP–20.

[23] Intriligator, D. S., Rees, A., and Horbury, T. S. First analyses of planar magnetic structures associated with the halloween 2003 events from the earth to voyager 1 at 93 au. *Journal of Geophysical Research: Space Physics (1978–2012) 113*, A5 (2008).

[24] Isavnin, A., Kilpua, E. K., and Koskinen, H. E. Grad–shafranov reconstruction of magnetic clouds: overview and improvements. *Solar Physics 273*, 1 (2011), 205–219.

[25] Jian, L., Russell, C., Luhmann, J., and Skoug, R. Properties of interplanetary coronal mass ejections at one au during 1995–2004. *Solar Physics 239*, 1-2 (2006), 393–436.

[26] Jones, G., and Balogh, A. Context and heliographic dependence of heliospheric planar magnetic structures. *Journal of Geophysical Research: Space Physics (1978–2012) 105*, A6 (2000), 12713–12724.

[27] Jones, G., Balogh, A., and Horbury, T. Observations of heliospheric planar and offset-planar magnetic structures. *Geophysical research letters 26*, 1 (1999), 13–16.

[28] Jones, G., Rees, A., Balogh, A., and Forsyth, R. The draping of heliospheric magnetic fields upstream of coronal mass ejecta. *Geophysical research letters 29*, 11 (2002), 15–1.

[29] Jones, G. H., and Balogh, A. Planar structuring of magnetic fields at solar minimum and maximum. *Space Science Reviews 97*, 1-4 (2001), 165–168.

[30] Kajdič, P., Blanco-Cano, X., Aguilar-Rodriguez, E., Russell, C., Jian, L., and Luhmann, J. Waves upstream and downstream of interplanetary shocks driven by coronal mass ejections. *Journal of Geophysical Research: Space Physics (1978–2012) 117*, A6 (2012).

[31] Kataoka, R., Watari, S., Shimada, N., Shimazu, H., and Marubashi, K. Downstream structures of interplanetary fast shocks associated with coronal mass ejections. *Geophysical research letters 32*, 12 (2005).

[32] Kaymaz, Z., and Siscoe, G. Field-line draping around icmes. *Solar Physics 239*, 1-2 (2006), 437–448.

[33] Kilpua, E., Hietala, H., Koskinen, H., Fontaine, D., and Turc, L. Magnetic field and dynamic pressure ulf fluctuations in coronal-mass-ejection-driven sheath regions. *Annales Geophysicae 31*, 9 (2013), 1559–1567.

[34] Kilpua, E., Isavnin, A., Vourlidas, A., Koskinen, H., and Rodriguez, L. On the relationship between interplanetary coronal mass ejections and magnetic clouds. *Annales Geophysicae 31*, 7 (2013), 1251–1265.

[35] Kivelson, M. G., and Russell, C. T. *Introduction to space physics*. Cambridge university press, 1995.

[36] Koskinen, H. *Physics of Space Storms: From the Solar Surface to the Earth*. Springer, 2011.

[37] Kozarev, K. A., Evans, R. M., Schwadron, N. A., Dayeh, M. A., Opher, M., Korreck, K. E., and van der Holst, B. Global numerical modeling of energetic proton acceleration in a coronal mass ejection traveling through the solar corona. *The Astrophysical Journal 778*, 1 (2013), 43.

[38] Lepping, R., Acũna, M., Burlaga, L., Farrell, W., Slavin, J., Schatten, K., Mariani, F., Ness, N., Neubauer, F., Whang, Y., et al. The wind magnetic field investigation. *Space Science Reviews 71*, 1-4 (1995), 207–229.

[39] Liu, Y., Opher, M., Wang, Y., and Gombosi, T. Downstream structure and evolution of a simulated cme-driven sheath in the solar corona. *Astron. Astrophys 527* (2011), A46.

[40] Liu, Y., Richardson, J., Belcher, J., Kasper, J., and Skoug, R. Plasma depletion and mirror waves ahead of icmes. In *36th COSPAR Scientific Assembly* (2006), vol. 36, p. 2515.

[41] Manchester IV, W., Gombosi, T., De Zeeuw, D., Sokolov, I., Roussev, I., Powell, K., Kóta, J., Tóth, G., and Zurbuchen, T. Coronal mass ejection shock and sheath structures relevant to particle acceleration. *The Astrophysical Journal 622*, 2 (2005), 1225.

[42] Mayaud, P.-N. *Derivation, meaning, and use of geomagnetic indices*, vol. 22. American Geophysical Union, 1980.

[43] McComas, D., Bame, S., Barker, P., Feldman, W., Phillips, J., Riley, P., and Griffee, J. Solar wind electron proton alpha monitor (swepam) for the advanced composition explorer. In *The Advanced Composition Explorer Mission*. Springer, 1998, pp. 563–612.

[44] McComas, D., Gosling, J., Winterhalter, D., and Smith, E. Interplanetary magnetic field draping about fast coronal mass ejecta in the outer heliosphere. *Journal of Geophysical Research: Space Physics (1978–2012) 93*, A4 (1988), 2519–2526.

[45] Mikić, Z., and Lee, M. An introduction to theory and models of cmes, shocks, and solar energetic particles. In *Coronal Mass Ejections*. Springer, 2006, pp. 57–80.

[46] Nakagawa, T. Solar source of the interplanetary planar magnetic structures. *Solar physics 147*, 1 (1993), 169–197.

[47] Nakagawa, T., Nishida, A., and Saito, T. Planar magnetic structures in the solar wind. *Journal of Geophysical Research: Space Physics (1978–2012) 94*, A9 (1989), 11761–11775.

[48] Neugebauer, M., Clay, D., and Gosling, J. The origins of planar magnetic structures in the solar wind. *Journal of Geophysical Research: Space Physics (1978–2012) 98*, A6 (1993), 9383–9389.

[49] Ogilvie, K., Chornay, D., Fritzenreiter, R., Hunsaker, F., Keller, J., Lobell, J., Miller, G., Scudder, J., Sittler Jr, E., Torbert, R., et al. Swe, a comprehensive plasma instrument for the wind spacecraft. *Space Science Reviews 71*, 1-4 (1995), 55–77.

[50] Reames, D. V. Particle acceleration at the sun and in the heliosphere. *Space Science Reviews 90*, 3-4 (1999), 413–491.

[51] Richardson, I., and Cane, H. Identification of interplanetary coronal mass ejections at 1 au using multiple solar wind plasma composition anomalies. *Journal of Geophysical Research: Space Physics (1978–2012) 109*, A9 (2004).

[52] Richardson, J. D. Shocks and sheaths in the heliosphere. *Journal of Atmospheric and Solar-Terrestrial Physics 73*, 11 (2011), 1385–1389.

[53] Richardson, J. D., and Liu, Y. A comparison of magnetosheaths, icme sheaths, and the heliosheath. In *Turbulence and Nonlinear Processes in Astrophysical Plasmas(AIP Conference Proceedings Volume 932)* (2007), vol. 932, pp. 387–392.

[54] Savani, N., Owens, M., Rouillard, A., Forsyth, R., Kusano, K., Shiota, D., and Kataoka, R. Evolution of coronal mass ejection morphology with increasing heliocentric distance. i. geometrical analysis. *The Astrophysical Journal 731*, 2 (2011), 109.

[55] Savani, N., Owens, M., Rouillard, A., Forsyth, R., Kusano, K., Shiota, D., Kataoka, R., Jian, L., and Bothmer, V. Evolution of coronal mass ejection morphology with increasing heliocentric distance. ii. in situ observations. *The Astrophysical Journal 732*, 2 (2011), 117.

[56] Schwartz, S. J. Shock and discontinuity normals, mach numbers, and related parameters. *ISSI Scientific Reports Series 1* (1998), 249–270.

[57] Schwenn, R., Raymond, J., Alexander, D., Ciaravella, A., Gopalswamy, N., Howard, R., Hudson, H., Kaufmann, P., Klassen, A., Maia, D., et al. Coronal observations of cmes. *Space Science Reviews 123*, 1-3 (2006), 127–176.

[58] Sheeley, N., Howard, R., Koomen, M., Michels, D., Schwenn, R., Muehlhaeuser, K., and Rosenbauer, H. Coronal mass ejections and interplanetary shocks. *Journal of Geophysical Research: Space Physics (1978–2012) 90*, A1 (1985), 163–175.

[59] Sheeley, N., Walters, J., Wang, Y.-M., and Howard, R. Continuous tracking of coronal outflows: Two kinds of coronal mass ejections. *Journal of Geophysical Research: Space Physics (1978–2012) 104*, A11 (1999), 24739–24767.

[60] Siscoe, G., MacNeice, P., and Odstrcil, D. East-west asymmetry in coronal mass ejection geoeffectiveness. *Space Weather 5*, 4 (2007).

[61] Siscoe, G., and Odstrcil, D. Ways in which icme sheaths differ from magnetosheaths. *Journal of Geophysical Research: Space Physics (1978–2012) 113*, A9 (2008).

[62] Smith, C. W., L'Heureux, J., Ness, N. F., Acuña, M. H., Burlaga, L. F., and Scheifele, J. The ace magnetic fields experiment. In *The Advanced Composition Explorer Mission*. Springer, 1998, pp. 613–632.

[63] Sonnerup, B., and Cahill, L. Magnetopause structure and attitude from explorer 12 observations. *Journal of Geophysical Research 72*, 1 (1967), 171–183.

[64] Sonnerup, B. U., and Scheible, M. Minimum and maximum variance analysis. *Analysis methods for multi-spacecraft data* (1998), 185–220.

[65] Szabo, A., and Wilson, L. I. Wind 2013 senior review proposal. *Executive Summary* (2013).

[66] Tousey, R. The solar corona. In *Space Research Conference* (1973), vol. 1, pp. 713–730.

[67] Vourlidas, A., Lynch, B. J., Howard, R. A., and Li, Y. How many cmes have flux ropes? deciphering the signatures of shocks, flux ropes, and prominences in coronagraph observations of cmes. *Solar Physics 284*, 1 (2013), 179–201.

[68] Wang, Y., Raeder, J., and Russell, C. Plasma depletion layer: Magnetosheath flow structure and forces. *Annales Geophysicae 22* (Mar. 2004), 1001–1017.

[69] Wang, Y., Raeder, J., Russell, C., Phan, T., and Manapat, M. Plasma depletion layer: Event studies with a global model. *Journal of Geophysical Research: Space Physics (1978–2012) 108*, A1 (2003), SMP–8.

[70] Webb, D. F., Cliver, E. W., Crooker, N. U., Cry, O. C. S., and Thompson, B. J. Relationship of halo coronal mass ejections, magnetic clouds, and magnetic storms. *Journal of Geophysical Research: Space Physics (1978–2012) 105* (Apr. 2000), 7491–7508.

[71] Webb, D. F., and Howard, T. A. Coronal mass ejections: Observations. *Living Rev. Solar Phys. 9* (2012), 3–83.

[72] Wimmer-Schweingruber, R., Crooker, N., Balogh, A., Bothmer, V., Forsyth, R., Gazis, P., Gosling, J., Horbury, T., Kilchenmann, A., Richardson, I., et al. Understanding interplanetary coronal mass ejection signatures. *Space Science Reviews 123*, 1-3 (2006), 177–216.

[73] Yermolaev, Y. I., Nikolaeva, N., Lodkina, I., and Yermolaev, M. Y. Geoeffectiveness and efficiency of cir, sheath, and icme in generation of magnetic storms. *Journal of Geophysical Research: Space Physics (1978–2012) 117*, A9 (2012).

[74] Zhang, J., Dere, K., Howard, R., Kundu, M., and White, S. On the temporal relationship between coronal mass ejections and flares. *The Astrophysical Journal 559*, 1 (2001), 452.

[75] Zurbuchen, T. H., and Richardson, I. G. In-situ solar wind and magnetic field signatures of interplanetary coronal mass ejections. *Space Science Reviews 123*, 1-3 (2006), 31–43.

[76] Zwan, B., and Wolf, R. Depletion of solar wind plasma near a planetary boundary. *Journal of Geophysical Research 81*, 10 (1976), 1636–1648.